NREL/TP-451-4720 • UC Category: 271 • DE92001213

NREL/TP--451-4720

DE92 001213

Research on Stable, High Efficiency Amorphous Silicon Multijunction Modules

Semiannual Technical Progress Report 1 May 1991 to 31 October 1991

A. Catalano, R.R. Arya, M. Bennett,
L. Chen, R. D'Aiello, B. Fieselmann,
Y. Li, J. Newton, R. Podlesny,
S. Wiedeman, L. Yang
Solarex Thin Films Division
Newtown, Pennsylvania

NREL technical monitor: Werner Luft

National Renewable Energy Laboratory
(formerly the Solar Energy Research Institute)
1617 Cole Boulevard
Golden, Colorado 80401-3393
A Division of Midwest Research Institute
Operated for the U.S. Department of Energy
under Contract No. DE-AC02-83CH10093

Prepared under Subcontract No.

February 1992

MASTER

DISTRIBUTION OF THIS DOCUMENT IS UNLIMITED

On September 16, 1991 the Solar Energy Institute was designated a national laboratory, and its name was changed to the National Renewable Energy Laboratory.

NOTICE

This report was prepared as an account of work sponsored by an agency of the United States government. Neither the United States government nor any agency thereof, nor any of their employees, makes any warranty, express or implied, or assumes any legal liability or responsibility for the accuracy, completeness, or usefulness of any information, apparatus, product, or process disclosed, or represents that its use would not infringe privately owned rights. Reference herein to any specific commercial product, process, or service by trade name, trademark, manufacturer, or otherwise does not necessarily constitute or imply its endorsement, recommendation, or favoring by the United States government or any agency thereof. The views and opinions of authors expressed herein do not necessarily state or reflect those of the United States government or any agency thereof.

Printed in the United States of America
Available from:
National Technical Information Service
U.S. Department of Commerce
5285 Port Royal Road
Springfield, VA 22161

Price: Microfiche A01
Printed Copy A06

Codes are used for pricing all publications. The code is determined by the number of pages in the publication. Information pertaining to the pricing codes can be found in the current issue of the following publications which are generally available in most libraries: *Energy Research Abstracts (ERA)*; *Government Reports Announcements* and Index (*GRA* and I); *Scientific and Technical Abstract Reports (STAR)*; and publication NTIS-PR-360 available from NTIS at the above address.

DISCLAIMER

Portions of this document may be illegible electronic image products. Images are produced from the best available original document.

SUMMARY

Goal: The primary goal of the Phase II effort is to demonstrate a multijunction module with a stabilized efficiency (600 hrs., 50°C, AM1.5) of 10.5%.

Approach: Triple-junction devices and modules employing silicon alloys with carbon for the widegap top junction and with germanium for the bottom junction will be developed to meet program goals.

Task I: Semiconductor Materials and Device Research

A small area cell initial conversion efficiency of 12.5% is desirable, given an anticipated degradation of 15% in a triple-junction device and other losses associated with module design (loss of active area, etc.). In order to achieve this goal, we require a higher open-circuit voltage (in the range of 2.5 V) than is now obtained in state-of-the-art a-Si:H/a-Si:H/a-SiGe:H devices. Hence, we have begun an aggressive campaign to develop a-SiC:H alloys with acceptable transport properties and stability.

We have sought to develop improved a-SiC:H alloys by employing the paradigm that feedstock gases which incorporate the requisite Si-C bonds will give rise to such desirable bonding in the solid and, hence, improved transport properties. To this end, we have synthesized tri- and di-silylmethanes (TSM, DSM) and employed the conventional hydrogen diluted methane, developed the necessary film deposition processes, fabricated the first devices using these materials and evaluated their performance and stability. The latter issue, ***stability***, is of principal concern with a-SiC:H since previous experience has shown them to be less stable than a-Si:H. Experiments on films have now shown conclusively that the novel feedstocks, particularly TSM, give rise to 1.9 - 2.0 eV with excellent transport and optical properties.

The encouraging results indicating improved transport properties for the a-SiC:H films have been improved further during the period of this report by examining the effect of substrate temperature on film properties. The usual measure of electro-optic properties, diffusion length, photoconductivity, etc., are found to improve at low substrate temperature in contrast with reports of the opposite effect in the literature. This careful study has been done on material having a ***bandgap*** of 1.96 eV $\pm$ .01. The measured properties of the best quality undoped films were found to depend strongly on thickness, suggesting a strong influence of surface effects.

The first devices fabricated show that the improved transport properties of the films, for the most part, translate into better device performance. a-SiC:H devices prepared from DSM have given even better performance than expected based on film results. Most importantly, devices prepared from TSM and hydrogen diluted methane show very good stability compared to conventional a-SiC:H devices. The stability of the devices appears to be comparable to a-Si:H.

In order to design the highest efficiency, stable devices it would be useful to have a quantitative, predictive model for the degradation process. We have succeeded in transforming the stretched exponential model developed by Redfield and Bube which predicts the effect of light exposure on defect density to devices, and confirmed its quantitative, predictive nature by experiment. The model has been expanded to include the effect of i-layer thickness. High intensity illumination has been used to degrade cells to saturation, confirming that the degradation process does indeed level-off after prolonged illumination. The high intensity degradation process can be used to rapidly assess the stability of devices and anticipate AM1.5 performance. The extension of this model to alloys should enable quantitative prediction of multijunction efficiency.

The performance of a-SiGe:H devices has been improved and stability further quantified confirming earlier reports of better stability for this alloy. Optimization of the grading of the p/i and the i/n interfaces has occurred leading to devices with ~ 9% conversion efficiency for 1.48 eV bandgap cells with i-layers only 1200Å thick! Moreover, the stability of a-SiGe:H devices is clearly superior to conventional a-Si:H devices. Since the degradation process is recombination-driven, comparison of devices on the basis of short-circuit current is appropriate. The short-circuit current determines the maximum recombination rate for a given device. Furthermore, in a two-terminal multijunction cell, the short-circuit currents (hence, recombination rates at V_{oc}) are identical in each junction adding to the value of this comparison. Viewed in such a manner, a-SiGe:H alloy devices are far more stable than a-Si:H and the stability improves with Ge addition. At low current, the superior transport properties and higher open-circuit voltage of a-Si:H yields a higher stabilized efficiency.

Task II: Non-Semiconductor Materials Research

Development of an atmospheric pressure chemical vapor deposition (APCVD) process for ZnO has begun in a newly constructed belt furnace. Diethylzinc, ethanol, and water are used as the reactants while both hydrogen fluoride and hexafluoropropylene (HFP) have been employed as dopants. Process development has proceeded by exploring the range of reactant flows, dopant concentrations and substrate temperature on growth rate, haze (texture), resistivity and transmission. The films grown by APCVD appear to be comprised of spherical nodules

compared to films grown by low pressure CVD which have well-defined crystal faces. Device quality films have been prepared which have a higher optical transmission compared to the present APCVD tin oxide of the same sheet resistance. Devices fabricated on the films confirm the higher optical transmission and have exhibited quantum efficiencies as high as 90% without anti-reflecting coating; indicating a net film absorption of about 5%. Further work, however, is necessary to optimize both the device fabrication process on ZnO and obtain better control of the APCVD process.

Low-iron glass has been evaluated as a substrate material to replace the Corning 7059 glass generally used. Optical absorption measurements indicate, and device preparation confirms, that the low-iron glass is an effective, low-cost substitute.

Task III: Submodule Research

Shunting defects in both cells and modules give rise to an anomalous light-induced degradation. The degradation takes place at a higher rate than in samples exhibiting few shunts and frequently gives rise to an increasing rate of degradation at long times. Although the mechanism is unclear, the origin of the defects appears to be large asperities in the tin oxide film formed by ~ 5 μm chunks of the oxide that have spalled off the APCVD furnace or belt. Because these particles are located at the periphery of the substrate, they can be minimized by laser scribing the module to confine the active area of the module away from the edges. Doing so results in a substantial improvement in not only stability, but also the distribution of initial cell and module efficiency. The relationship between the extent of the leakage current and performance has been quantified. Light soaking studies have shown that the degradation of the module, after 600 hours, can be reduced from in the range of over 30% to 17% - 20% by minimizing the shunt current.

The extent of the leakage current appears to depend on the thickness of the junctions of the device including the doped layers, with the greatest thickness giving rise to the lowest shunt currents.

NREL has completed light-soaking studies of some of the **Solarex** first generation triple-junction modules. After 600 hours of exposure at AM1.5, the modules have exhibited 17% - 22% degradation from initial efficiencies in the range of 8.6% to 9.05%. These modules were fabricated before the importance of shunts was recognized.

There has been some suggestion that the rear contact might be involved in the anomalous degradation of modules since shunting defects reappear after curing in modules with ZnO/Ag rear

contacts unlike modules with Al rear contacts. In fact, triple-junction modules with Al rear contacts exhibit far lower degradation (~10%) than their ZnO/Ag backed counterparts. This may be due to the imbalance in the triple-junction device. Thin device (2000Å middle junction) modules, without this imbalance, exhibit degradation at a rate similar to ZnO/Ag.

TABLE OF CONTENTS

Page

1.0 INTRODUCTION 1

2.0 TASK I: SEMICONDUCTOR MATERIALS AND DEVICES 2
2.1 Stability 2
2.1.1 Kinetics of Light-Induced Degradation 2
2.1.2 Thickness Dependence 10
2.1.3 Dependence of Degradation Rate on Deposition Temperature . . . 12
2.2 High Efficiency Single Junction a-SiGe:H Devices 18
2.3 Ultrathin Multijunction Devices 19
2.4 Films and Devices of a-SiC:H 23
2.4.1 Optimization of a-SiC:H Film Properties 24
2.4.2 Boron Doping Study of CH_4+H_2 Based Alloys 35
2.4.3 Stability and Device Performance 37

3.0 TASK II: NON-SEMICONDUCTOR MATERIALS RESEARCH 44
3.1 Substrate Materials 44
3.2 Transparent Front Contacts 44
3.2.1 Textured Tin Oxide (SnO_2) 44
3.4 Back Contact Structures and Material 60
3.5 Solar Cells on ZnO 60

4.0 TASK III: MODULE RESEARCH 65
4.1 Introduction 65
4.2 Impact of Shunts on Initial Device and Module Performance 66
4.3 Origin of Shunts and Ways to Reduce Their Impact 66
4.4 Influence of Rear Contact Material(s) on Shunt 73
4.5 Effect of Shunts on Stability 73
4.6 Other Stability Results 78
4.6.1 Modules Degraded for 2000 hours at NREL 78
4.6.2 Modules Degraded at the PECo Test Site 81
4.6.3 Modules With Al Rear Contacts 81
4.7 Improvement of the Uniformity and Reproducibility of the Front and Rear Contacts 81
4.8 Temperature Coefficient of Triple-Stack Modules 85
4.9 Summary of Task III Progress 85
4.10 Task III Work in Progress 85

REFERENCES 89

LIST OF FIGURES

Figure		Page
2-1.	Time dependences of cell degradation at various temperatures and 140 suns (a), and at various light intensities and 50°C (b). Curves are fits using the SJT model.	4
2-2.	Degradation time dependences at various temperatures and 140 suns (a), various intensities and 50°C (b), and various intensities and 100°C (c). Curves are fits using the RB model.	6
2-3.	Arrhenius plot of $\Delta K = K - K(T = 50°C)$ from **Table 2-1**. The straight line gives an activation energy ~0.52 eV.	7
2-4.	Saturated defect density as a function of light intensity for various temperatures.	9
2-5.	Degradation time dependences for solar cells with various thicknesses. Light soaking was done at 50°C and 50 suns.	11
2-6.	Degradation time dependences for cells with various thicknesses. Light soaking was done at 100°C and 25 suns.	13
2-7.	Stabilized cell efficiency as a function of i-layer thickness measured at 100°C and 25 suns (open circles), and those calculated for 1 sun and 1/3 sun at 50°C. Solid curve is a polynomial fit to the data.	14
2-8.	The percentage loss in normalized efficiency after light exposure equivalent to 2000 hours at 1 sun, as a function of the temperature at which the triple-junction cell was made.	16
2-9.	The absolute efficiency before and after light-induced degradation as a function of the deposition temperature of the cell.	17
2-10.	The J-V characteristics (AM1.5) of a typical a-SiGe:H cell used in the bottom junction of a triple-junction device.	20
2-11.	Quantum efficiency of the same a-SiGe:H device whose J-V characteristics is shown in **Figure 2-10**.	21
2-12.	The initial and normalized efficiencies after 1000 hrs. light-soaking of a-SiGe:H single junction cells vs. initial J_{sc}. The GeH_4 fraction of cells used for each series is indicated.	22
2-13.	Variations with T_s of bandgap, Urbach energy, defect absorption at 1.2 eV, electron $\mu\tau$, and dark conductivity of $CH_4 + H_2$ based a-SiC:H alloys.	25

LIST OF FIGURES (continued)

Figure		Page
2-14.	Variations with T_s of transport and optical properties for $CH_4 + H_2$ based a-SiC:H alloys with the same optical bandgaps.	27
2-15.	Thickness dependence of transport and optical properties for $CH_4 + H_2$ based a-SiC:H alloys of 1.93 - 1.94 eV bandgaps. The T_s is 220°C. H-dilution ratio is 25:1.	28
2-16.	Bandgap dependence of electron $\mu\tau$ of a-SiC:H alloys made from $CH_4 + H_2$ and CH_4 only (without H-dilution).	30
2-17.	Comparison of hole diffusion length for a-SiC:H alloys made with and without H_2 dilution to the $CH_4 + SiH_4$ gas mixture.	31
2-18.	Urbach energy versus optical bandgap for CH_4 and $CH_4 + H_2$ based a-SiC:H alloys.	32
2-19.	Bandgap dependence of defect absorption at 1.2 eV for a-SiC:H alloys derived from $CH_4 + SiH_4$ mixtures with and without H-dilution.	33
2-20.	Infrared transmission spectra for representative a-SiC:H films based on CH_4 and $CH_4 + H_2$ recipes.	34
2-21.	Variations with optical bandgap of electron photoconductive $\mu\tau$ and dark conductivity for CH_4 (without H-dilution) and $C.Cl_3D$ based a-SiC:H alloys.	36
2-22.	Efficiency dependence on illumination time for p-i-n single junction cells using a-SiC:H i-layer with 1.9 eV bandgap prepared from different feed gas mixtures (see **Table 2.5**). The i-layer thickness is in unit of Å.	39
2-23.	Normalized photocurrent versus time of continuous illumination for a-SiC:H films with 1.90 eV bandgap (except the a-Si:H reference film) derived from different gas mixtures.	43
3-1.	Comparison of transmission spectra for 7059F, sodalime and low-iron glass.	45
3-2.	Surface profile scan of tin oxide film over a region containing a high density of particles. One particle is located between 20 - 25 micrometers.	47
3-3.	Sheet resistance of SnO_2 substrate along with others fabricated on ZnO substrates (see **Figure 3-14**).	49

LIST OF FIGURES (continued)

Figure		Page
3-4.	Picture of the APCVD furnace showing how glass substrates are moved under the injection heads.	51
3-5.	Variation in resistance as twelve 6 inch x 12 inch substrates were coated with zinc oxide films. The line above each substrate number gives the range of resistance values.	52
3-6.	Variation in transmission and haze as twelve 6 inch x 12 inch substrates were covered with zinc oxide.	53
3-7.	Visible spectra of a specular (haze 3%) zinc oxide film scanned in a high index fluid (diiodomethane).	55
3-8.	Visible spectra of a textured (haze 19%) zinc oxide film scanned in a high index fluid (diiodomethane).	56
3-9.	Change in resistance of zinc oxide films as a function of dopant (hexafluoropropylene) flow rate. Films were APCVD films prepared at 525°C. The films are all 0.5 - 0.6 microns in thickness.	57
3-10.	Change in APCVD zinc oxide film thickness and resistance as the exhaust rate from the furnace is increased.	58
3-11.	Affect of the flow of diethylzinc at 550°C and 575°C on the thickness of APCVD zinc oxide films.	59
3-12.	SEM pictures showing the difference between the highly crystalline LPCVD zinc oxide films (a) and the APCVD films made of small spheres (b).	61
3-13.	Illuminated I/V curve for single junction control cell made on SnO_2; an identical device fabricated on ZnO yielded a far lower V_{oc} (see **Figure 3-14**).	63
3-14.	Illuminated I/V curve for single junction cell deposited on APCVD ZnO. The control cell I-V is shown in **Figure 3-13**. The currents determined from quantum efficiency measurements (**Table 3-4**) are more accurate and confirm the higher ZnO optical transmission.	64
4-1.	Effect of leakage current on V_{oc} in a small-area triple-junction cell.	67
4-2.	Effect of leakage current on FF in a small-area triple-junction cell.	68
4-3.	Effect of leakage current on V_{oc} in 936.3 cm^2 triple-junction modules.	69

LIST OF FIGURES (continued)

Figure		Page
4-4.	Variation in V_{oc} for triple-stack modules without re-scribes.	70
4-5.	Variation in V_{oc} for triple-stack modules with re-scribes.	71
4-6.	Stability of cells having various metals for the rear contact.	74
4-7.	Average leakage current per segment for 789 cm^2 modules having either Al or ZnO/Ag rear contacts.	75
4-8.	Effect of "shunt" vs. "no shunt" on the stability of a small-area triple-stack cell.	76
4-9.	Outdoor stability measurements of triple-stack modules without re-scribes.	77
4-10.	Change in cell parameters for a module degraded outdoors (without re-scribes). The legend gives the initial and final values of the cell parameters.	79
4-11.	Indoor degradation of six re-scribed modules.	80
4-12.	Outdoor data for two of the triple-junction modules degraded at the PECo test site in Newtown, Pennsylvania (no re-scribes).	82
4-13.	Degradation of 3" x 3" triple-stack modules which are current-imbalanced as a result of having Al rear contacts.	83
4-14.	Indoor stability data for a 789 cm^2 triple-stack module which is more nearly current-balanced than the mini-modules shown in **Figure 4-13.**	84
4-15.	Uniformity of J_{sc} over the surface of a recently made triple-stack module.	86
4-16.	The variation of the cell parameters with temperature for a triple-stack module.	87

LIST OF TABLES

Table		Page
2-1.	Fitting Parameters Used to Model Solar Cell Degradation Data in **Figure 2-2(a).**	8
2-2.	Photovoltaic Parameters for a-SiGe:H Single Junction Cells.	18
2-3.	Initial Parameters of Ultra-Thin Tandem and Triple-Junction Cells.	23
2-4.	Properties of Boron Doped a-SiC:H Films by Two Deposition Methods.	35
2-5.	Initial Characteristics of Representative a-SiC:H Single Junction Cells.	38
2-6.	Comparison of $\alpha_{1.2}$ and E_0 of a-SiC:H Films with 1.90 eV Bandgap Before and After Accelerated Photo-Degradation.	41
3-1.	Comparison of Module Performance for Low-Iron Glass vs. Pyrex.	
3-2.	Properties of a Variety of ZnO and SnO_2 Films.	
3-3.	Properties of ZnO Films Used to Make a-Si Solar Cells.	60
3-4.	Solar Cell Parameters for Cells on ZnO.	62
4-1.	Tandem i_2 Thickness Experiment Analysis of Leakage Current/Segment at -2V.	72
4-2.	Aperture Area Efficiency (in %) of Solarex Triple-Stack Modules Degraded at NREL.	78

1.0 INTRODUCTION

During the first half of the Phase II program, we have sought to quantify the light-induced degradation of a-Si:H devices as part of our overall goal to obtain a working quantitative model for the process in multijunction alloy devices. Simultaneously, we have developed improved wide (a-SiC:H) and narrow (a-SiGe:H) bandgap alloys and alloy-based devices to achieve our ultimate goal of a triple-junction, ***triple bandgap*** device. All triple-junction devices reported on in this report, however, have bandgaps less than or equal to amorphous silicon. With the improvements reported here, devices with wide bandgap top junctions will be possible for the first time. Textured ZnO for the front contact of the device appears to be an attractive alternate to SnO_2, one which promises a higher ultimate transmission and hence higher module performance. We report the first efforts to develop an atmospheric chemical vapor deposition (APCVD) process for that purpose.

In Task III, we combine the elements of the first two tasks to demonstrate improved module performance. Anomalous degradation of the modules compromises the improved stability observed for triple-junction devices. We have learned that the anomalous degradation of modules can be traced to defects in the underlying tin oxide layer, and we have succeeded in limiting the effect of these defects. As our understanding and control over these defects improves, we can expect improvement in the stabilized performance of modules.

2.0 TASK I: SEMICONDUCTOR MATERIALS AND DEVICES

2.1 Stability

2.1.1 Kinetics of Light-Induced Degradation

During the period covered by this report, our view of the time dependent behavior of cell efficiency vs. time has changed. At the onset, a semilogarithmic variation of efficiency vs. time was appropriate at least up to ~ 1000 hrs. (the equivalent of one year outdoors). At longer times changes both indoors and out are virtually impossible to observe. This has changed with the advent of high intensity, accelerated degradation and a stretched exponential mathematical model for the time dependence. For the first time, we are able to make measurements of sufficient accuracy to gage performance at the 20 or even 50 year mark. Hence, these accelerated measurements do not directly include the effect of annealing which counteracts the degradation process because the exposure times are so short. Nonetheless, the comprehensive modeling of device degradation for both a-Si:H and the alloys, remains an important and attainable goal.

Accelerated degradation tests using high intensity light have provided a powerful means to investigate the long-term kinetics of light-induced degradation in amorphous materials and devices **(1-3)**. Our recent study of a-Si:H solar cells showed convincingly that ultimate stability against light exposure is reached at elevated temperatures and the stabilized cell efficiency depends on both temperature and light intensity **(2)**. We have concluded that stabilization at elevated temperatures is caused by the balance between light-induced defect generation and thermal annealing. Stabilization, however, did not occur under the high intensity illumination within the duration of our experiments at 50°C, even though considerable degradation was observed. Therefore, at the start of the period covered by this report, it remained unanswered as to whether solar cells under AM1.5 illumination would also experience the heavy degradation observed at high intensities or if thermal annealing at 50°C would enable cells to stabilize at a higher efficiency under the normal AM1.5 operating intensity. We have collected a set of degradation data on solar cells to examine the validity of various models for the degradation kinetics. This has led to the derivation of a predictive model for solar cells under the normal operating conditions.

The kinetic model of degradation relates the density of defects to the light exposure time. Although it is generally believed that degradation in solar cells is primarily due to an increase in the i-layer defect density, a relationship between the defect density and at least one of the cell parameters is required in order to compare the cell degradation data with the model. While there

is no reliable theoretical prediction, a large body of experimental data have previously shown that over a wide range of exposure times the cell efficiency degrades linearly with log time (4), while the defect density follows a power law time dependence (5). These time dependences can be combined to give the following empirical relationship,

$$\eta = 1 - A \log (N/N_o) \qquad (1)$$

where η and N/N_o are the normalized cell efficiency and defect density in the i-layer, respectively. This relationship holds up to at least 1000 hrs. (equivalent to one year outdoors). The proportionality constant A depends on the structure of the solar cell, e.g. the i-layer thickness, etc. For a single junction a-Si:H cell with a 5000Å thick i-layer, we determined that A in Eq. 1 is approximately 0.6. Since the defect density in the i-layer may not be uniform under white light illumination, N in Eq. 1 should be regarded as a certain averaged defect density.

Despite debates on the origin of defect generation, two kinetic models, proposed by Stutzmann, et al. (5) (SJT) and Redfield, et al. (6) (RB), respectively, have been relatively successful in explaining most experimental observations on films, including the well-known $t^{1/3}$ (time dependence) and $I^{0.6}$ (intensity) power laws, respectively. In the following, we examine the self-consistency of both models without concern about the physical origins on which the models are based.

The SJT Model

The rate equation for photo-degradation in the SJT model can be simplified as,

$$\frac{dN}{dt} = C \frac{I^{1.8}}{N^2} - D(N - N_o) \qquad (2)$$

where the light intensity exponent 1.8 is required by the experimentally observed scaling law, i.e. $I^{1.8}{}_{t=const}$. In Eq. 2, D is the annealing coefficient which is expected to be thermally activated. The rate equation can be solved numerically using C and D as adjustable parameters. By fitting degradation curves measured at 140 suns and at various temperatures, as shown in **Figure 2-1(a)**, we obtained the D values at 100°C, 150°C and 190°C, respectively. These values expectedly formed a straight line in the Arrhenius plot, yielding an activation energy ~0.71 eV. However, the extrapolated D value at 50°C, which is insignificant at 140 suns, is inconsistent with the data measured at reduced light intensities as shown in **Figure 2-1(b)**. The predicted D produces a much larger annealing effect at AM1.5 than is actually observed. It is thus concluded that the

Figure 2-1. Time dependences of cell degradation at various temperatures and 140 suns (a), and at various light intensities and 50°C (b). Curves are fits using the SJT model.

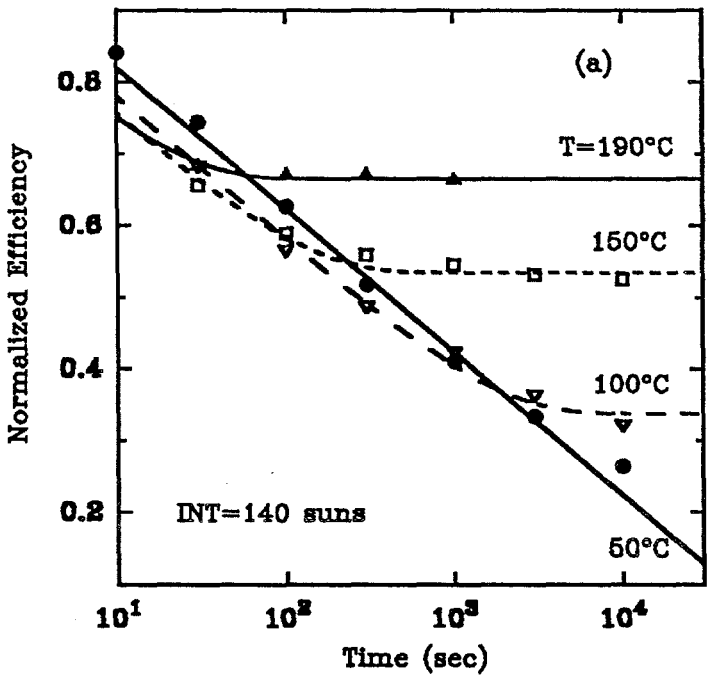

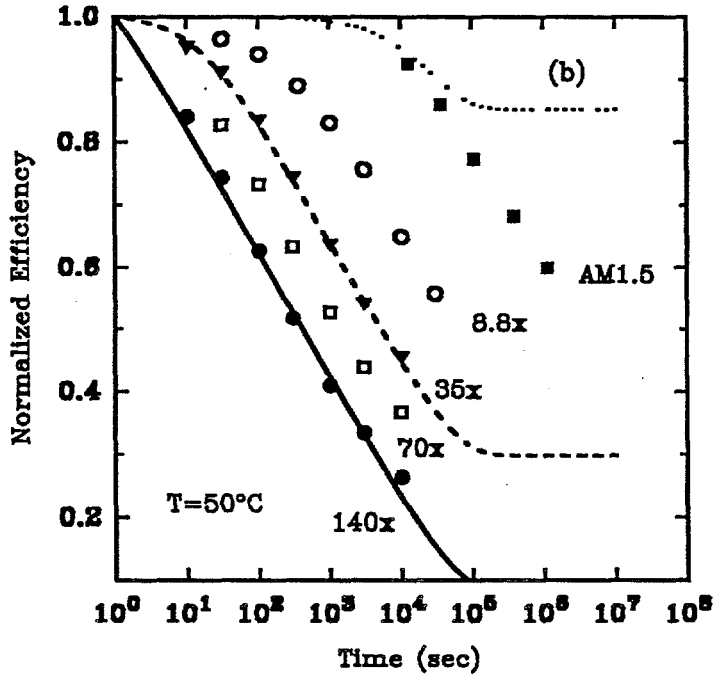

SJT model, defined by Eq. 2, cannot self-consistently explain the cell degradation data. We note, however, that using the complete term for light-induced defect generation, allowing a distribution of annealing energies, and more importantly, setting an upper limit to the defect density may resolve this inconsistency.

The RB Model

In contrast to the SJT model, the RB model introduces a time dependent factor into the rate equation to account for the dispersive nature of the defect generation and annealing. In addition, the model assumes that there is a limit to the number of defects (N_T) and that in principle light-induced annealing and thermal generation terms can exist. However, since the dark equilibrium defect density is much smaller than N_T, thermal generation should be much weaker than thermal annealing and hence can be neglected. The rate equation thus appears as:

$$\frac{dN}{dt} = \left(\frac{t}{P}\right)^{-\alpha} (G - DN) \tag{3}$$

$$G = N_T C_1 R \tag{4}$$

$$D = (C_1 + C_2) R + \nu \tag{5}$$

where P is a characteristic period for the dispersive effect; R is the rate responsible for the light-induced generation and annealing, presumably related to carrier recombination or trapping; C_1 and C_2 are the respective rate coefficients; and ν is the thermally activated frequency for annealing. The solution to Eq. 3 is a stretched exponential,

$$N = N_s - (N_s - N_o) \exp(-Kt^{\beta}) \tag{6}$$

where $N_s = G/D$, $\beta = 1-\alpha$ and $K = \beta^{-1}P^{1-\beta}D$.

Figure 2-2(a) shows the stretched exponential fits to the same temperature series as in **Figure 2-1(a)**. The fitting parameters used are listed in **Table 2-1** in which β is taken to be proportional to T, i.e. $\beta=T/T_o$ (7), and the T_o used here is 718K. We notice that in **Table 2-1**, $N_s xK = G\beta^{-1}P^{1-\beta}$ depends only weakly on temperature. Therefore, the temperature dependence of K is primarily contained in the annealing term. Since ν is likely to be negligible at 50°C, $\Delta K=K-K(T=50°C)$ should be proportional to ν at higher temperatures. Indeed, an excellent straight line was obtained in the Arrhenius plot of ΔK as shown in **Figure 2-3**. The activation energy is ~0.52 eV. The extrapolated value at 50°C, ~0.0093, is truly much smaller than K(T=50°C) we have assumed. While the 0.52 eV activation energy appears to be too small compared with the ~1 eV value observed in the dark annealing experiments, it is actually consistent because for

Figure 2-2. Degradation time dependences at various temperatures and 140 suns (a), various intensities and 50°C (b), and various intensities and 100°C (c). Curves are fits using the RB model.

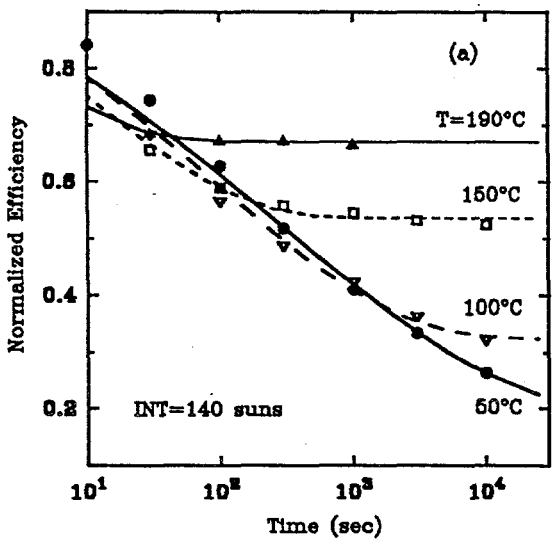

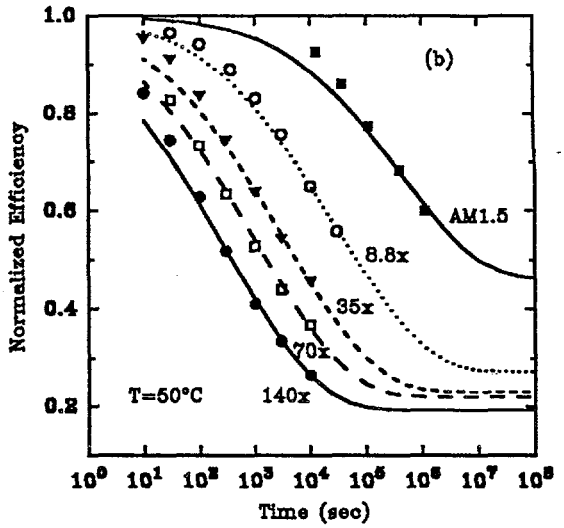

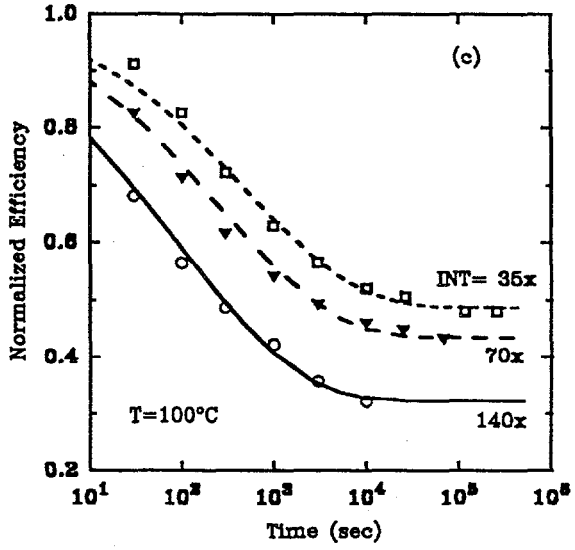

Figure 2-3. Arrhenius plot of $\Delta K = K - K(T = 50°C)$ from **Table 2-1.** The straight line gives an activation energy ~0.52 eV.

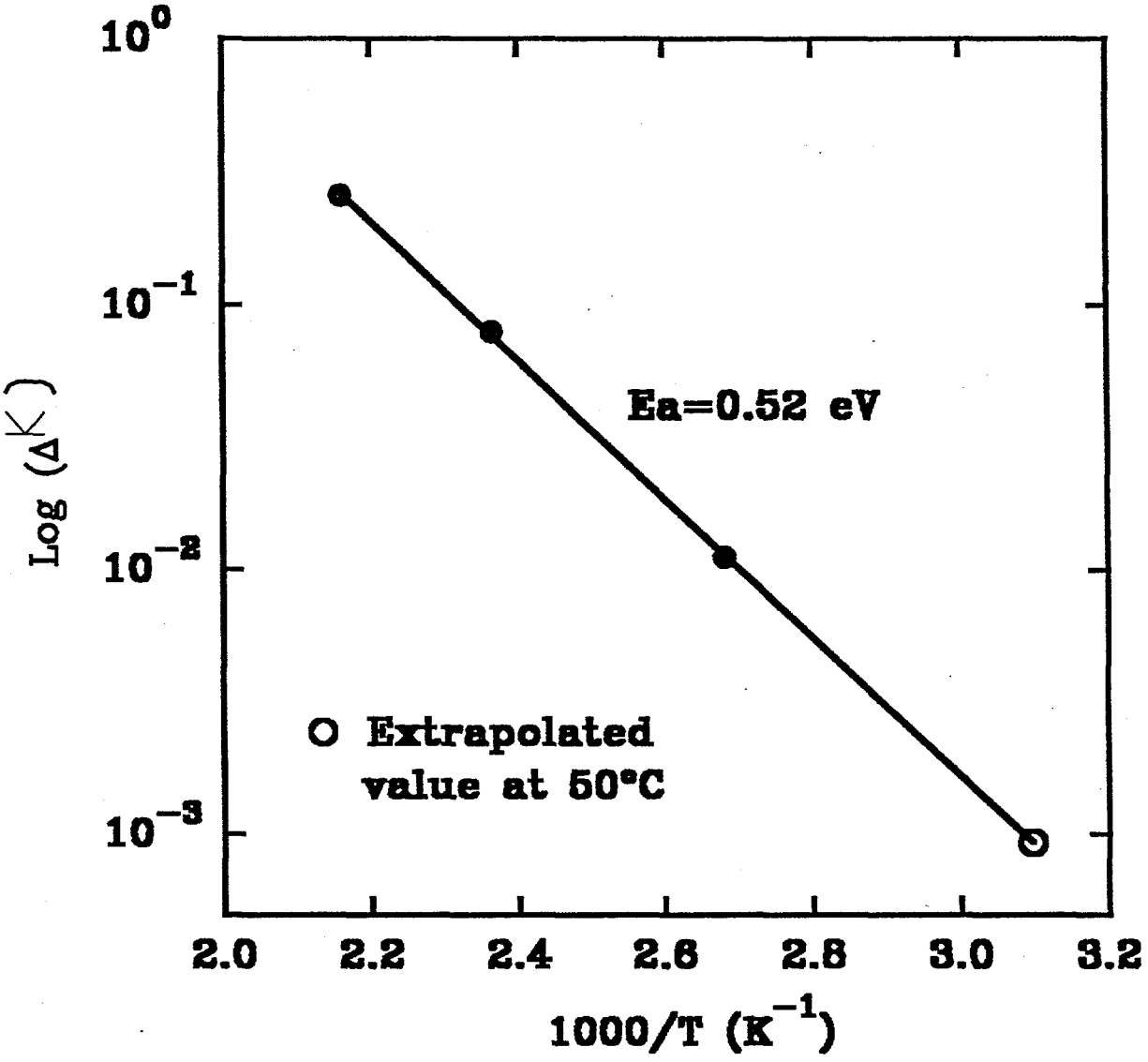

a stretched exponential the activation energy observed experimentally is equal to E_a/β, where E_a is the apparent activation energy contained in ν.

Table 2-1. Fitting Parameters Used to Model Solar Cell Degradation Data in **Figure 2-2(a)**.

T(°C)	β	K	N_s/N_o	KxN_s/N_o
50	0.45	0.022	22.26	0.49
100	0.52	0.033	13.42	0.44
150	0.59	0.102	5.94	0.61
190	0.65	0.278	3.56	0.99

In order to satisfy the experimentally observed scaling law, i.e. $I^{1.8}t$ = const., the rate R must bear an intensity dependence $I^{0.81}$ so that $\exp(-Kt^{\beta}) \sim \exp[(I^{1.8}t)^{\beta}]$. Thus, the complete description for K is:

$$K = 3.90 \times 10^{-4}\, I^{0.81} + 1.17 \times 10^{5} \exp\left(-\frac{0.52}{kT}\right) \tag{7}$$

Where I is in the unit of suns (AM1.5). We now use K values determined by Eq. 7 to fit the other data. **Figures 2-2(b) and 2-2(c)** show the degradation curves measured with various intensities at 50°C and 100°C, respectively. Excellent fits were obtained using N_s as the only adjustable parameter. Since N_s and K are inter-related through G and D, we next examine the consistency of N_s as a function of light intensity and temperature. By expressing N_s in terms of G and K and then substituting them with Eqs. 4 and 7, we obtain,

$$\frac{N_s}{N_o} = A_s \frac{I^{0.81}}{I^{0.81} + \left(3.0 \times 10^{8} \exp\left(-\frac{0.52}{kT}\right) \right)} \tag{8}$$

where A_s is proportional to $C_1\beta^{-1}P^{1-\beta}$ whose weak temperature dependence can be taken into account by using K x N_s/N_o values at various temperatures in **Table 2-1.** We have plotted N_s/N_o as a function of light intensity in **Figure 2-4.** Points were obtained from fitting the data and curves were calculated from Eq. 8. We note that the N_s/N_o values at 100°C, 150°C and 190°C were essentially fixed by the experiments. The excellent agreement between the data points and the calculated curves in **Figure 2-4** indicates that the RB model satisfies all the consistency requirements in explaining the extensive degradation data on solar cells. Furthermore, the RB model predicted that the effect of thermal annealing at 50°C is already

Figure 2-4. Saturated defect density as a function of light intensity for various temperatures.

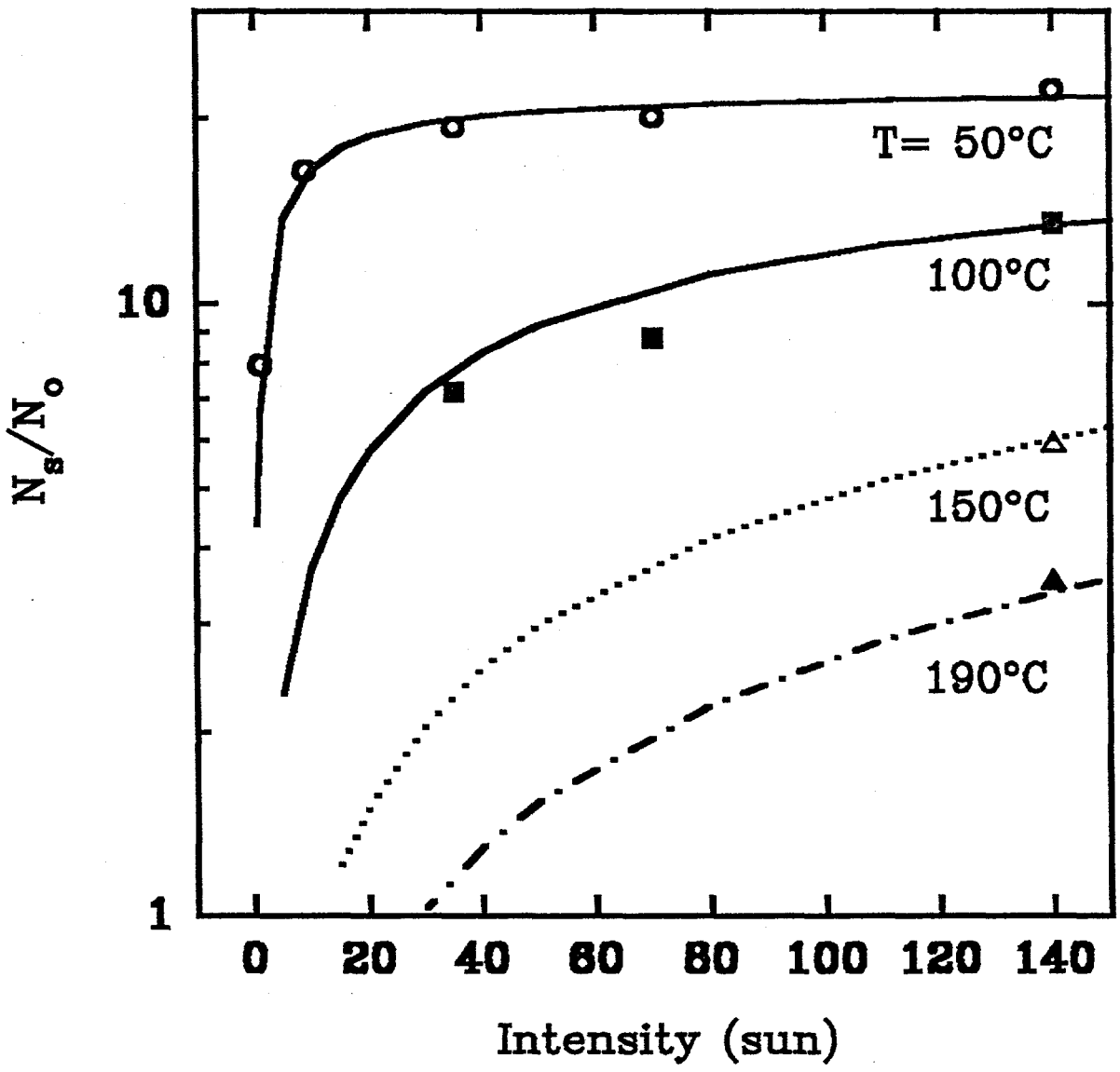

significant under AM1.5 illumination and the cell efficiency would not degrade to the extremely low value as observed at high intensities.

2.1.2 Thickness Dependence

It is well known that the stability of a-Si:H based solar cells can be greatly improved by reducing the thickness of the i-layer (**8,9**). This effect is commonly attributed to the larger electric field present in the thin cell which quickly sweeps carriers across the device making it less sensitive to light-induced defects in the i-layer.

We have explored the thickness dependence of the long-term stability of a-Si:H solar cells using the high intensity accelerated degradation test. While stabilization was only reached at elevated temperatures within the duration of our experiments, the stabilized cell efficiency under device operating conditions were predicted as a function of i-layer thickness using the quantitative RB model described in the previous section.

The a-Si:H solar cells used in this study had a simple heterojunction p-i-n structure in which only the thickness of the i-layer was varied between 2000Å and 8000Å. Intense white light up to ~50 suns (AM1.5), from a focussed xenon arc lamp was used for accelerated light soaking. The solar cells were held at open-circuit during light soaking.

Figure 2-5 shows the normalized efficiency versus exposure time for solar cells with various i-layer thicknesses. The cell temperature was held at ~50°C and the light intensity was ~50 suns. The equivalent soaking time for standard AM1.5 illumination can be estimated using the scaling law $I^{1.8}t=\text{const}$ (**10**). It is apparent that the rate of degradation depends strongly on the thickness of the i-layer as was found previously at low light intensities (**8**). Since cells were light soaked under open-circuit conditions (no electric field across the cell), the defect density in the i-layer is expected to be roughly the same for cells with different i-layer thicknesses. Therefore, the substantial reduction in degradation with decreasing i-layer thickness indicates that thin cells are much less susceptible to defects in the i-layer, i.e. thin devices are able to perform at a higher level relative to their initial values given the same light-induced defect level. At least two factors contribute to this effect: 1) thin cells have longer collection lengths due to increased built-in electric field and 2) photocarriers travel a shorter distance in thin cells in order to be collected.

Accelerated degradation experiments (**10**) and modelling, as shown in the previous section, have shown that the cell performance will eventually stabilize after prolonged light soaking. The stabilization is caused by the balance between defect generation and annealing under the normal

Figure 2-5. Degradation time dependences for solar cells with various thicknesses. Light soaking was done at 50°C and 50 suns.

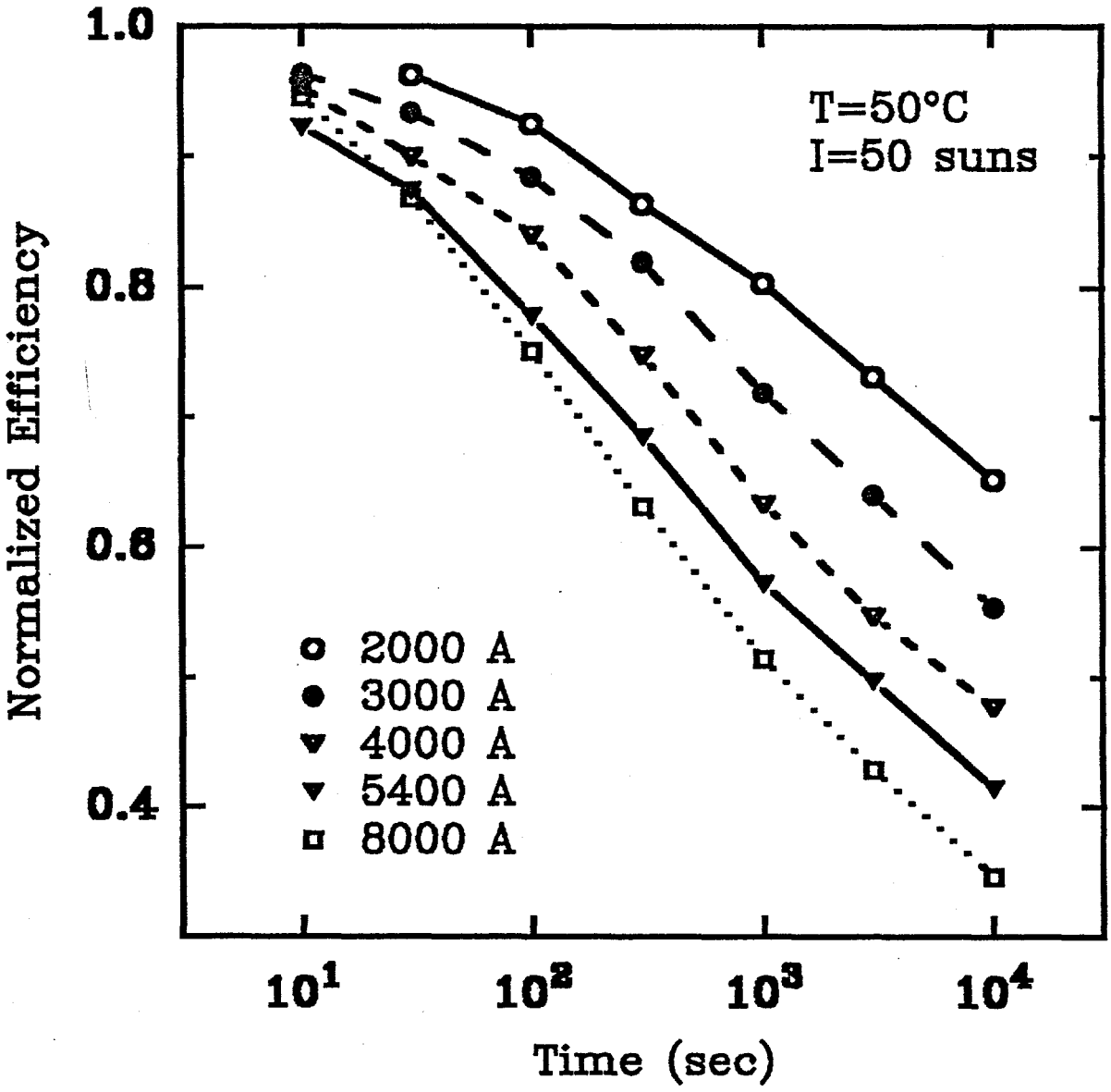

solar cell operating conditions, i.e., AM1.5 and 50°C, or at elevated temperatures. Since the stabilized defect density is roughly independent of the i-layer thickness for a given light soaking condition, cells with different i-layer thickness are expected to exhibit varying stabilized efficiencies for the reasons discussed earlier. To prove this experimentally, we have light soaked cells with different i-layer thicknesses at an intensity of 25 suns and 100°C until they approach stabilization. **Figure 2-6** shows the time dependences of normalized cell efficiency for various i-layer thicknesses. The stabilized efficiency (also normalized) as a function of i-layer thickness under the particular condition is plotted as open circles in **Figure 2-7**. The results confirmed that the thin cells do have better relative efficiencies than the thick ones over the entire lifetime.

The exact thickness dependence of the stabilized efficiency is important for designing the multijunction solar cell with optimized long term efficiency. While stabilization was reached at 100°C and 25 suns, we can estimate the stabilized efficiencies under the normal cell operating conditions using the kinetic model for the solar cell degradation.

By combining Eq. (1), which relates device performance to defect density, with Eq. 8, which gives the time dependence of defect density under illumination, leads to a model which leads to a calculation of the stabilized efficiency (η_S),

$$\eta_S = 1-(1-\eta'_S)\frac{\log(N_S/N_O)}{\log(N'_S/N_O)} \qquad (9)$$

where quantities with the prime are for the condition at which stabilized cell efficiency has been measured. Predictions were made for two conditions. One, at 50°C and AM1.5, is when cells are used in single junction configuration. The other, at 50°C and 1/3 AM1.5 roughly approximates conditions in a triple-junction configuration. Results are shown in dashed curves in **Figure 2-7**. It is interesting to note that the stabilized cell efficiency depends strongly on the light intensity at the operating condition. Therefore, by reducing the effective light intensity in each junction to yield the actual measured short circuit current, the stability of multijunction solar cells can be further improved as shown in **Figure 2-7**.

It should be pointed out that the above analysis is only an approximation. Effects resulting from defects generated at interfaces could be present, complicating the thickness dependence of the light-induced degradation in a-Si:H solar cells.

2.1.3 Dependence of Degradation Rate on Deposition Temperature

It has long been known that deposition temperature affects the properties and composition of a-Si:H. Hydrogen content and bandgap both vary inversely with deposition temperature.

Figure 2-6. Degradation time dependences for cells with various thicknesses. Light soaking was done at 100°C and 25 suns.

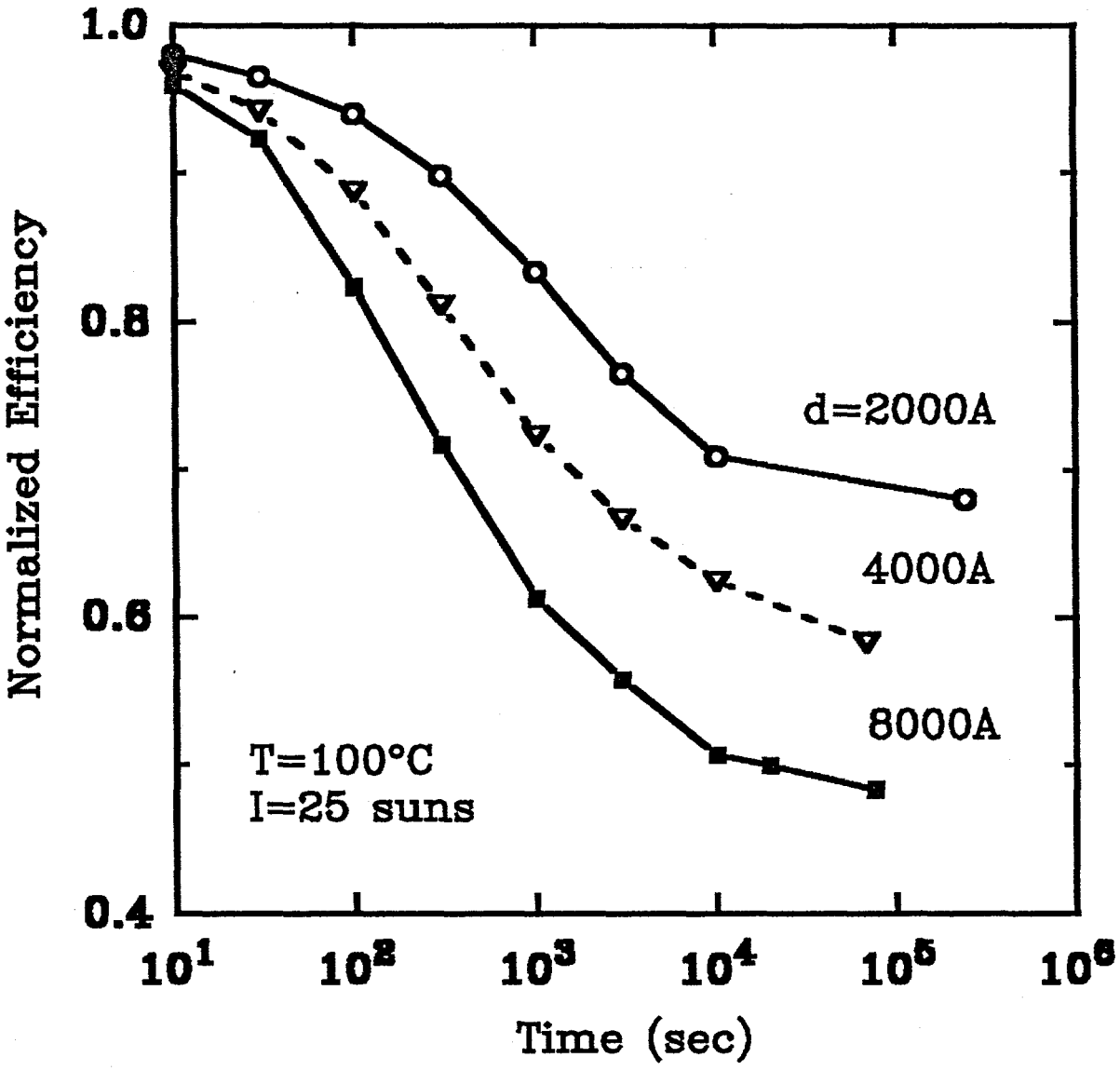

Figure 2-7. Stabilized cell efficiency as a function of i-layer thickness measured at 100°C and 25 suns (open circles), and those calculated for 1 sun and 1/3 sun at 50°C. Solid curve is a polynomial fit to the data.

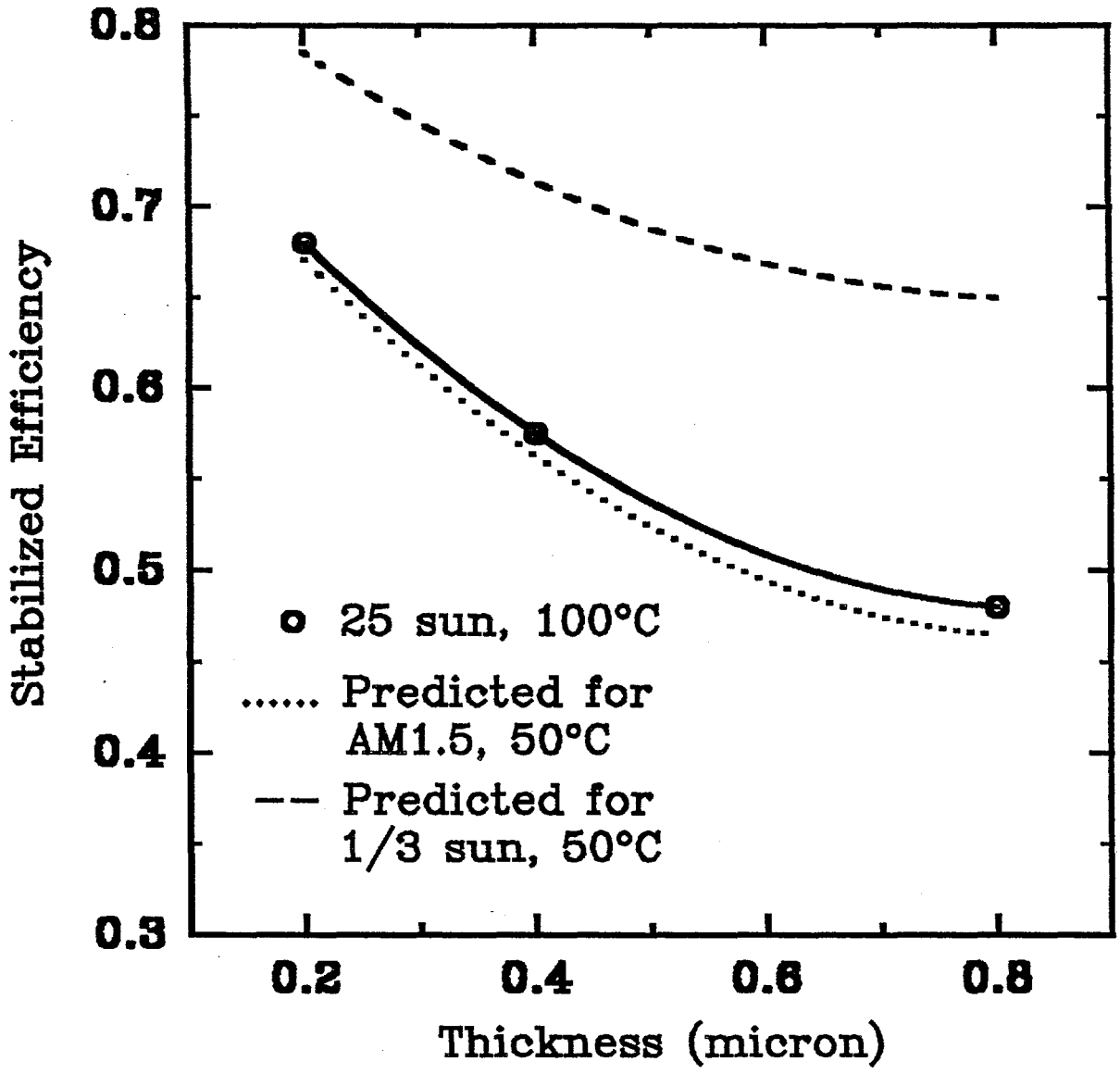

Optoelectronic properties such as photo and dark conductivity are also affected. The influence of deposition temperature on degradation kinetics of a-Si:H has been studied to some degree at Solarex in the past, as well as by others (**11**). Our previous experience with single junction devices has indicated that the degradation rate is increased at deposition temperatures below 250°C. At "normal" substrate temperatures (250°C), degradation clearly depends on i-layer thickness as discussed above. Device design, such as the inclusion of a-SiC:H buffer layers, can also affect stability. This body of experience with single junction cells indicated that, within a range of 250°C to 280°C, device deposition temperature had only a minor influence on device degradation rate due to the Staebler-Wronski effect.

The effect of deposition temperature on stability has been re-evaluated recently for triple-junction cells of a-Si:H/a-Si:H/a-SiGe:H design. Unlike the behavior which would have been expected of single junction cells, the degradation rate evidenced a strong dependence on deposition temperature. The loss in efficiency after an equivalent of 2000 hours exposure at one sun is shown in **Figure 2-8**. Although the sample prepared at the highest temperature is suspect due to an anomalously low starting efficiency, this plot of small area, triple-junction device results indicates that deposition temperature offers a means to substantially reduce the loss in efficiency due to light-induced degradation. The effect of deposition temperature on device stability may be greater simply because of the greater number of serially connected junctions present in the triple cell. The picture is complicated, however, by the potential effect of current balance on device stability for the multijunction cell. Enough work has not yet been done to determine how degradation rate is affected when the light-generated current in one of the junctions of the triple is different than that of the other two junctions. Obviously, the imbalanced junction is biased either toward V_{oc} or toward short circuit by the other junctions when the triple-junction device as a whole is operating at the maximum power point. It can easily be seen that light-induced degradation in an individual junction may affect the overall degradation of the triple cell differently depending on how far it is biased from its own maximum power point when the entire triple cell is operating at the maximum power point.

The highest deposition temperature which could be used will be determined by how much the initial efficiency must be traded off for long-term stability. The loss in initial device efficiency with increasing deposition temperature stems from deterioration of the electronic properties of the doped and intrinsic layers due to loss of hydrogen content, increased defect density, altered doped layer transparency and possibly doping efficiency. This is evident in **Figure 2-9** which shows the absolute efficiency of the small area triple-junction devices of **Figure 2-8** before and after the equivalent of 2000 hours of degradation, one sun. The loss in starting efficiency in this series is due to the effects mentioned above as well as progressive imbalance in the current generation in the individual junctions with increasing deposition temperature, as the device design

Figure 2-8. The percentage loss in normalized efficiency after light exposure equivalent to 2000 hours at 1 sun, as a function of the temperature at which the triple-junction cell was made.

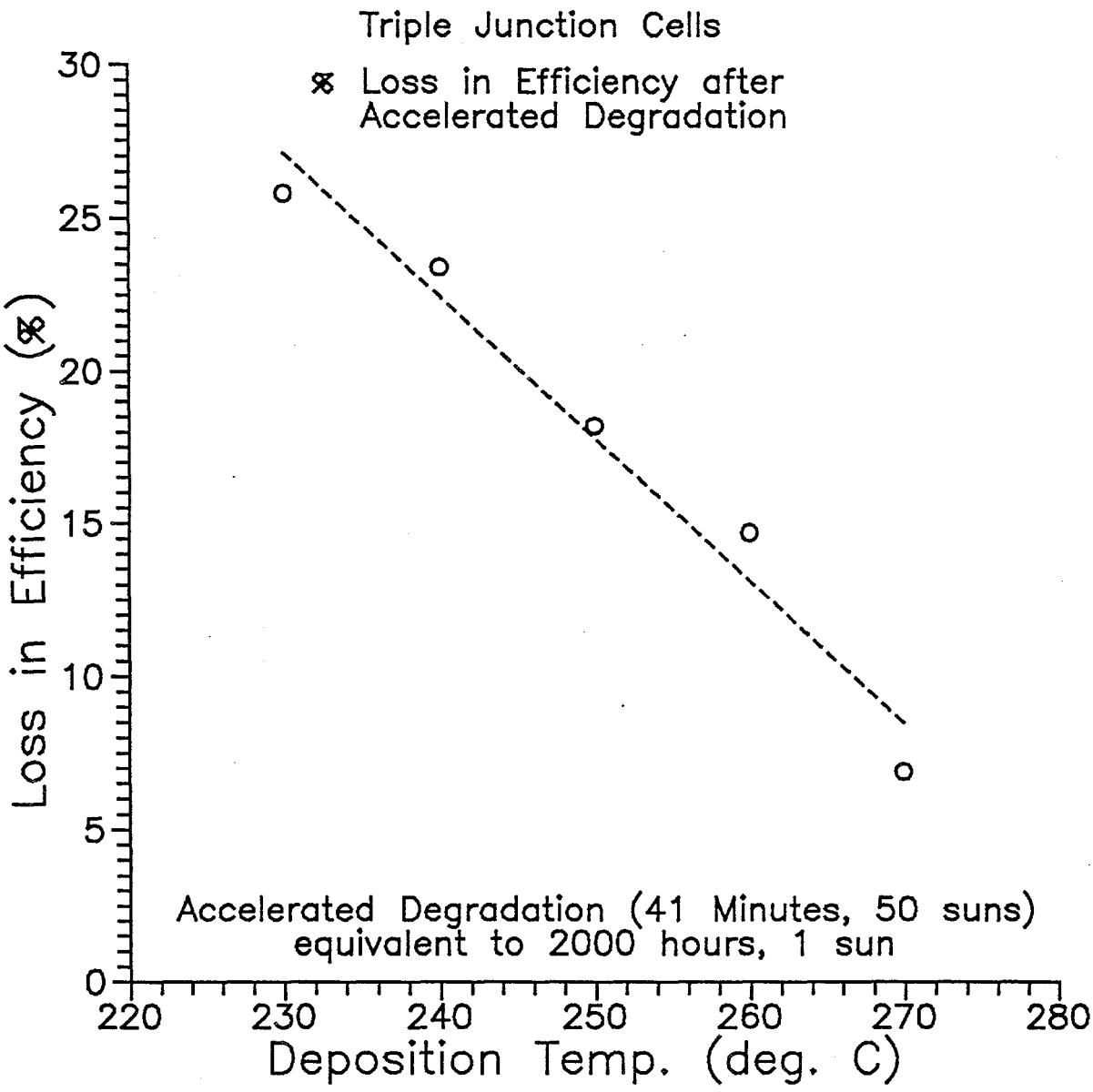

Figure 2-9. The absolute efficiency before and after light-induced degradation as a function of the deposition temperature of the cell.

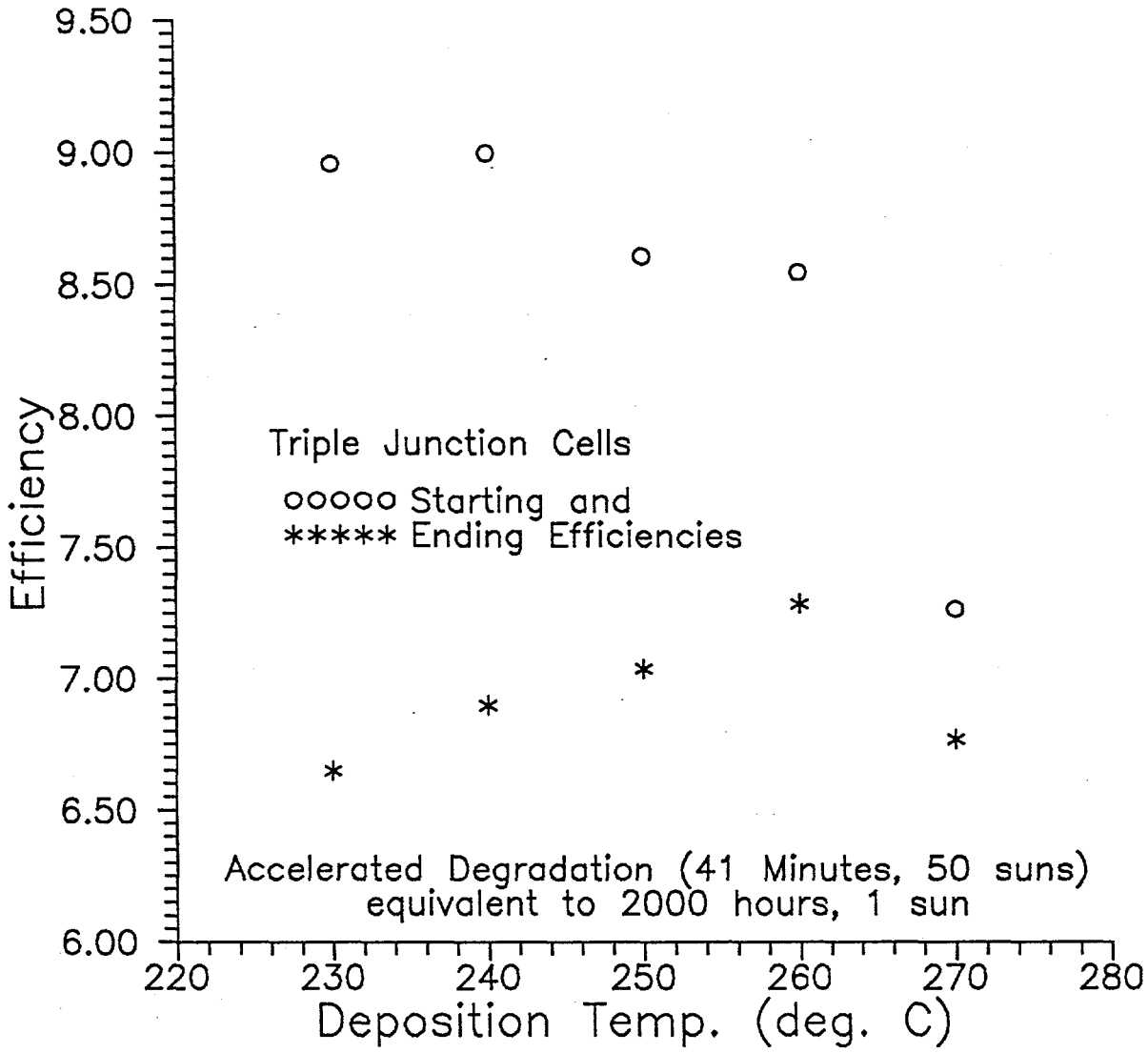

and layer thicknesses was not adjusted to compensate for the decreasing bandgaps caused by higher temperature. Considering the last point to be anomalous due to its low starting efficiency, it is apparent from **Figure 2-9** that the final absolute efficiency after degradation is better for higher deposition temperature in spite of a lower absolute starting efficiency.

Further work is planned to confirm the dependence of triple cell degradation rate on deposition temperature, and to better determine the nature of starting efficiency loss with increasing deposition temperature. It is fairly certain that the initial efficiency can be improved by adjusting the intrinsic layer thicknesses of the triple for better current balance, however, the extent to which the impact of reduced hydrogen content or material quality can be addressed is presently uncertain. If the quality of the doped layers are found to be diminished by deposition at high temperature, it may be possible to deposit various components of the device at differing temperatures using a multi-chamber system. It is possible that the easiest path to high efficiency, stable devices is through efficiency optimization of a stable device, rather than through stability improvements to a high efficiency device.

2.2 High Efficiency Single Junction a-SiGe:H Devices

Our effort to improve the performance of a-SiGe:H cells and assess their stability has continued during this period. After systematic optimization of device structure, particularly the p/i and n/i interface grading, the efficiencies of the single junction cells over a wide range of alloy compositions (GeH_4 concentration from 5% to 25%) have been raised substantially from those devices we had obtained half a year ago. **Table 2-2** lists the initial photovoltaic parameters for the typical single junction a-SiGe:H devices fabricated during this period. It is interesting to note that due to strong optical absorption in a-SiGe:H alloys, high efficiency (~ 9%) devices can be made using very thin i-layers (<< 2000Å). This suggests that higher end-of-life efficiencies than

Table 2-2. Photovoltaic Parameters for a-SiGe:H Single Junction Cells.

GeH_4 fraction	d (μm)	V_{oc} (V)	J_{sc} (mA/cm^2)	FF (%)	η (%)
0.05	0.32	0.81	17.1	66	9.14
0.10	0.19	0.78	17.7	67	9.18
0.15	0.20	0.75	18.1	66	8.84
0.25	0.12	0.70	18.5	67	8.67

is achievable in a-Si:H devices may be possible. Unfortunately, the thin devices are more prone to shunt-related problems which can adversely affect the stability of the device. **Figures 2-10** and **2-11** show the typical I-V characteristics (AM1.5) and the quantum efficiency of the a-SiGe:H devices used in the bottom junction of a triple-junction cell. Notice that excellent fill factor and long wavelength QE response at 800 nm is obtained in these devices.

As part of our effort to establish a comprehensive stability model for multijunction devices, we have begun a systematic study on the stability of a-SiGe:H alloy solar cells. Samples of varying i-layer thicknesses and compositions have been made and degraded under AM1.5 illumination at 50°C. All samples consisted of similar structures for the p/i and n/i buffer layers. Since light-induced degradation of amorphous silicon presumably originates from carrier recombination, the equivalent recombination rate should be used to scale the relative stability of a-SiGe:H alloy materials with different bandgaps. For solar cells being light-soaked under open-circuit conditions, the recombination rate in the i-layer is roughly proportional to the short circuit current (J_{sc}) before light-soaking provided the cell fill factor is high and complete charge collection is approached at short circuit. **Figure 2-12** (a) shows the initial efficiencies of groups of cells each with different composition as a function of initial J_{sc}. The initial efficiency clearly reaches a peak with increasing J_{sc} (or thickness) for each series of cells at a constant Ge concentration. This behavior is expected because the efficiency is limited by light absorption at low thickness and by poor fill factor when thickness is too large. It is also expected that J_{sc}'s corresponding to peak initial efficiencies increase with Ge concentration. **Figure 2-12** (b) shows the normalized efficiencies after 1000 hours of light-soaking at 100 mW/cm^2 as a function of J_{sc}. It is apparent that for a given J_{sc} (or carrier generation rate), the relative stability of a-SiGe:H cells improves substantially with increasing Ge concentration. ***This result is important because it indicates that replacing a-Si:H with a-SiGe:H alloy in the middle junction or increasing Ge concentration in the back junction of a triple-stack solar cell (with similar current balance) will generally improve the device stability (see Section 2.3 for further discussion).*** There has been some evidence that the design of a-SiGe:H solar cells may also influence the device stability. A systematic study of the effect of design on stability will be conducted.

2.3 Ultrathin Multijunction Devices

The stability of the current Si/Si/SiGe triple-junction device is strongly limited by the a-Si:H middle junction which is the thickest among the three junctions. The thickness of the middle junction i-layer, i_2, ranges from 4000Å to 6000Å in order to balance the current. For example, after 600 hours of continuous light soaking at AM1.5 and 50°C, a 4000Å a-Si:H middle junction

Figure 2-10. The J-V characteristics (AM1.5) of a typical a-SiGe:H cell used in the bottom junction of a triple-junction device.

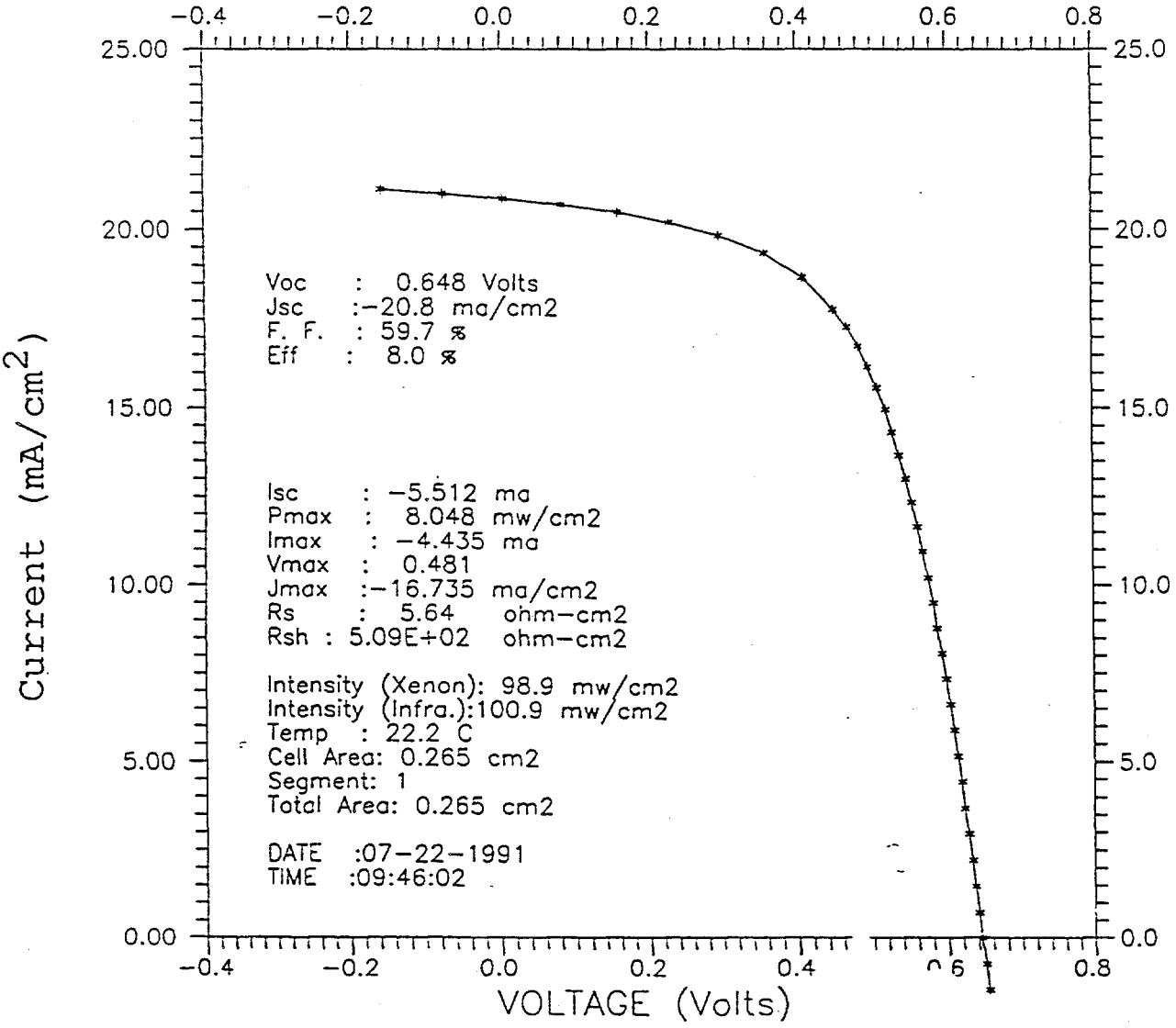

Figure 2-11. Quantum efficiency of the same a-SiGe:H device whose J-V characteristics is shown in **Figure 2-10.**

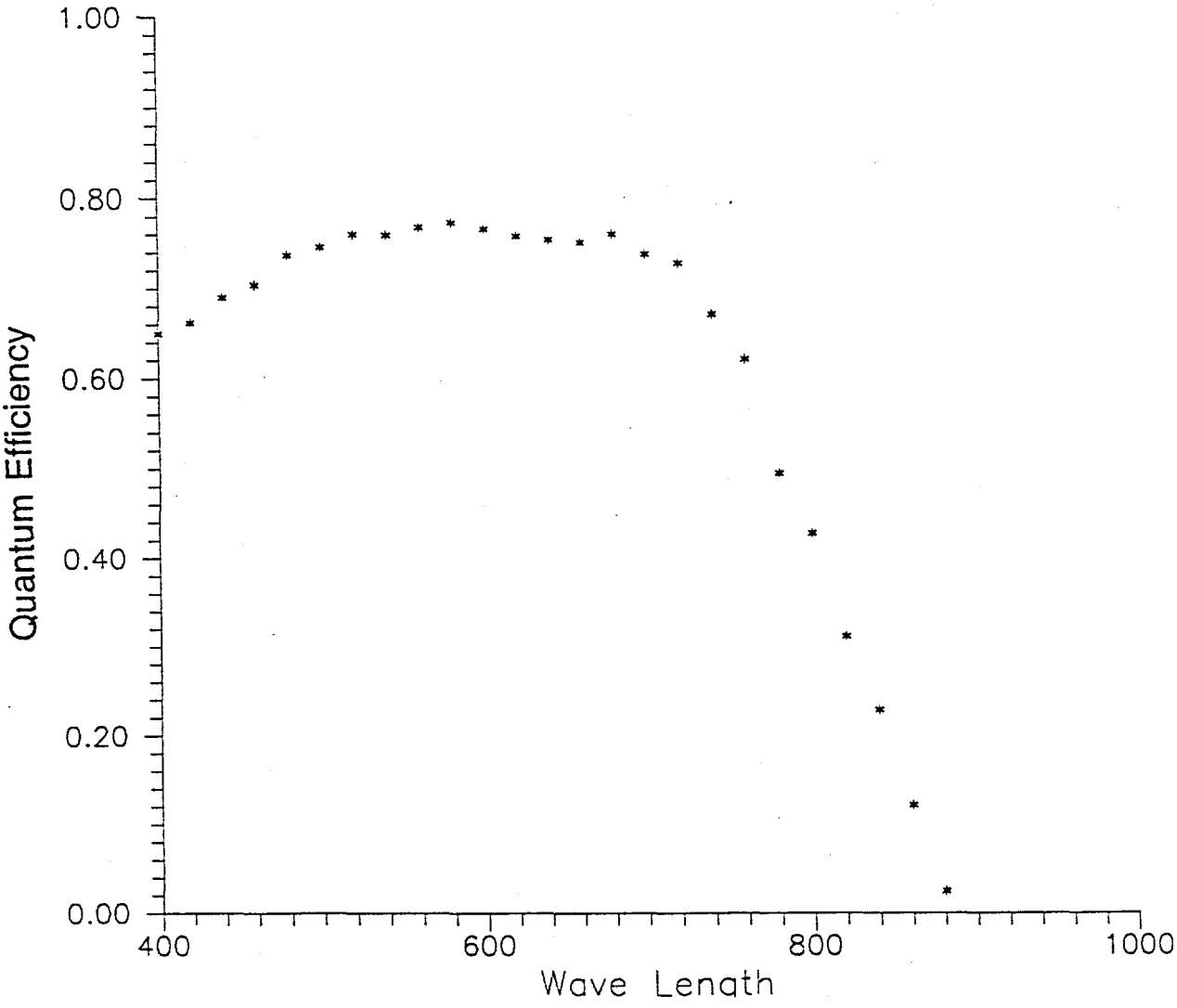

Figure 2-12. The initial and normalized efficiencies after 1000 hrs. light-soaking of a-SiGe:H single junction cells vs. initial J_{sc}. The GeH_4 fraction of cells used for each series is indicated.

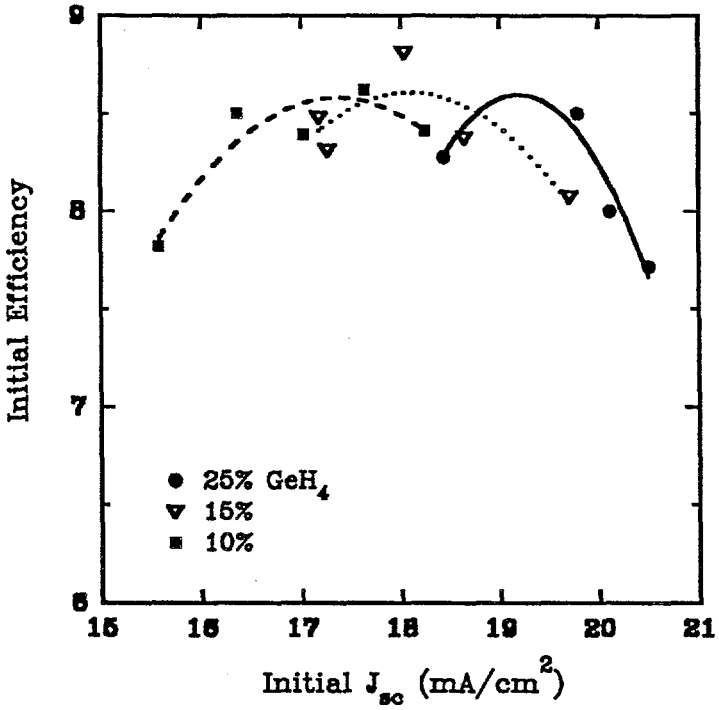

(a)

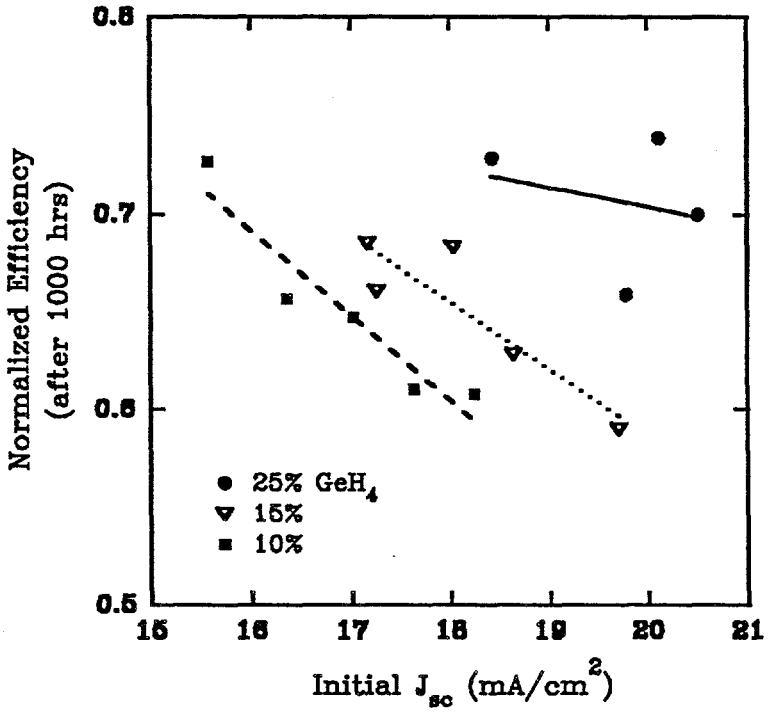

(b)

would degrade about 28% while the 1800Å a-SiGe:H back junction would degrade only about 12%, and the 600Å front junction would suffer essentially no degradation (each component absorbs ~1/3 of the incident light). Therefore, we have explored the possibility of using SiGe alloy in the middle junction in order to substantially reduce the thickness of this junction and improve the device stability. Tandem devices with an a-Si:H front junction and an a-SiGe:H back junction have also been fabricated in which both junctions are quite thin. **Table 2-3** lists the structures and the photovoltaic parameters for various triple and tandem devices. It is quite clear from **Table 2-3** that with increasing GeH_4 fraction in the deposition, a much thinner i_2 layer is needed to balance the current. The open-circuit voltage decreases slightly as Ge is added to the middle junction. However, the fill factor and the overall efficiencies remain fairly good due to improved performance of the SiGe junctions. Preliminary light-soaking tests have indicated that the ultra-thin multijunction devices have indeed superior stability compared to standard 4000Å Si/Si/SiGe devices.

Table 2-3. Initial Parameters of Ultra-Thin Tandem and Triple-Junction Cells With Ge in the Middle and Bottom Cells.

Cell	I1	I2	I3	V_{oc}	J_{sc}	FF	η
	(GeH_4 Fraction, Thickness Å			(V)	(mA/cm^2)	(%)	(%)
MC1260-1	0%, 650	2%, 3500	20%, 1800	2.28	6.1	67	9.3
D11009-1	0%, 600	5%, 3400	25%, 1800	2.24	6.2	69	9.5
D11021-1	0%, 600	10%, 2200	25%, 1800	2.19	6.5	65	9.2
D11104-2	0%, 600	15%, 1900	25%, 1800	2.17	6.7	66	9.7
D10801-4	0%,1200	15%, 1700		1.56	9.3	64	9.3
MC1273-1	0%,1400	20%, 2100		1.5	9.6	64	9.3

2.4 Films and Devices of a-SiC:H

As part of Task I - Semiconductor Materials Research in the NREL contract, we have continued to search for improved deposition conditions for rf glow-discharge a-SiC:H alloys with bandgaps 1.8 - 2.0 eV and to evaluate their device application potential. The objectives are to optimize the photo-electronic properties ***and*** to minimize light-induced instability in solar cells. Progress has been made in both areas as described below.

2.4.1 Optimization of a-SiC:H Film Properties

Our approach to optimizing a-SiC:H consists of two parallel methods. One is to find the optimal glow-discharge deposition conditions for a-SiC:H using the conventional feedstock methane (CH_4) as the carbon source by employing hydrogen dilution (the CH_4+H_2 recipe). The other method is to explore novel carbon feedstocks that have the desired Si-C bonds built-in so as to maximize the Si-C bond density and to reduce the methyl group (CH_2 and CH_3) concentration in the solid film. As stated in the last annual report (**12**), we have made a number of a-SiC:H films using novel carbon feedstocks disilylmethane (DSM) and trisilylmethane (TSM). The TSM based films show significantly improved electron and hole transport, reduced CH_n and SiH_2 bond density, sharper Urbach absorption edge, and reduced sub-bandgap absorption. The DSM based films exhibit properties rather similar to those found in CH_4 based films without H-dilution (**13**). No further optimization of TSM and DSM based bulk films was attempted during this report period. It is important to note that these novel feedstocks are not commercially available and the syntheses of DSM and TSM are time-consuming, low-yield processes. More DSM and TSM have been synthesized, understandably in small quantities, at Solarex in order to further explore these materials. Preliminary data on device performance and stability of the DSM and TSM based materials will be described later.

We have further improved the optical and transport properties of CH_4+H_2 based a-SiC:H films with bandgaps between 1.9 and 2.0 eV by using moderate and relatively low deposition substrate temperatures (T_s) in the range of 170-250°C instead of the higher substrate temperatures (T_s=300-320°C) employed earlier. The high T_s recipe was published by A. Matsuda, et al. (**14,15**), who examined only electron photoconductivity and dark conductivity in their widegap CH_4+H_2 based alloys. The high (300°C - 350°C) T_s employed by these authors is believed to help desorb the undesirable CH_3 radicals from the surface (and to enhance the mobility of the precursors on the growth surface). Unfortunately, as demonstrated below, the electron photoconductivity or the mobility-lifetime product $\mu\tau$ alone is insufficiently reliable for judging the films' electronic properties. The comparison of a-SiC:H alloys deposited at different T_s is not straightforward since the lower T_s leads to wider bandgap due to higher hydrogen content in the film (assuming that the carbon concentration in the film is insensitive to T_s) when all the other parameters are held constant. This is illustrated in **Figure 2-13**, which shows the variation with T_s of the optical bandgap E_g defined as the energy at which the absorption coefficient equals $2x10^3$ cm^{-1}, the Urbach energy E_0, the defect related optical absorption at 1.2 eV or $\alpha_{1.2}$, the electron $\mu\tau$, and the room temperature dark conductivity. The optical parameters were all obtained from photothermal deflection spectroscopy (PDS). The films were all fabricated using a fixed H-dilution ratio $H_2/[CH_4+SiH_4]$ of 25:1. Although the high T_s films seem to show better properties, one can not conclude from **Figure 2-13** that high T_s is favorable

Figure 2-13. Variations with T_s of bandgap, Urbach energy, defect absorption at 1.2 eV, electron $\mu\tau$, and dark conductivity of $CH_4 + H_2$ based a-SiC:H alloys.

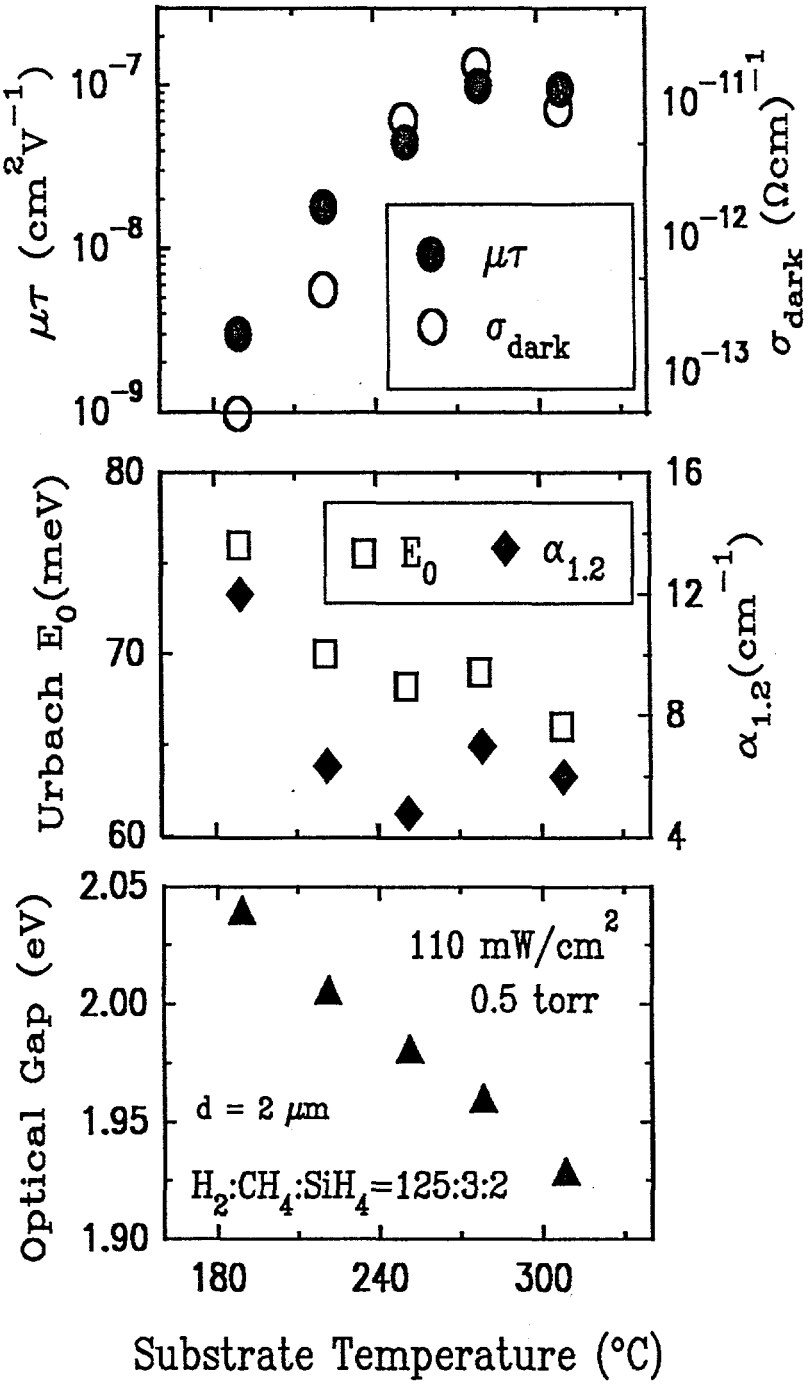

because the bandgap at high T_s is smaller and because the properties of a-SiC:H alloys are sensitive to the bandgap.

In order to observe the 'real' effect of T_s, we have synthesized a series of CH_4+H_2 based films, with nearly ***identical*** optical bandgaps of 1.96 ± 0.01 eV, by changing both the T_s and the gas phase CH_4 (and H_2) concentration while keeping the H-dilution ratio fixed at 25:1. The chamber pressure and rf power were kept constant. At a ***given*** bandgap, the lower T_s films would have more hydrogen but less carbon than the high T_s films (increasing either carbon or hydrogen content in the alloy would raise the bandgap). **Figure 2-14** shows the dependence on T_s of E_0, $\alpha_{1.2}$, $\mu\tau$ and L_{sspg} (the ambipolar diffusion length derived by the steady state photocarrier grating technique). It is evident that at the given bandgap 1.96 eV, the relatively low T_s results in better transport and optical properties. Incidentally, the relatively low T_s (e.g. $\leq$250°C) is desirable from the practical view of preparing solar cell i-layers or buffer layers (e.g., avoid dopant diffusion or desorption). Also, low T_s (e.g., < 200 °C) for the p-layer, which is deposited against the reduction-prone tin oxide, would be preferable when heavy hydrogen dilution is called for.

It should be stressed that, unlike the CH_4 based samples which are insensitive to film thickness > 0.5 μm, the CH_4+H_2 based materials show an apparent thickness dependence of the measured opto-electronic properties up to over 1 μm, as illustrated in **Figure 2-15**, which depicts the relationship between material properties and film thickness when all the other deposition parameters were kept nominally identical. The bandgaps for these films are 1.93-1.94 eV. In **Figure 2-15**, σ_{dark} and E_σ refer to the room temperature dark conductivity and its thermal activation energy (measured by temperature dependence of σ), respectively. The sample 'quality' is poorer below 1 μm and the benchmark parameters asymptote at film thickness near or greater than 1.5 μm. This apparent thickness dependence, widely observed for unalloyed a-Si:H, is probably a reflection of surface effects and band-bending which is more pronounced in films with lower bulk defect density (in this case the good CH_4+H_2 based alloys). However the likelihood that film properties change along the growth axis (i.e., reaction condition at the film growing surface evolves with time during deposition) cannot be ruled out. In any case, in order to obtain the so-called 'bulk' properties, films of thickness near 2 μm would be required. This means that very long deposition time is needed for each run (e.g., 15-20 hours) since the growth rate is about 1000 Å/hour under the aforementioned deposition conditions for CH_4+H_2 based specimens. Another difficulty introduced by the thickness requirement is that thick undoped films made at low T_s (< 250 °C) show increasingly poorer adhesion to the substrates such as quartz and crystalline Si as the substrate temperature is reduced. Adhesion to NiCr pads are somewhat better. The flaking or peeling off of the films made at low T_s (e.g., 170 and 190°C) occurred in a matter of several hours after the specimens were cooled down. Such films had to be measured immediately before wide-spread film peeling occurred. There has been little adhesion problem with

Figure 2-14. Variations with T_s of transport and optical properties for CH_4 + H_2 based a-SiC:H alloys with the same optical bandgaps.

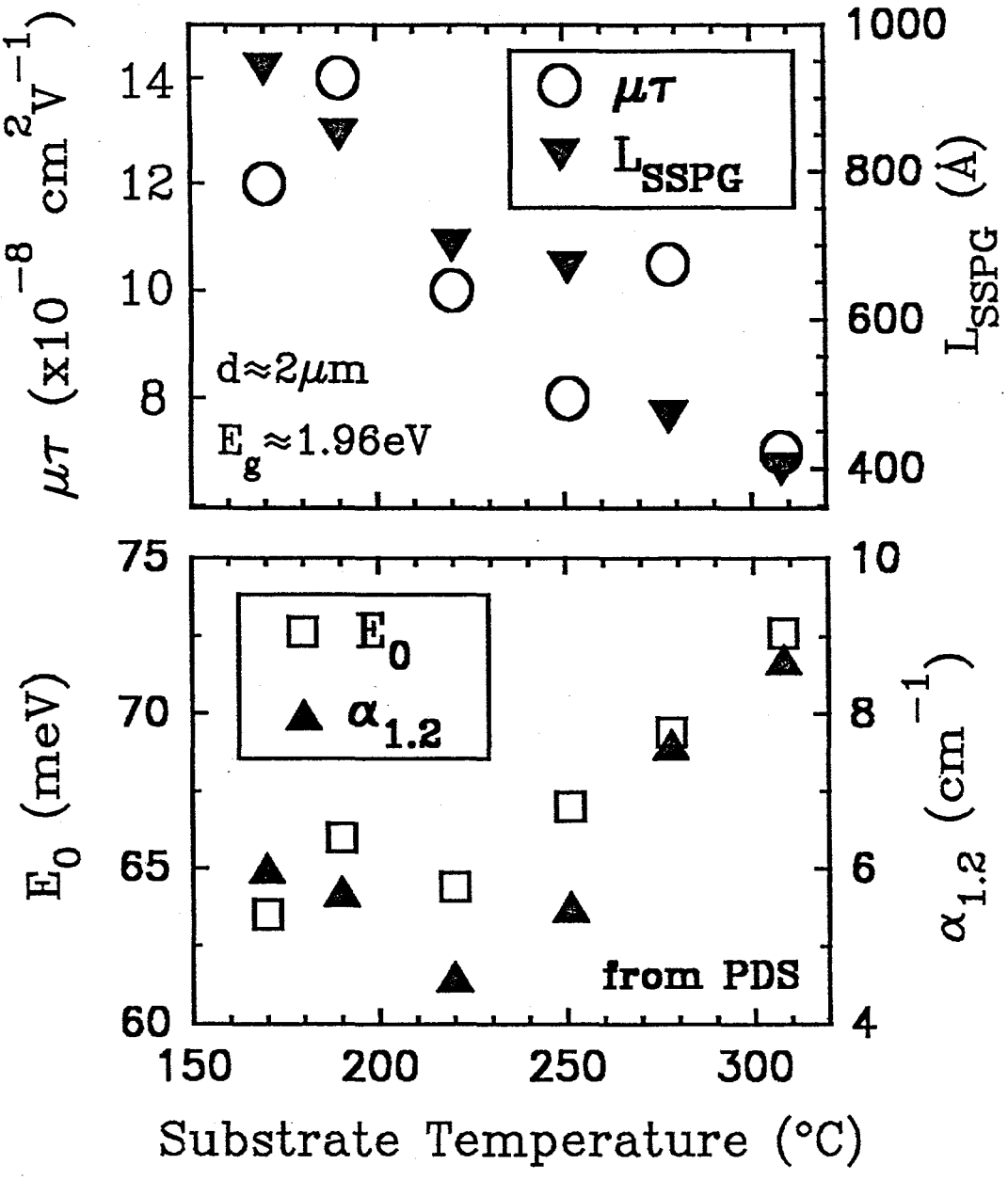

Figure 2-15. Thickness dependence of transport and optical properties for CH_4 + H_2 based a-SiC:H alloys of 1.93 - 1.94 eV bandgaps. The T_s is 220°C. H-dilution ratio is 25:1.

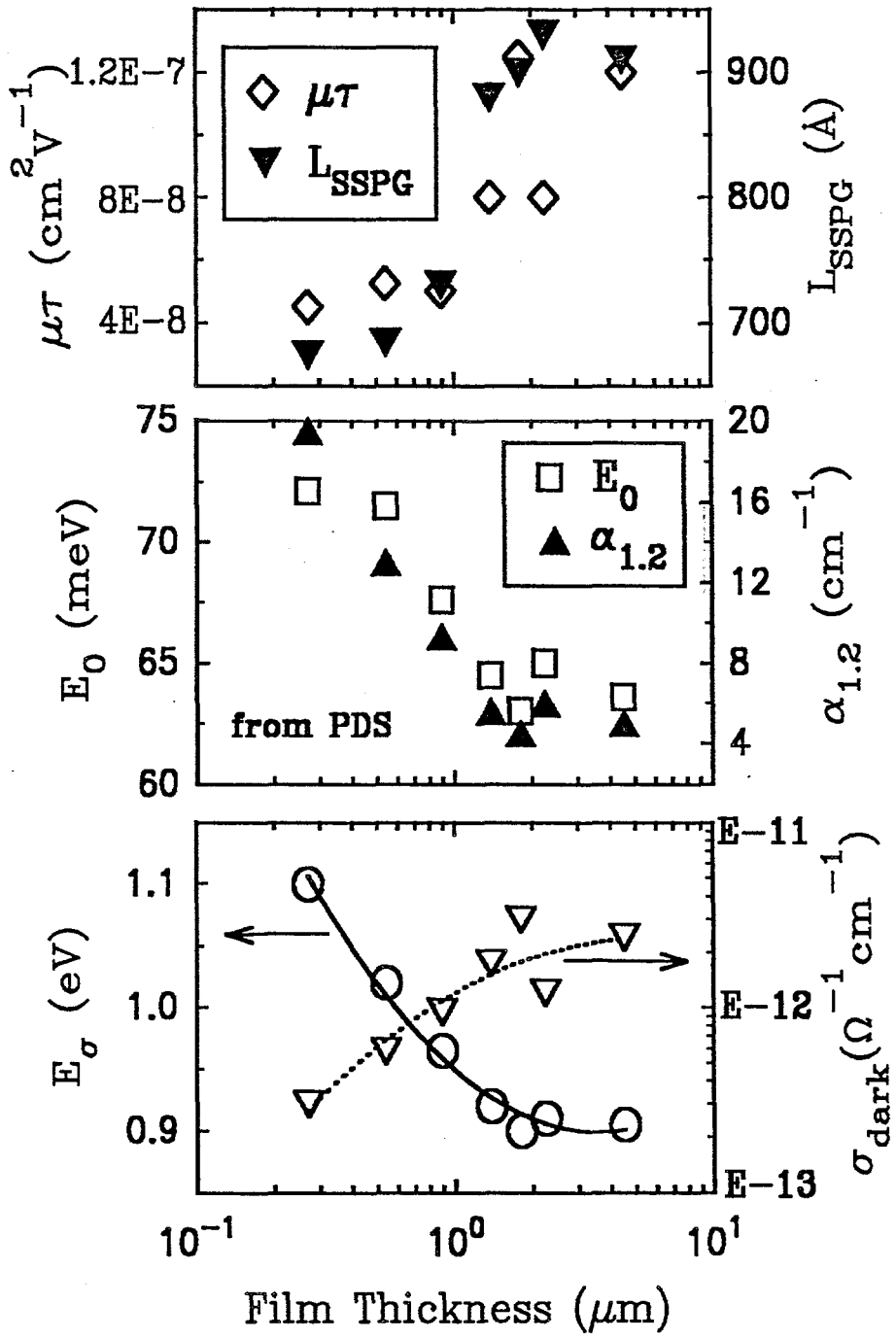

the high T_s samples. No T_s below 170°C was investigated (unsuccessfully tried once) since it appeared to be impossible to obtain non-flaking thick films for proper characterization.

Figures 2-16 through **2-19** compare our recent data on CH_4+H_2 films made at relatively low T_s with those of high T_s CH_4+H_2 based films and those from CH_4 based alloys without H-dilution, showing the variation with bandgap of electron $\mu\tau$, ambipolar diffusion length (or hole diffusion length) L_{sspg}, Urbach energy E_0, and sub-bandgap absorption $\alpha_{1.2}$, respectively. The infrared transmission spectra for representative alloys of 2.0 eV bandgap from the CH_4 and CH_4+H_2 recipes are displayed in **Figure 2-20**. The CH_4+H_2 based alloys, thicker than 1 μm, were all made with H-dilution ratios near 25:1. Remarkable improvements in film properties can be seen for hydrogen dilution, at any T_s studied. Also, consistent with **Figure 2-14**, **Figures 2-16** through **2-19** establish that the CH_4+H_2 recipe works best (as judged by the measured initial properties) at relatively low T_s instead of high T_s as previously proposed. Note that most of the films in the group labelled 170°C - 250°C in **Figures 2-16** through **2-19** were made at 220 °C. The data suggest that increasing hydrogen content is preferable to increasing carbon content in raising the bandgap using the CH_4+H_2 recipe (at least for E_g below 2.0 eV and in the 170°C - 320°C). The reduction of defect absorption and enhancement in phototransport for CH_4 +H_2 alloys, in comparison with CH_4 based alloys, are correlated with the reduction of methyl group (CH_n) absorption indicated in **Figure 2-20**. However, lower CH_n by itself does not necessarily mean better film properties since the T_s = 220°C films show superior E_0 and $\alpha_{1.2}$ than the T_s = 313°C films (in **Figure 2-20**) even though the latter appears to contain less CH_n. At the 2.0 eV bandgap, the Si-H_n stretch mode centered at 2080 cm^{-1} and the Si-H monohydride mode at 2000 cm^{-1}, which is dominant in unalloyed a-Si:H, is too weak to be observable even in the CH_4+H_2 based films. This may be partially due to the chemical shift of the Si-H stretch mode induced by adjacent carbon atom(s). In summary, the CH_4+H_2 recipe which works best at relatively low T_s has led to impressive improvements in optical and photo-transport properties of a-SiC:H with E_g < 2.0 eV compared to the conventional CH_4 based alloys. The remaining (important) question of whether the low T_s materials would lead to better solar cells and/or better device ***stability*** (compared to high T_s alloys of comparable bandgaps) is presently being studied.

To find out whether replacing hydrogen in CH_4 with halogen atoms such as chlorine (Cl) would improve a-SiC:H alloys, we have briefly explored another carbon compound, CCl_3D (a carbon bonded to three chlorine and a deuterium) by rf glow-discharge using the SiH_4+CCl_3D mixture. Although the CH_n methyl group concentrations were reduced by using CCl_3D instead of CH_4, a lot of CCl_n species were visible in the infrared transmission spectra indicating little improvement in the bonding structure of carbon species. The Urbach energy and sub-bandgap defect absorption are similar for films based on CCl_3D and CH_4 with comparable bandgaps. The CCl_3D based alloys have a somewhat lower $\mu\tau$ and σ_{dark} compared to CH_4 based alloys, as

Figure 2-16. Bandgap dependence of electron $\mu\tau$ of a-SiC:H alloys made from $CH_4 + H_2$ and CH_4 only (without H-dilution).

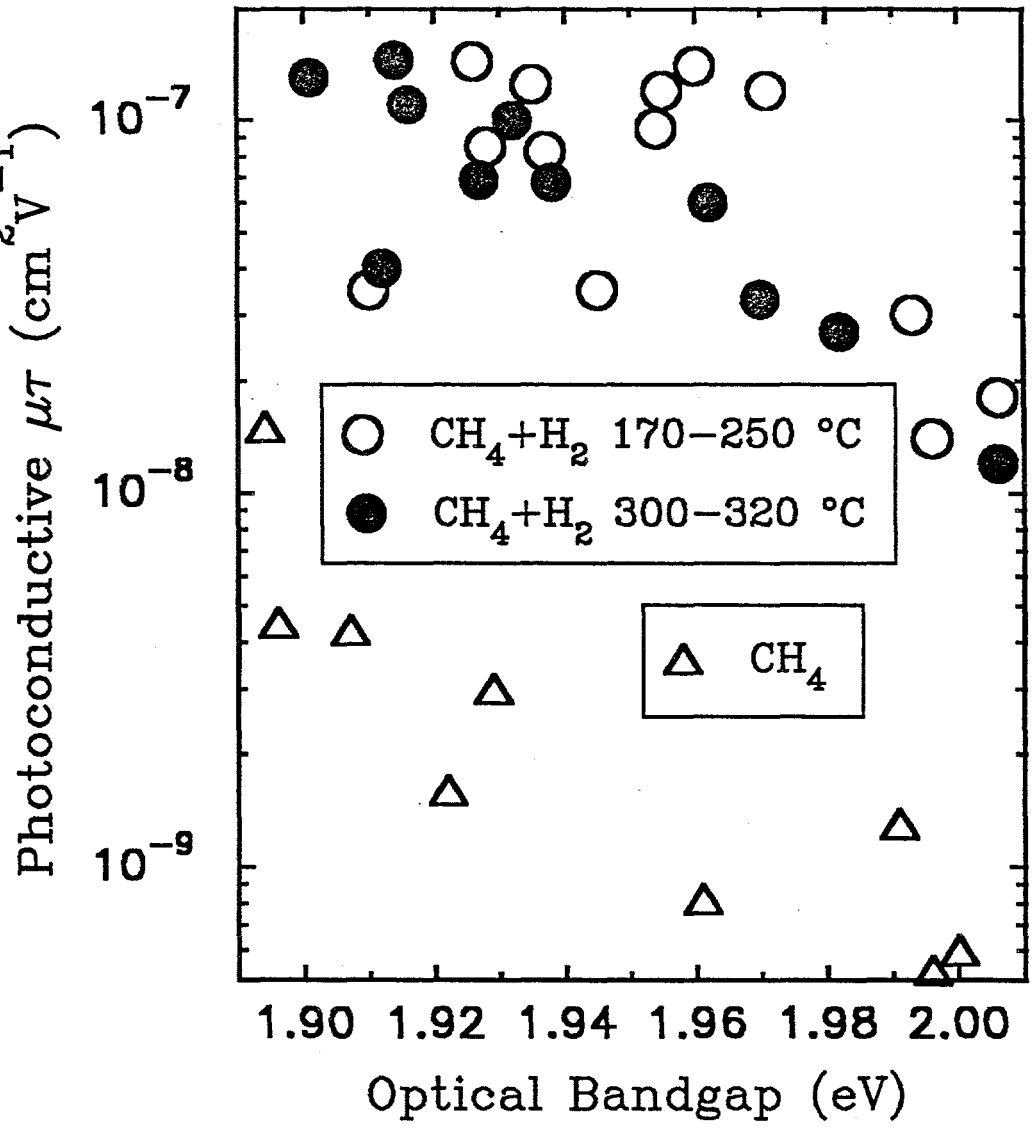

Figure 2-17. Comparison of hole diffusion length for a-SiC:H alloys made with and without H_2 dilution to the CH_4 + SiH_4 gas mixture.

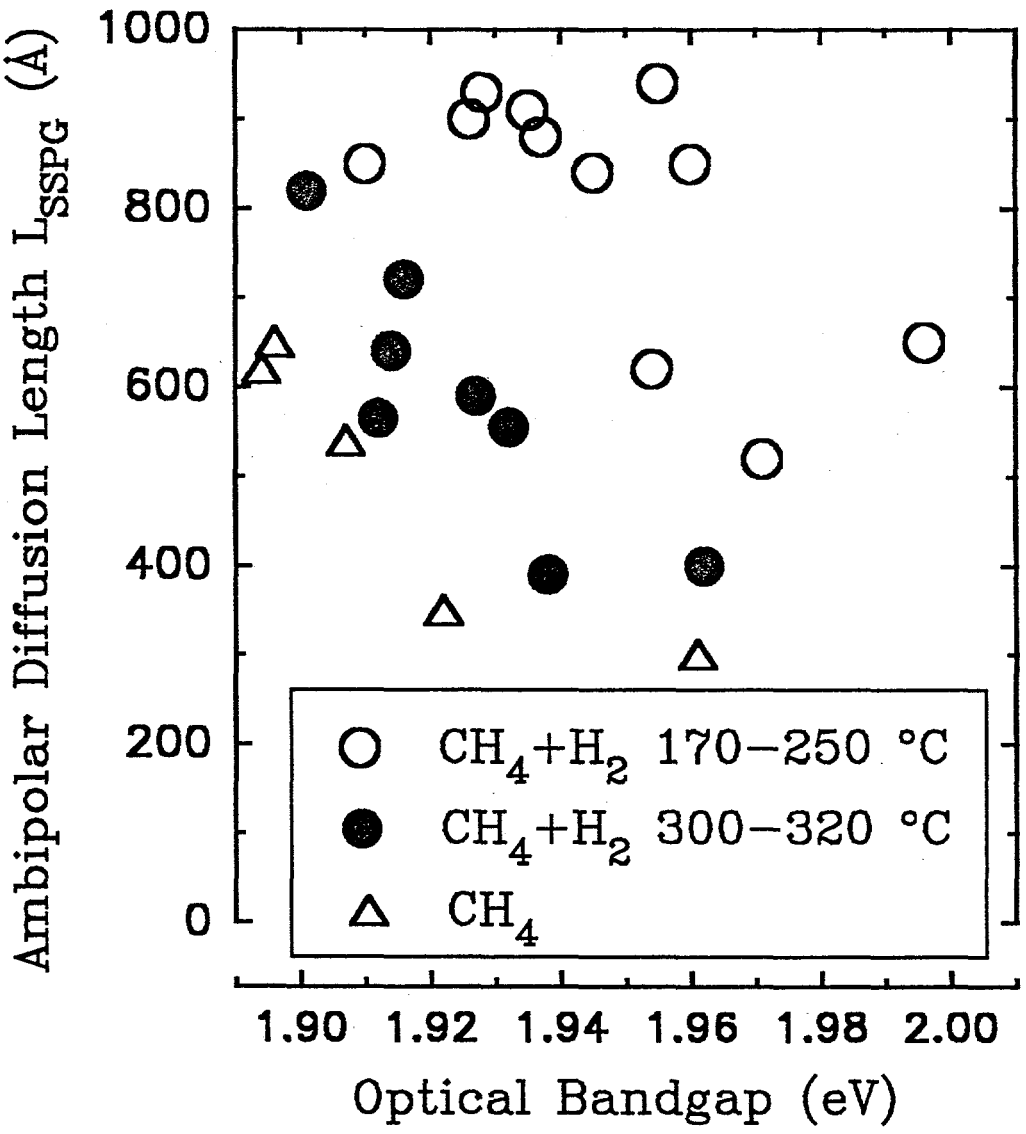

Figure 2-18. Urbach energy versus optical bandgap for CH_4 and CH_4 + H_2 based a-SiC:H alloys.

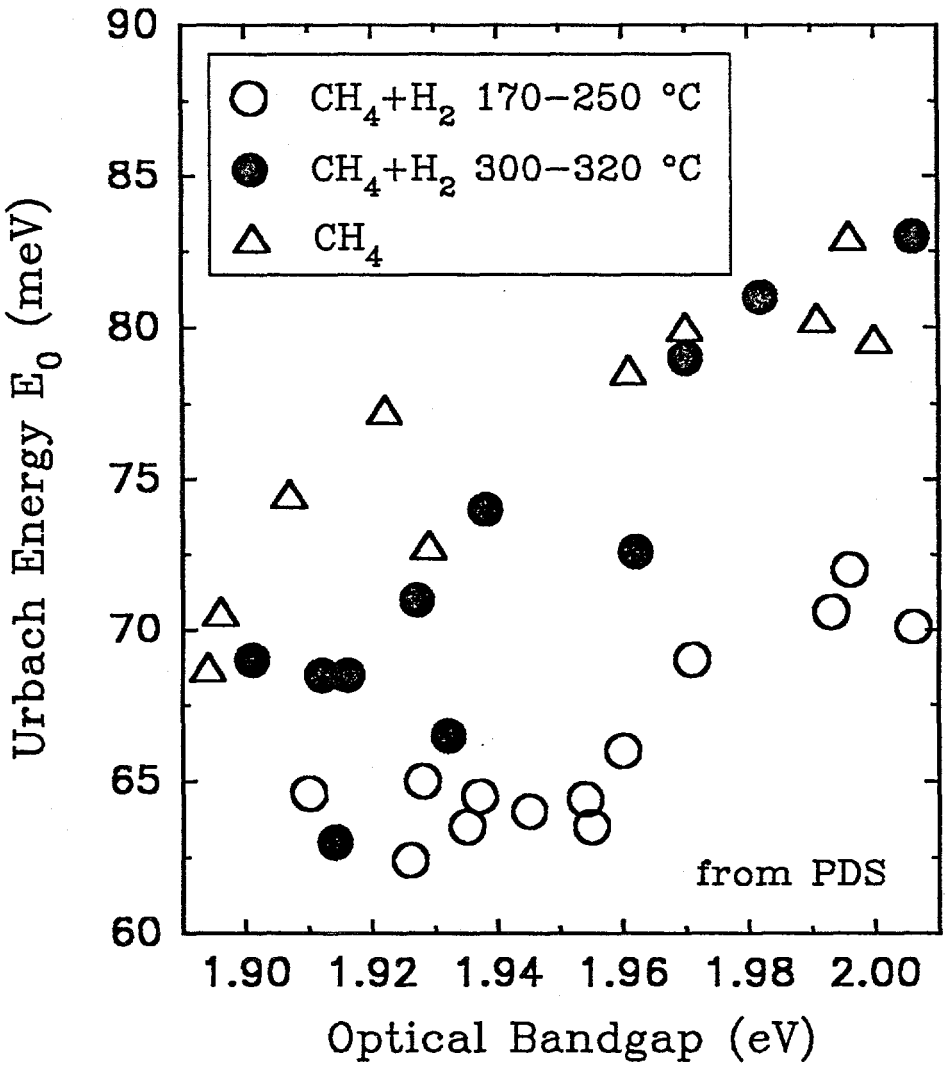

Figure 2-19. Bandgap dependence of defect absorption at 1.2 eV for a-SiC:H alloys derived from CH_4 + SiH_4 mixtures with and without H-dilution.

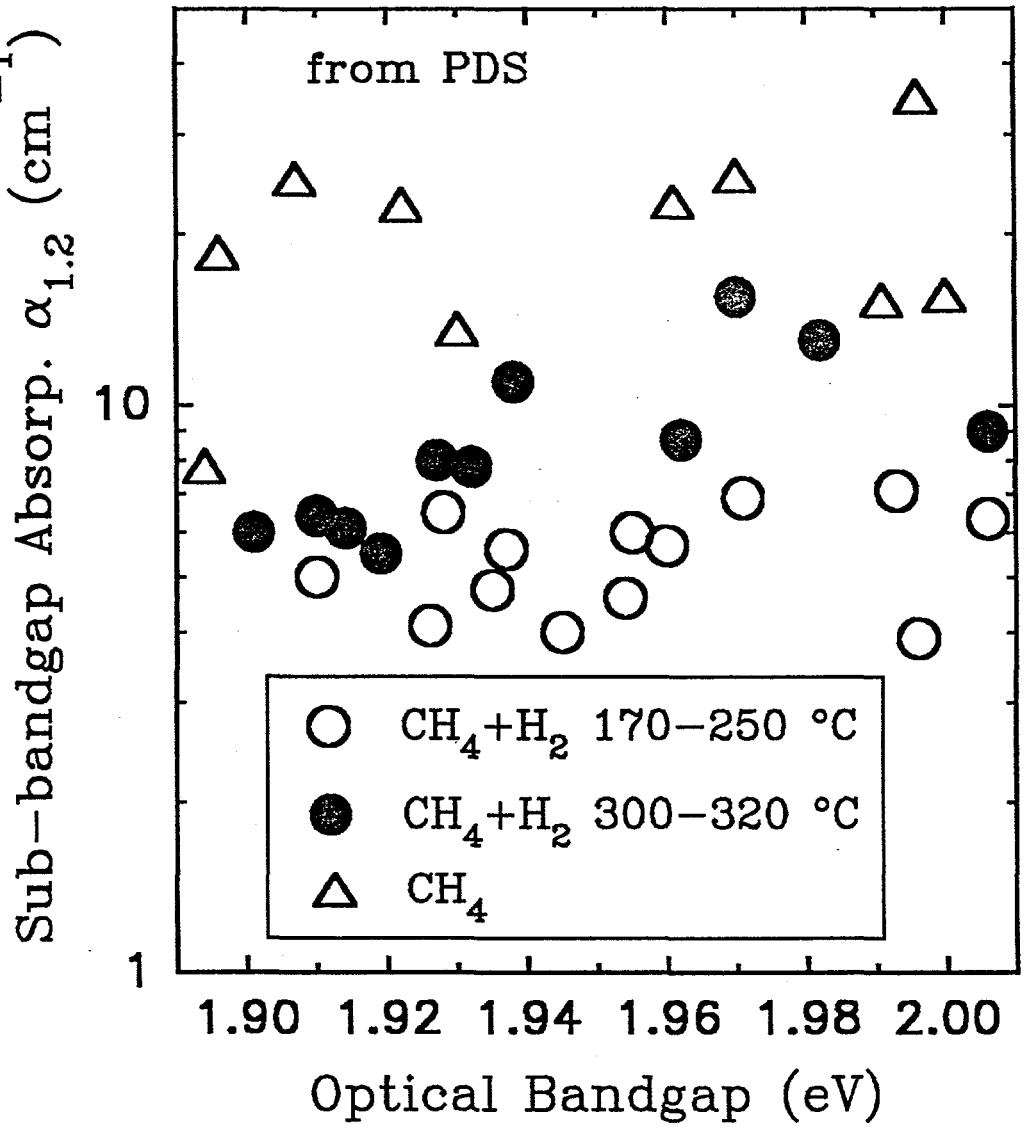

Figure 2-20. Infrared transmission spectra for representative a-SiC:H films based on CH_4 and $CH_4 + H_2$ recipes.

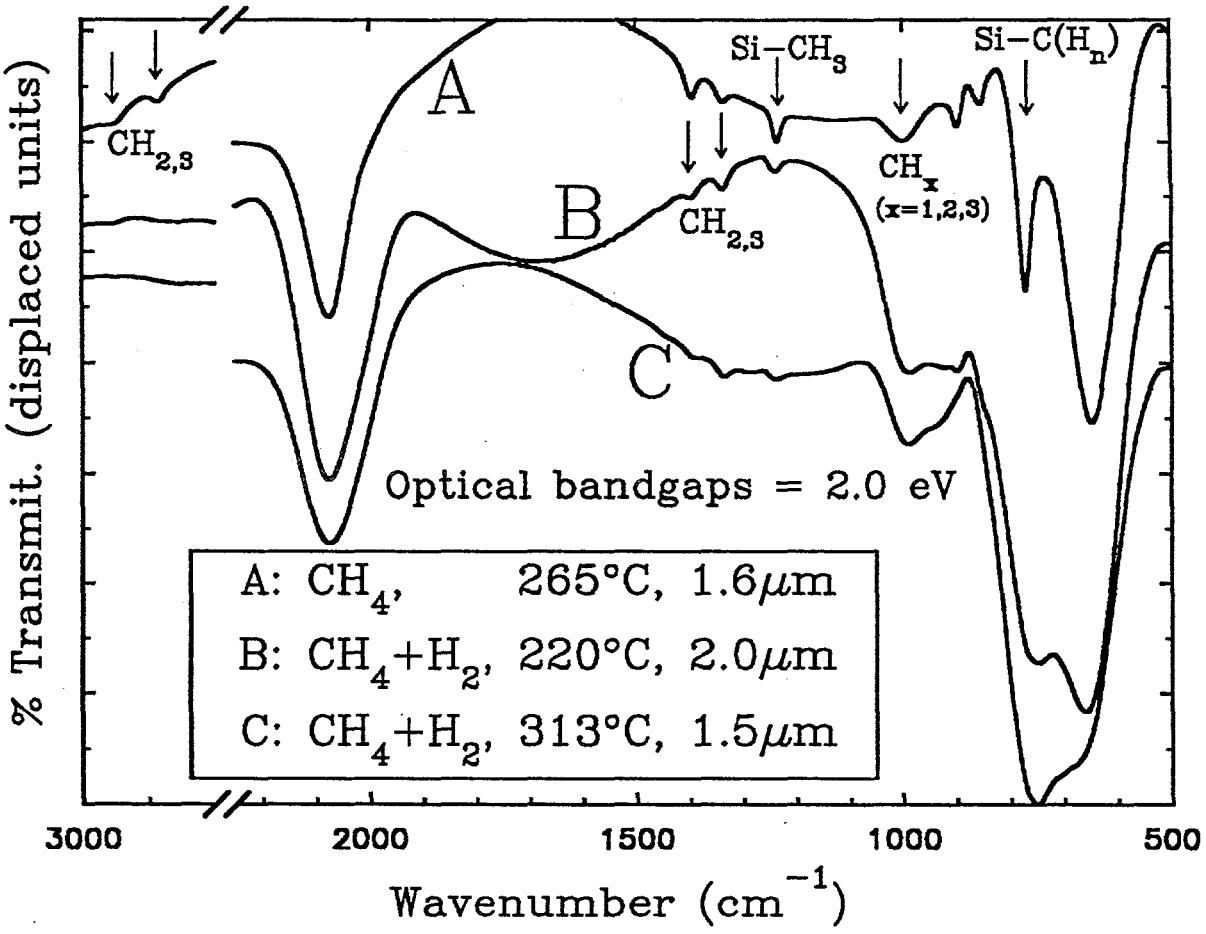

shown in **Figure 2-21**. However, the photosensitivity or the $\mu\tau/\sigma_{dark}$ ratio is comparable for the two groups of alloys. In view of the above negative results, no further study or device evaluation of the CCl_3D feedstock has been pursued.

2.4.2 Boron Doping Study of CH_4+H_2 Based Alloys

The difficulty in doping a-SiC:H alloys compared to a-Si:H may be attributable to the higher density of gap states and broader tail density of states (intrinsic and doping-induced) in the alloys which retards the movement of the Fermi level toward the band-edge. Also, bear in mind that the undoped a-SiC:H alloys have a much lower electrical conductivity than a-Si:H. The reduced defect density of the CH_4+H_2 based a-SiC:H described earlier is expected to result in more efficient doping in p-type a-SiC:H which is used as the window layer in p-i-n structure solar cells. Two methods of depositing boron doped a-SiC:H:B films using the CH_4+SiH_4+H_2+B_2H_6 mixture have been attempted. One is the normal continuous deposition. The other is to alternate film growth and hydrogen etching by striking a pure hydrogen plasma for 60 seconds after every 20 Å of film deposition. The hydrogen dilution ratio was kept at 25:1 and the T_s was 180°C - 190°C (except once at 300°C). **Table 2-4** summarizes the room temperature dark conductivity, σ_{dark}, and its thermal activation energy, E_σ, of these films. Also included for comparison is a film made from the conventional CH_4+SiH_4+B_2H_6 mixture using the recipe for the p-layer in p-i-n cells. The nominal gas phase ratio of B_2H_6 to SiH_4 + CH_4 was about 0.4% for of the films reported here (the true B_2H_6 content was probably lower due to the known instability or decomposition of B_2H_6 in the storage cylinder). The optical bandgap here is signified by E_{04}, the energy at which the optical absorption coefficient equals 10^4 cm^{-1}. (The usual definition of bandgap for undoped films at the lower absorption level of $2x10^3$ cm^{-1} is not appropriate here due to the broadening of the absorption edge caused by heavy doping and dopant alloying while the E_{04} gap is far less sensitive to this effect.)

Table 2-4. Properties of Boron Doped a-SiC:H Films by Two Deposition Methods

Type of Film	E_{04} Gap (eV)	σ_{dark} (S/cm)	E_σ (eV)	E_0 (meV)
CH_4	2.14	$6x10^{-7}$	0.45	214
CH_4+H_2 cont.*	2.13	$4x10^{-6}$-$6x10^{-9}$	'0.15'-0.5	110
CH_4+H_2 alt.**	2.13	$1x10^{-5}$-$5x10^{-9}$	'0.15'-0.6	?

* Continuous deposition.
** Alternating film growth and hydrogen etching.

Figure 2-21. Variations with optical bandgap of electron photoconductive $\mu\tau$ and dark conductivity for CH_4 (without H-dilution) and $C.Cl_3D$ based a-SiC:H alloys.

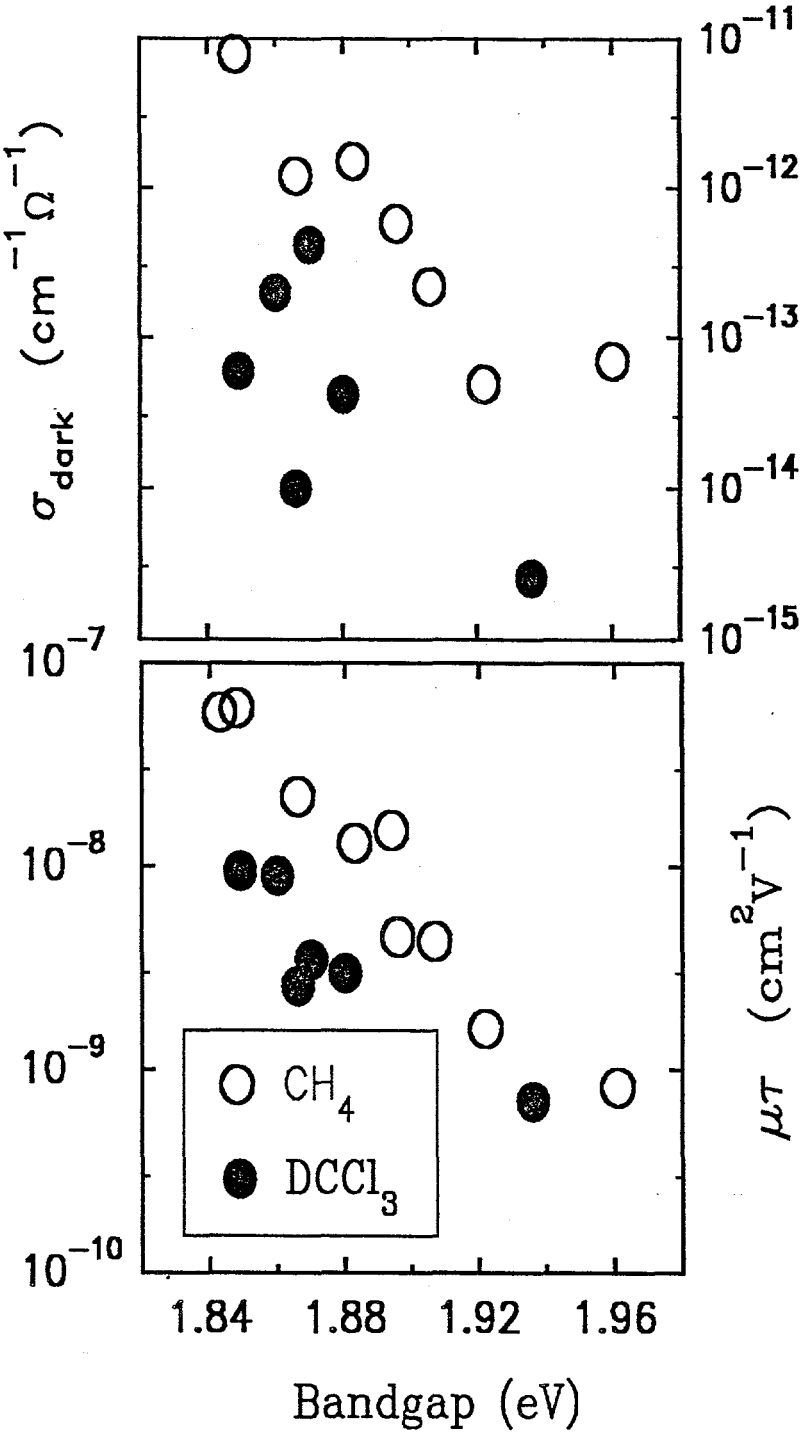

Higher conductivity, lower activation energy, and sharper absorption edge (smaller E_0) have been observed in some CH_4+H_2 based p-type films. However, a ***severe*** problem with our preliminary study of these films has been an unacceptably poor doping uniformity ***and*** an unacceptably poor reproducibility, particularly for the films prepared using the alternating growth/etch method. This is evident from the great scattering of the σ_{dark} and E_σ data obtained under nominally similar conditions. For example, some co-deposited films would differ in their σ_{dark} values by 2-3 orders of magnitude. The poor reproducibility and non-uniformity is believed to be related to the instability of the B_2H_6 gas and its reaction with the hydrogen-rich plasma (and the deposition hardware). Work is now under way to replace B_2H_6 with trimethylboron as the dopant source to solve the above problem. It appears that better p-type a-SiC:H films (with higher σ_{dark} and not-too-broad band edge) should be achievable but our present data are inconclusive. It is worth mentioning that TSM based p-layer, in place of the normal CH_4 based p-layer without H-dilution, has led to higher V_{oc} and good fill factor in simple a-Si:H p-i-n cells without any buffer (V_{oc} = 0.86V versus the usual V_{oc} of 0.83V - 0.84V). Further work of p-type material using the novel feedstock is planned.

We briefly explored another p-type dopant, gallium (Ga), in the gas phase doping of a-Si:H and a-SiC:H alloys by using trimethylgallium to compare with the conventional boron doping. The measurements of conductivity and its temperature dependence indicate that Ga doping effect does exist but it is not as nearly as efficient as boron doping (as judged by the change in σ_{dark} for a given percentage of dopant gas introduced). This may be due to the deeper position of the Ga doping levels in the bandgap. Another serious drawback of Ga doping is that the bandgap of the resulting material shrinks and the absorption edge broadens significantly (compared to undoped a-Si:H and a-SiC:H films) even at fairly low doping levels. The Ga doped films are visibly darker. In comparison, the boron doped films show relatively small (E_{04}) bandgap narrowing and band-edge broadening for comparable σ_{dark}. Thus, it appears that Ga doping has little practical value for a-Si:H based photovoltaic technology.

2.4.3 Stability and Device Performance

Simple single junction p-i-n type solar cells have been fabricated on glass/textured ZnO with a-SiC:H *i*-layers of near 1.90 eV bandgap using CH_4, CH_4+H_2, DSM, and TSM feed gases. The thickness of i-layers were varied from 1000Å to over 2000Å. The primary objective was to evaluate the light-induced degradation of devices prepared using various a-SiC:H feedstocks and dilution conditions. No effort was made to optimize the interface grading, p-layer, etc. The B_2H_6 doped p-layers were all prepared from CH_4+SiH_4 mixtures without H-dilution. The a-Si:H n-layers were deliberately made thick (500Å - 600Å) to simulate the condition of the top junction

in triple-junction cells (such that little light is reflected back into the i-layer due to strong n-layer absorption) and to alleviate shunting problems of thin cells. Most of the cells have Al back contact which has a relatively low (~ 50%) reflectivity. **Table 2-5** lists the parameters of representative a-SiC:H single junction cells made from different recipes. An unalloyed a-Si:H cell is included for reference.

Table 2-5. Initial Characteristics of Representative a-SiC:H Single Junction Cells.

Cell I.D.	Carbon Source	I-Layer Thickness	Bandgap (eV)	V_{oc} (V)	J_{sc} (mA/cm^2)	FF	η (%)
S10515ZD[a]	None	2,200	1.75	0.83	11.0	0.72	6.6
S10516ID	CH_4	1,300	1.90	0.90	5.4	0.53	2.6
S10725JD[a]	CH_4	2,000	~1.91	0.91	5.9	0.56	3.0[b]
S10515BD[a]	$CH_4 + H_2$	1,800	1.90	0.77	7.4	0.56	3.2
S10724HD[c]	$CH_4 + H_2$	1,300	1.90	0.86	7.6	0.57	3.6
S10515CD[a]	TSM	2,000	1.90	0.86	7.4	0.51	3.2
S10516GD[c]	TSM	1,100	1.89	0.90	6.0	0.70	3.8
S10523YD	DSM	2,300	~1.93	0.92	7.8	0.67	4.8
S10710UD[a]	DSM	2,300	~1.89	0.89	9.6	0.59	5.0[b]

(a) Cells used in stability comparison in **Figure 2-22.**
(b) ITO/Ag rear contact (higher current) and thinner p-layer.
(c) CH_4 buffer (without H) at p/i interface ~100Å.

Some interesting observations can be made concerning these cells. The CH_4 based cells have poor fill factors (FF) and comparatively low short circuit currents (J_{sc}), as expected for an i-layer material with poor transport properties, while the open-circuit voltages (V_{oc}) look reasonable for the given bandgap of the i-layer. DSM (disilylmethane) yields devices with the best initial performance, particularly fill factor, followed by TSM (trisilylmethane). It is difficult to understand why the DSM based cells (initially) perform so well given the rather poor transport properties of the DSM based films which, with the exception of mild improvement in hole diffusion length, are quite comparable to those of the CH_4 based films as described in the last report **(12)**. Perhaps a better p/i interface is formed due to the lower rf power used or due to the absence of CH_3 radicals found in the conventional CH_4+SiH_4 plasma. Thin cells using TSM show good parameters when made with a CH_4 or DSM buffer, without H-dilution, at the p/i interface. Deposition of TSM with hydrogen dilution directly against the p-layer has resulted in low V_{oc} and poor FF (see cell S10515CD in **Table 2-5**). More investigation of the TSM based cells is being conducted to conclusively determine whether the good transport properties of the TSM

Figure 2-22. Efficiency dependence on illumination time for p-i-n single junction cells using a-SiC:H i-layer with 1.9 eV bandgap prepared from different feed gas mixtures (*see* Table 2.5). The i-layer thickness is in unit of Å.

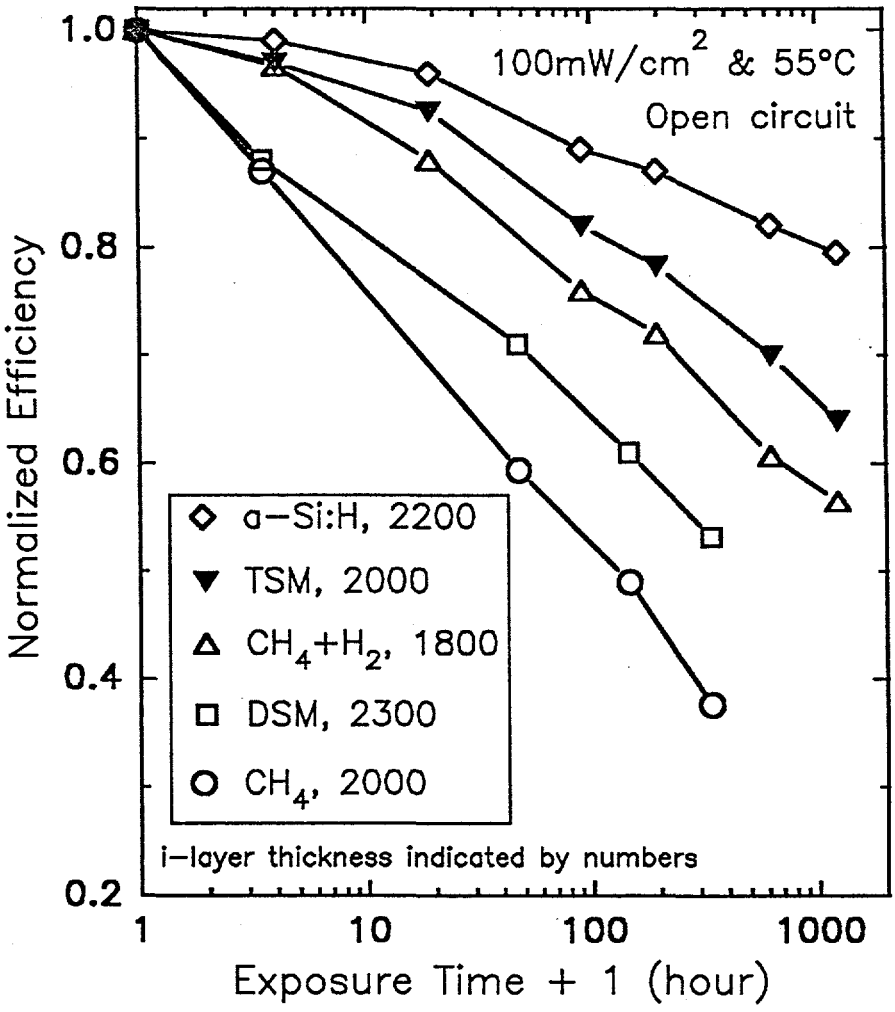

based films can translate into superior device performance. The CH_4+H_2 based cells, made at relatively high T_s of 305°C, are disappointingly poor in view of the good film transport (and optical) properties obtainable using the CH_4+H_2 recipe. The V_{oc} is particularly low for the 1.90 eV or so bandgap of the i-layer. The poor FF is similar to that of CH_4 based cells. No cell has yet been fabricated using the CH_4+H_2 formula at lower T_s which, among other things, may result in a better p/i interface by reducing the thermally activated dopant diffusion. We suppose the poor initial efficiency of the CH_4+H_2 based cells (and the TSM based cell S10515CD in **Table 2-5** which had H-dilution at the p/i interface) may be due to hydrogen bombardment at the p/i junction. The resulting damage or etching, possibly facilitated by the high substrate temperature, may have led to a high effective recombination rate. Damage to the p-layer may also reduce majority carrier mobility leading to "blocking" behavior. There may also be a band-edge mismatch between the p-layer, made without hydrogen dilution, and the i-layer made with heavy hydrogen dilution. Alternatively, one might speculate that the CH_4+H_2 based i-layer studied here is inhomogeneous and has a low-bandgap component (or phase) which could limit the V_{oc} below the value expected from the nominal bandgap of the i-layer. We are presently further evaluating the CH_4+H_2 recipe, under various conditions and in different deposition systems, to firmly establish its potential benefits.

The stability of the above single junction cells with a-SiC:H i-layers were tested under simulated AM1.5 illumination (100 mW/cm^2) at 55°C. **Figure 2-22** shows the normalized cell efficiency as a function of illumination time for cells with near 1.90 eV gap i-layers (except the a-Si:H reference cell) of comparable thickness near 2000Å prepared from different recipes. The initial parameters of the cells, without any buffers, have been given in **Table 2-5**. The relative degradation rate of thinner cells (1000Å - 1300Å) from various feedstocks are qualitatively similar to that shown in **Figure 2-22**. Not surprisingly, the a-Si:H cell exhibits the least amount of degradation despite the higher photo-generation rate due to its narrower bandgap (and higher optical absorption). What is notable and encouraging is the reduction in instability of the TSM and CH_4+H_2 based devices, whose data are nearly within the experimental error of each other, compared to the far poorer stability of the CH_4 based cell. The DSM based cells appear to experience slightly slower photo-degradation when compared to the CH_4 based cells as judged by the data from several cells of various thickness. The improved stability of the TSM and CH_4+H_2 based devices seems to be related to the reduced densities of SiH_2 and CH_n bonds evident in the infrared vibrational spectra compared to the CH_4 and DSM based materials which exhibit rather strong 2080 cm^{-1} (due to SiH_2 or Si-H on micro-void surfaces) and CH_n absorptions. The broad Urbach edge in the CH_4 and DSM based materials may be indicative of a higher density of potential sites for photo-induced metastable defects. The TSM and CH_4 + H_2 based cells (and a-Si:H cells) with CH_4 or DSM p/i buffers degrade notably faster compared to those cells without such thin (100Å - 200Å) buffers of about 1.90 eV bandgap. From our preliminary data it

appears hopeful that thin a-SiC:H layers (e.g., < 1000Å) with 1.9 eV bandgap can be made reasonably stable. This argues well for their practical use as the top junctions of a-Si:H based triple-junction cells or as p/i buffer layers in cells with a-Si:H (or possibly a-SiGe:H) i-layers.

We have also explored the effect of illumination on the properties of a-SiC:H films prepared by different means. No change in the hydrogen bonding structure (SiH_n and CH_n) for a-Si:H *and* a-SiC:H (E_g up to 2.0 eV) films is observable in the infrared spectra after high intensity light soaking with a dosage roughly equivalent to 100 years of AM1.5 illumination at about 70°C. Therefore the poorer device stability of a-SiC:H is not correlated with any massive hydrogen bonding rearrangements. Photothermal Deflection Spectroscopy (PDS) derived sub-bandgap optical absorption spectra were taken for a-SiC:H alloys of 1.90 eV gap from different recipes after 80 hours of illumination whose intensity was 20 times of AM1.5 (2000 mW/cm^2) at 60-70°C. **Table 2-6** lists the defect absorption at 1.2 eV ($\sigma_{1.2}$) and Urbach energy (E_0) for the films before and after the light-soaking. Also listed is the data of an a-Si:H film for comparison. (Further illumination on the a-Si:H film had little effect on its PDS spectrum). The CH_4 film shows the most increase in sub-gap absorption as expected. However, unlike the device stability data which shows the DSM based cells are almost as unstable as the CH_4 based cells, the DSM ***film*** shows a smaller $\alpha_{1.2}$ after illumination relative to the CH_4 film. After the extended illumination the DSM film has an $\alpha_{1.2}$ comparable to that of the TSM and CH_4+H_2 films, although the initial $\alpha_{1.2}$ for the DSM film is rather high. Hence, ***the PDS derived defect absorption is unlikely to be a reliable predictor for the relative stability of a-SiC:H devices.*** The E_0 values for the CH_4 and DSM specimens are higher, both before *and* after light-soaking, than those for the TSM and CH_4+H_2 derived specimens. For the limited cases studied, there exists a qualitative correlation between E_0 and the degree of instability for a-SiC:H based devices. That is, material with higher E_0 gives more unstable i-layer.

Table 2-6. Comparison of $\alpha_{1.2}$ and E_0 of a-SiC:H Films with 1.90 eV Bandgap Before and After Accelerated Photo-Degradation.

Sample I.D.	Carbon Source	$\alpha_{1.2}$ initial (cm^{-1})	$\alpha_{1.2}$ after (cm^{-1})	E_0 initial (meV)	E_0 after (meV)
S01210JF	none (a-Si:H)	2.5	29	55	63/64
S10120SF	CH_4	20-25	97	74	81
S10129CF	CH_4 + H_2	6	56	69	76
S10107JF	DSM	12	59	72	80/81
S10329QF	TSM	5	50	63	73/74

We have also measured the dependence of electron photoconductivity versus illumination time for 1.90 eV bandgap a-SiC:H films deposited from different gas mixtures. The light source was a HeNe laser whose intensity was adjusted by neutral density filters. The photogeneration rate was kept the same, for all the films studied, at about 10^{21} $cm^{-3}sec^{-1}$. An a-Si:H film was also measured for comparison. The normalized photocurrent versus excitation time is plotted in **Figure 2-23**. The photocurrent of the CH_4+H_2 based film degraded the fastest presumably because of its high initial value of $\mu\tau$ (the a-Si:H film, though, had the highest initial photoconductivity or $\mu\tau$). The normalized $\mu\tau$ degradation rates for CH_4, DSM, and TSM based films were about the same. The comparison of the photoconductivity degradation data with the cell degradation data (**Figure 2-22** and **Figure 2-23**) indicates that, at least for a-SiC:H alloys, ***photoconductivity alone is not an appropriate indicator for stability of bipolar devices such as solar cells*** (contrary to the assumption used by some research groups in studying material stability). This is consistent with our view that film measurements provide, at most, a rough guide to device performance. Film properties as measured by PDS, SSPG photoconductivity are a necessary, but by no means, sufficient condition for adequate device performance. We comment that, in principle, the degradation of ambipolar diffusion length (hole diffusion length) should be a good gauge for device stability. However, the low photoconductivity of the a-SiC:H films after severe degradation makes the measurement *and* the data analysis rather difficult.

In summary, the structural, optical, and phototransport properties of a-SiC:H films have been significantly improved using either hydrogen dilution of CH_4, particularly at moderate and relatively low substrate temperatures, or the novel carbon source TSM. The simple p-i-n single junction solar cells using a-SiC:H i-layer based on DSM and TSM recipes show much improved initial performance than cells based on the conventional CH_4+SiH_4 mixture. The TSM and CH_4+H_2 based cells, with bandgap near 1.90 eV, show considerably reduced degradation in efficiency after extended optical illumination compared to CH_4 and DSM based cells of comparable i-layer bandgaps and thickness. There exists no simple correlation between the cell stability and the stability of such film properties as photoconductivity and sub-bandgap defect absorption for a-SiC:H alloys. The performance of cells based on the CH_4+H_2 recipe at high temperature has been disappointing and further work is being conducted to optimize the device structure and the i-layer deposition conditions (e.g., lower temperature) using this promising recipe which is much more practical and convenient than the recipes based on novel carbon feedstocks (e.g., TSM).

Figure 2-23. Normalized photocurrent versus time of continuous illumination for a-SiC:H films with 1.90 eV bandgap (except the a-Si:H reference film) derived from different gas mixtures.

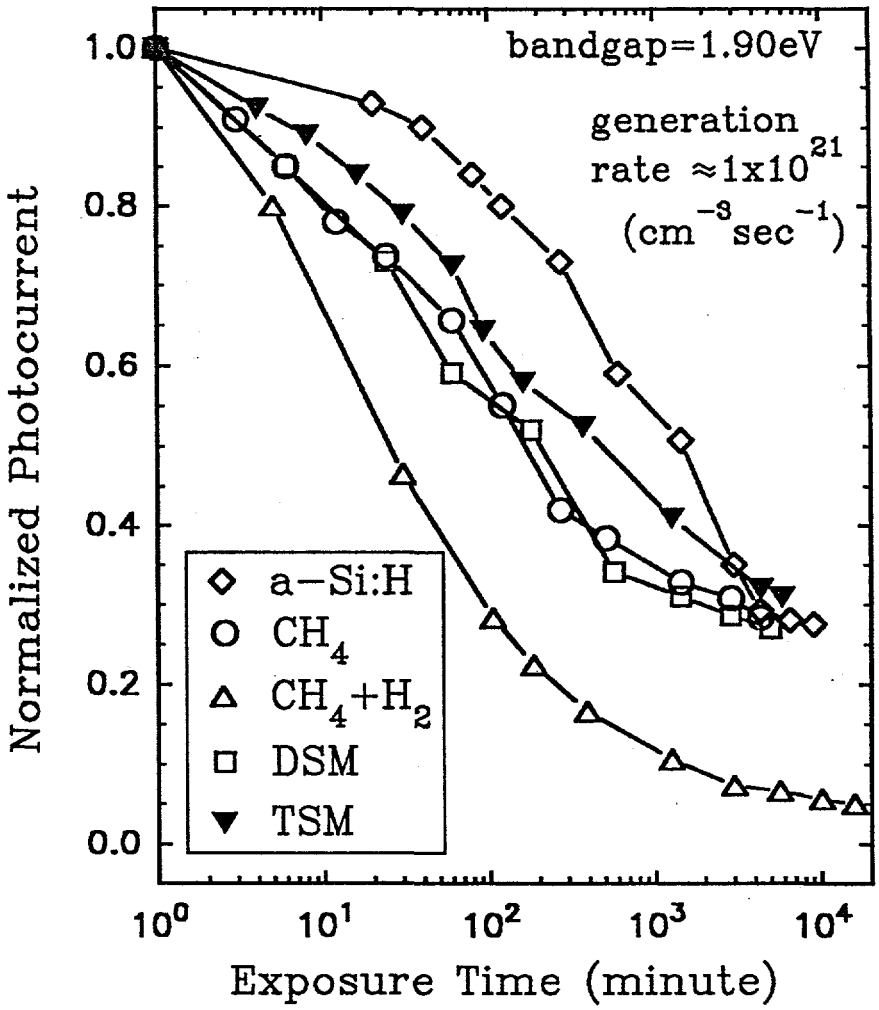

3.0 TASK II: NON-SEMICONDUCTOR MATERIALS RESEARCH

The purpose of this task is to prepare, characterize, and optimize the structural, electrical, chemical, and optical properties of the non-semiconductor materials that are required for the fabrication of modules utilizing the semiconductor thin-film materials developed in Task I. The goal is to support the demonstration of stable triple-junction cells and modules by developing improved transparent and reflecting contacts and other non-semiconducting components.

3.1 Substrate Materials

Glass

Because of its proven performance, availability, and low cost, glass has become the substrate of choice for single as well as multijunction module development at Solarex. To date, in our research activities, we have used Corning 7059F fused pyrex at a size of 12" x 13" x 0.043". This choice was made because of its chemical purity and high optical transmission. However, this type of glass is far too costly (~$10/ft^2) for commercial use in multijunction module manufacture, and the 0.043" thickness would not provide sufficient strength for practical large-area modules.

During this period, we have qualified and introduced a low-iron sodalime glass into the research activity. Aside from the low-iron feature, it has the same physical size and finish as the soda lime glass used in Solarex' thin-film manufacturing line. The optical transmission of this glass as compared to 7059F pyrex and the sodalime glass is shown in **Figure 3-1.** The transmission for the low iron glass is slightly lower (~1%) than the 7059F because it is twice as thick. Before the low iron glass will completely replace pyrex in our research, comparisons of its use in critical process steps and in cell and module performance must be made. Such evaluations were conducted during this period. A comparison of module performance between films and devices made on low-iron glass and pyrex is given in **Table 3-1.** Overall the data shows little difference in performance with the exception of slightly higher currents in the case of the low iron glass for the triple-junction modules.

3.2 Transparent Front Contacts

3.2.1 Textured Tin Oxide (SnO_2)

One major problem area reported previously and discussed in greater detail in Section 4.0 is the limitation of performance and stability caused by excess shunt-leakage currents. One cause is

Figure 3-1. Comparison of transmission spectra for 7059F, sodalime and low-iron glass

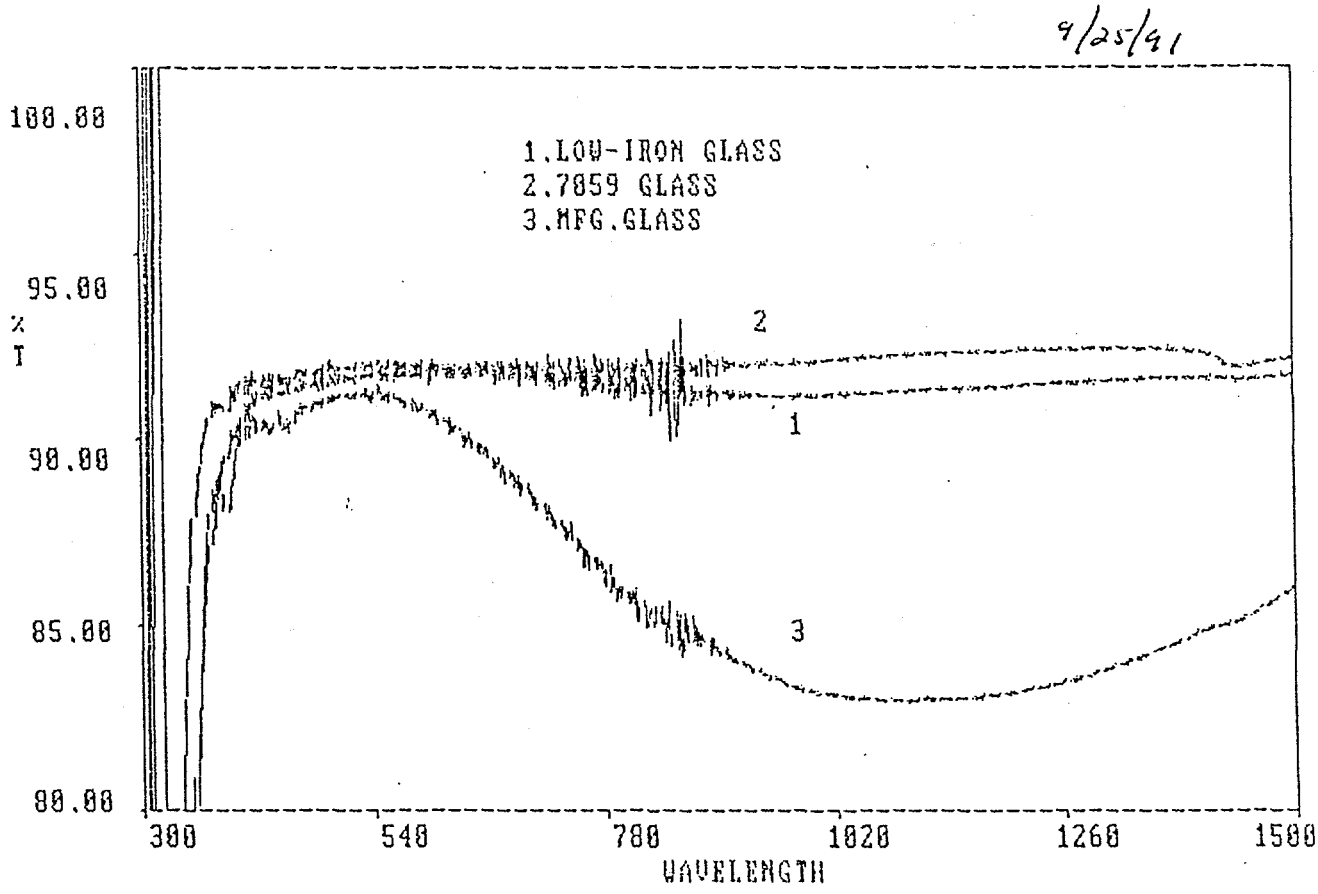

Table 3-1. Comparison of Module Performance for Low-Iron Glass vs. Pyrex.

Module #	Substrate	I_{sc} mA	FF	V_{oc} (V)	Eff (%)
Triple					
A1298-1	7059	208	0.664	59.4	8.77
A1298-2	Low Fe	211	0.659	59.5	8.84
A1298-3	Low Fe	213	0.663	59.6	8.97
Tandem					
L1302-1	7059	340.4	0.602	39.4	8.63
L1302-5	Low Fe	340.3	0.599	39.8	8.67

thought to be particles and/or defects found on or imbedded in tin oxide films. We have reported a description and classification of such particles previously. During this period, we have made attempts to reduce particle formation as well as to determine which particles are most harmful.

Our previous classifications of particles were based on size and shape as seen in photomicrographs. The height of such particles was estimated by optical means. We have now used the stylus-type surface profiler operating in a "surface texture" mode to estimate the vertical height of ***small*** particles which appear to be about 1 micrometer in diameter. A typical profile of a region on the surface of a tin oxide sample containing a large density (~10^4/cm) of such particles is shown in **Figure 3-2.** Surprisingly, the peak-to-peak height of the particles is about 1200Å, which is only 50% higher than the average peak variation of the tin oxide crystals. We also know from the analysis conducted by Art Nelson at NREL that the particles are composed primarily of SnO_2 with only trace amounts of Cl, sometimes found at the particle site. These sites the probably do not cause thin weak regions or pinholes in the amorphous silicon films. If excess leakage currents are induced by these sites, the cause is more subtle, perhaps resulting in poor device quality material grown at the base of the peaks near the particles. Such a mechanism has been proposed by Sakai, et al. **(16)** to explain low V_{oc} in their tandem solar cell devices.

Large particles (> 5 μm) continue to be the obvious causes of shunt currents. These particles generally come from thick tin oxide material flaking from interior furnace parts. In our recent experiments, we have shown that the furnace conveyor belt to be a major source of these large particles. Improvements in belt cleaning as well as other factors related to limiting excessive film growth and peeling of furnace parts have led to a reduced particle count for tin oxide films.

Figure 3-2. Surface profile scan of tin oxide film over a region containing a high density of particles. One particle is located between 20 - 25 micrometers.

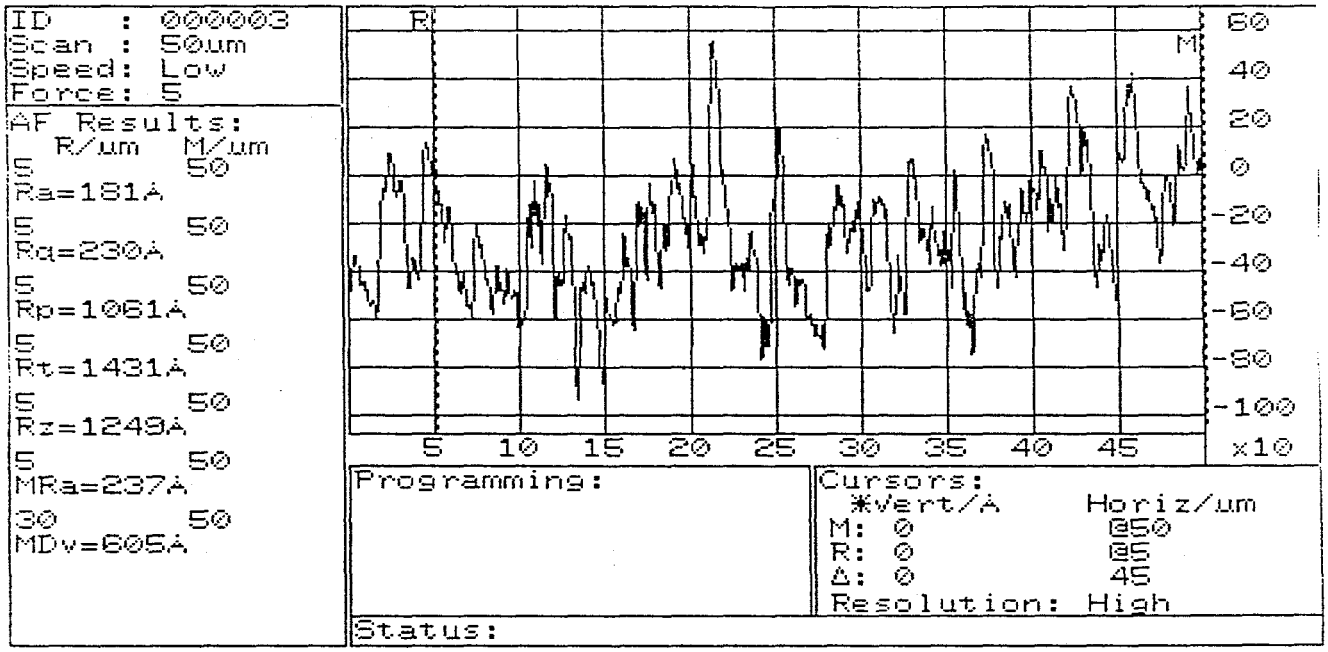

In the area of parameter optimization of tin oxide, during this period, we have achieved higher conductivity films. This work was started on the smaller R&D belt furnace which is now dedicated to ZnO research. A typical plot showing the range of results for conductivity versus HF flow is shown in **Figure 3-3.**

3.3 Atmospheric Pressure Chemical Vapor Deposition (APCVD) of ZnO

Although textured tin oxide (SnO_2) is currently used as a front contact layer for solar cells and modules, optical analysis of the amorphous silicon multijunction structure indicates that the present SnO_2 material used in the solar cell front contact accounts for significant (8% - 10%) optical losses. Efforts to reduce these optical losses centered around minimizing optical absorption and increasing light scattering while improving the electrical conductivity of the transparent front contact by employing ZnO.

Zinc oxide (ZnO) films offer special advantages over SnO_2 films. A lower optical absorption in the blue region of the spectrum is expected from zinc oxide films because of a larger bandgap **(17)** (3.2 eV) compared with the bandgap obtained with tin oxide films (3.0 eV). Doped zinc oxide can be prepared with higher conductivities using a number of dopants (fluorine, aluminum, or boron) than tin oxide films of equal thickness. In addition, zinc oxide is more resistant to reduction by the hydrogen plasma encountered during a-Si:H deposition. Thus, it should be possible to produce an optically transparent window in devices using hydrogen dilution. Furthermore, zinc oxide is more easily etched with dilute acid making equipment maintenance easier; conversely, the greater "softness" of the film may give rise to handling problems.

Zinc oxide can be prepared by Low Pressure Chemical Vapor Deposition (LPCVD), Atmospheric Pressure Chemical Vapor Deposition (APCVD), spray pyrolysis, sputtering, and a number of other methods **(18)**. The chief advantage of APCVD of zinc oxide is that it would utilize the existing equipment employed for SnO_2 deposition. By operating at atmospheric conditions no complex vacuum systems are needed such as is required for LPCVD of zinc oxide.

Atmospheric deposition furnaces can be operated continuously and are inherently faster and safer than vacuum systems that require batch processing with pumpdown steps. As we will see later, different deposition techniques produce zinc oxides with far different properties. APCVD zinc oxide has excellent optical and electrical properties for a front contact in a-Si:H photovoltaic devices.

Figure 3-3. Sheet resistance of SnO_2 substrate along with others fabricated on ZnO substrates (see Figure 3-14).

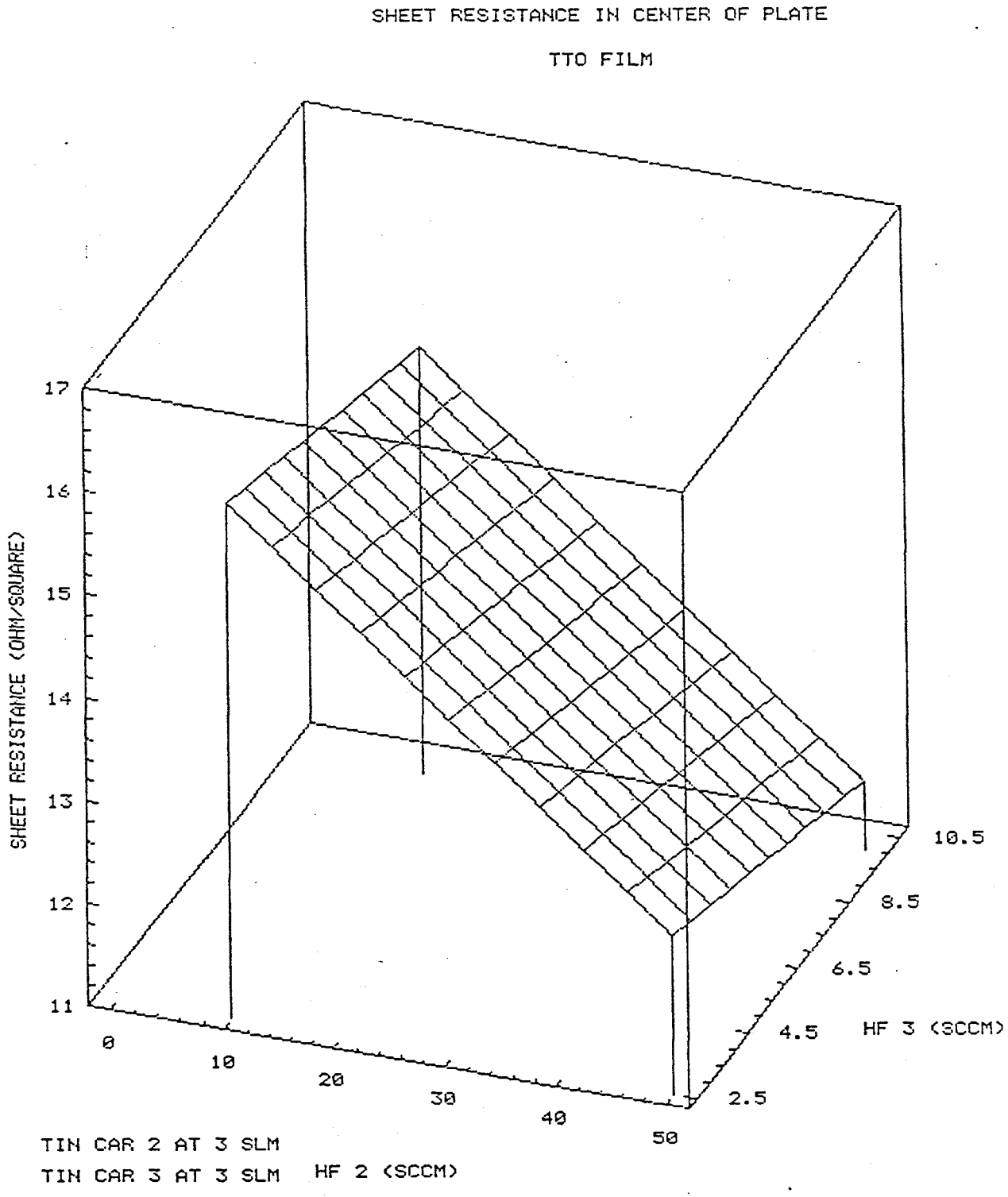

Installation and modification of a Watkins-Johnson furnace for the atmospheric deposition of zinc oxide films by chemical vapor deposition has been completed. Depositions were carried out on 3" x 3" pieces of Corning 7059 glass. As indicated in **Figure 3-4**, the furnace carries substrates on a moving belt through the furnace, under the deposition heads, producing a uniform conducting film. Movement of the substrate during APCVD of ZnO was found to be necessary based on initial studies with a deposition system that had a static substrate. In that study, it was found that in a wide range of zinc oxide deposition conditions it was not possible to obtain films with uniform optical and electrical properties using atmospheric deposition when the substrate remained in a fixed position. The inability to prepare uniform ZnO samples at atmospheric pressure without sample movement is related to the rate of diffusion of reactants to the substrate surface. In contrast, in LPCVD (pressures of 1-50 torr) of ZnO, the low pressure permits rapid gas phase diffusion of reactants; hence, batch systems with immobile substrates yield uniform films.

The zinc source for the APCVD furnace is the commercially available pyrophoric liquid (boiling point 118°C) diethylzinc (DEZ) that is thermally stable in the absence of air. A number of oxygen containing compounds (H_2O, O_2, N_2O, methanol, tetra-butyl alcohol, etc.) **(19)** have been reported in the literature to react with DEZ to give ZnO films. The best results for atmospheric deposition of ZnO have been obtained with anhydrous ethanol **(20)**. The reaction between DEZ and ethanol is given by:

$$Zn(CH_2CH_3)_2 + CH_3CH_2OH \dashrightarrow ZnO + C_2H_4 + 2C_2H_6$$

In practice, the process of film formation is conducted by combining DEZ and ethanol in a deposition head supplied by metal bubblers heated to above room temperature. The bubblers were fed a nitrogen carrier gas through a mass flow controller with the precise level of DEZ and ethanol determined by the bubbler temperature and the vapor pressure of the liquid. The reactant lines were heated to above the bubbler temperature to ensure that no liquid condensed in the lines. In addition to the main reactants, trace amounts of water vapor were added to the ethanol vapor to improve film properties.

The major variables such as oven temperature, HF flow, DEZ flow, water vapor flow, dilute nitrogen flow rates, exhaust rate, and belt speed were examined to optimize uniformity, conductivity, and transmission. To obtain sufficiently thick films (0.3 - 1.0 μm) a belt speed between 3" to 6" per minute was used. In early experiments, there was a tendency for heads to become clogged by ZnO powder. This was eliminated by careful adjustment of exhaust and reactant flows. It was necessary to permit the furnace to stabilize at a given set of conditions prior to sample preparation in order to obtain satisfactory reproducibility. Some measure of the reproducibility of the films can be obtained from **Figure 3-5** by noting the changes in conductivity from a series of twelve samples prepared in a single run consecutively. **Figure 3-6** shows the change in transmission and haze for the same sample.

Figure 3-4. Picture of the APCVD furnace showing how glass substrates are moved under the injection heads.

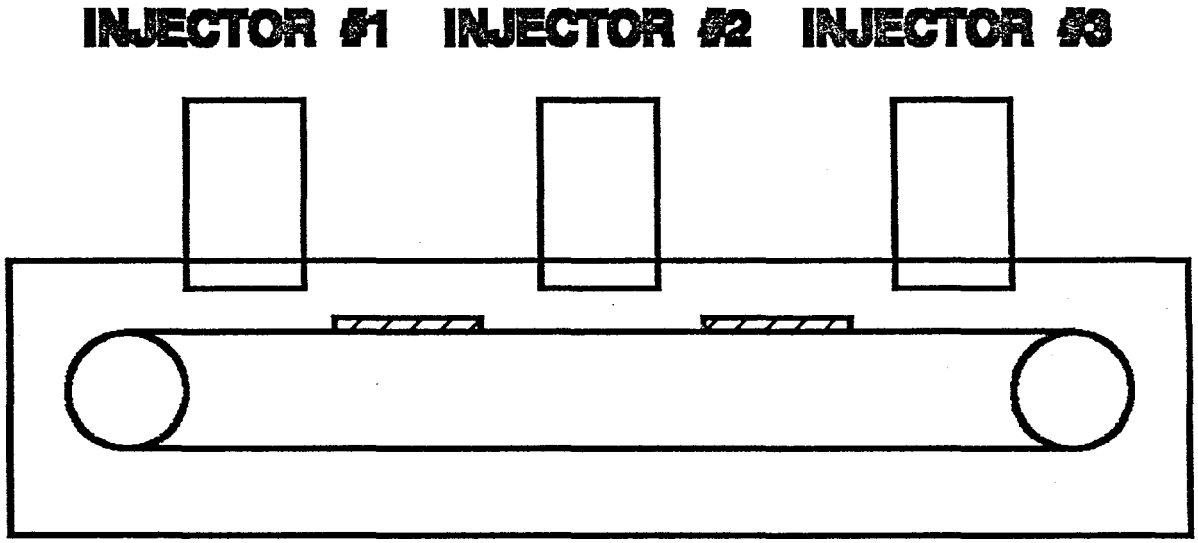

Figure 3-5. Variation in resistance as twelve 6 inch x 12 inch substrates were coated with zinc oxide films. The line above each substrate number gives the range of resistance values.

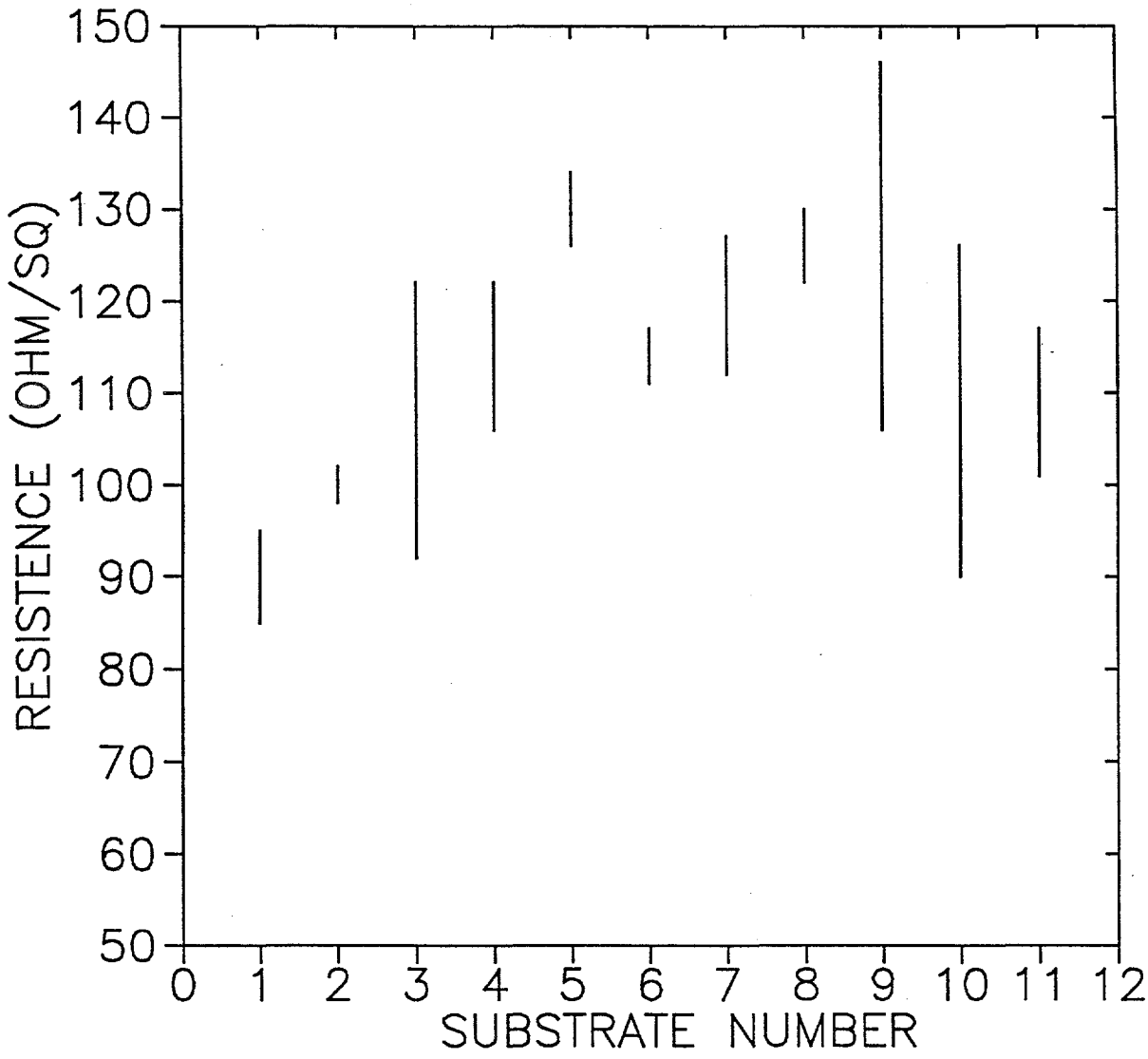

Figure 3-6. Variation in transmission and haze as twelve 6 inch x 12 inch substrates were covered with zinc oxide.

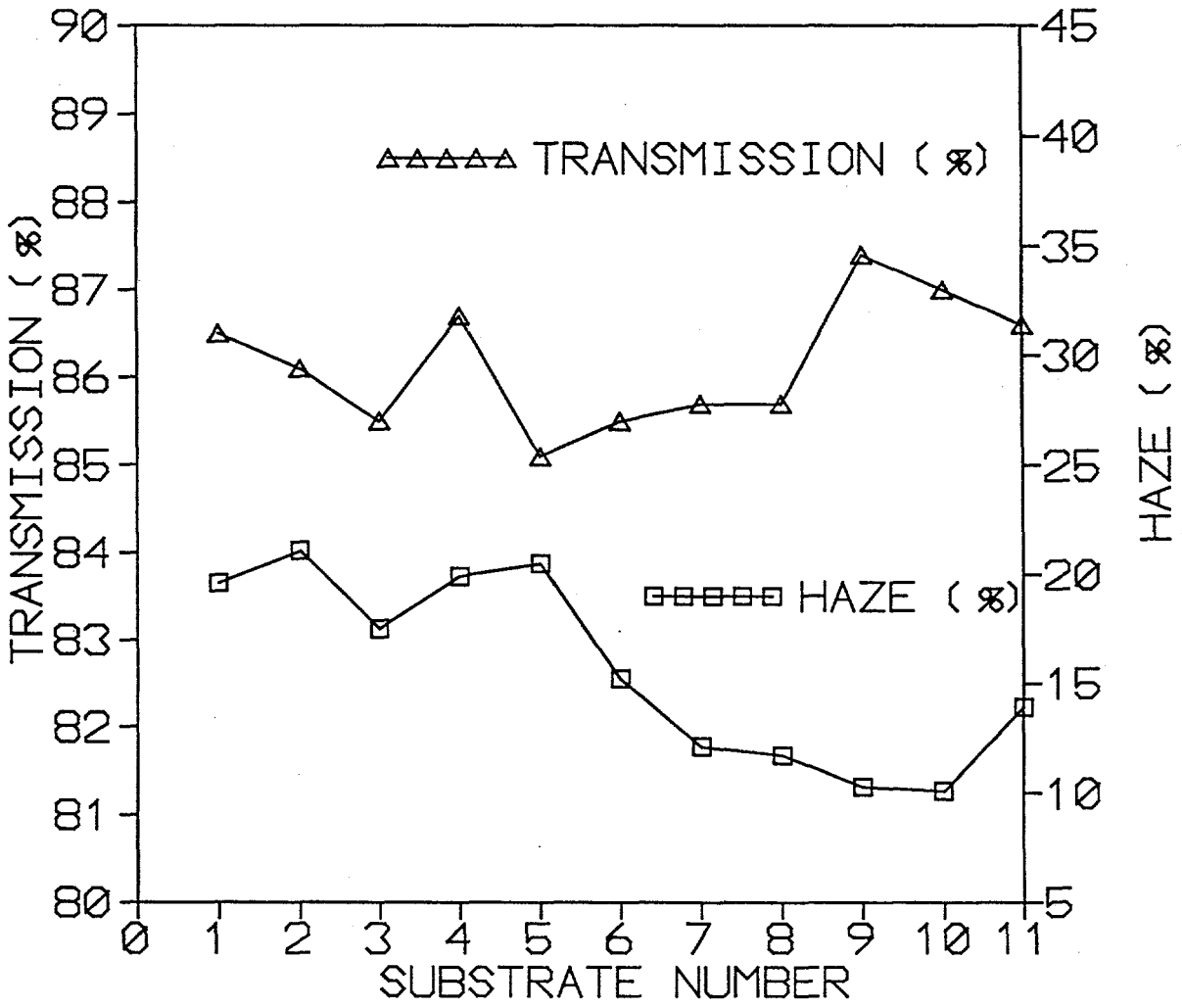

Table 3-2 gives a list of the properties of selected APCVD ZnO films. For comparison, typical tin oxide and LPCVD ZnO film properties are included. **Figure 3-7** shows the spectra of a typical specular sample of ZnO and **Figure 3-8** shows the spectra of a textured sample. Zinc oxide samples were characterized by Dektak IIA Surface Probe Measuring System, Sloan Technology). The optical haze and transmission value were obtained using a Gardner (Silver Springs, Maryland) Hazegard hazemeter which yield an average value over the visible spectrum.

Table 3-2. Properties of a Variety of ZnO and SnO_2 Films.

Film Type	APCVD - ZnO	APCVD - ZnO	LPCVD-ZnO	LPCVD-ZnO	Sputtered ZnO	APCVD-SnO_2
Thickness (Å)	7000	6000	8500	15000	800	9000
Resistance (Ohm/Sq.)	20-40	60-90	12-15	5-6	320	15-25
Transmission (%)	85.5	82.6	87.0	82.0	88-92	78-82
Haze (%)	21	23	2	12	0-1	20-30
Dopant	HF	C_3F_6	B_2H_6	B_2H_6	Al	HF

Initially, the samples were non-uniform and it was difficult to optimize depositions when the films contained materials with a wide range of optical and electrical properties. The major improvements in uniformity were accomplished by altering the position of the head to prevent turbulent flow. Uniformity also appeared to improve by switching from hydrogen fluoride (0.5% HF in nitrogen) to hexaflouroproylene (C_3F_6 HFP). The decomposition of HFP produces fluoride doping the oxide. As indicated in **Figure 3-9**, at high HFP flows, no further improvement in conductivity is obtained. This suggests that the kinetics of decomposition of the HFP limits the availability of fluorine. Studies with HF indicate a clear maximum conductivity established by the incorporated F.

Although pressure is not a variable in the APCVD system, the exhaust rate which is inversely related to the reagent residence time must be optimized. **Figure 3-10** shows the effect of adjusting the exhaust rate. Not surprisingly, the film thickness decreases as the exhaust rate increases and the residence time decreases. These results can be interpreted to mean that the longer time reagents spend in the furnace the greater is the chance that they will react and deposit. Surprisingly, better conductivity is obtained at higher exhaust rate, despite the lower film thickness.

Figure 3-11 shows that the deposition rate is related to the DEZ flow rate. The reaction is run with a very large excess of ethanol (typically 20 to 40 fold excess).

Figure 3-7. Visible spectra of a specular (haze 3%) zinc oxide film scanned in a high index fluid (diiodomethane).

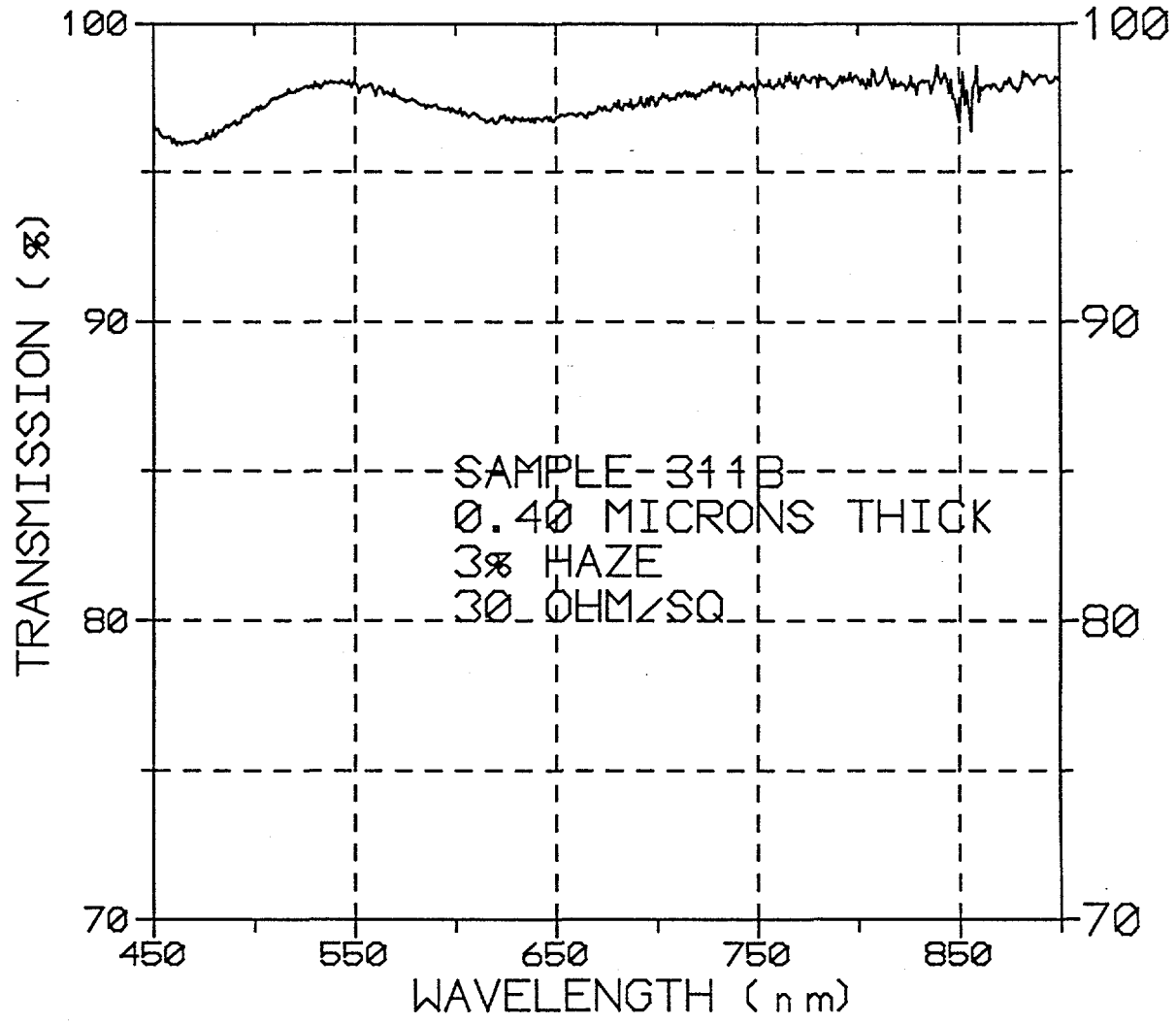

Figure 3-8. Visible spectra of a textured (haze 19%) zinc oxide film scanned in a high index fluid (diiodomethane).

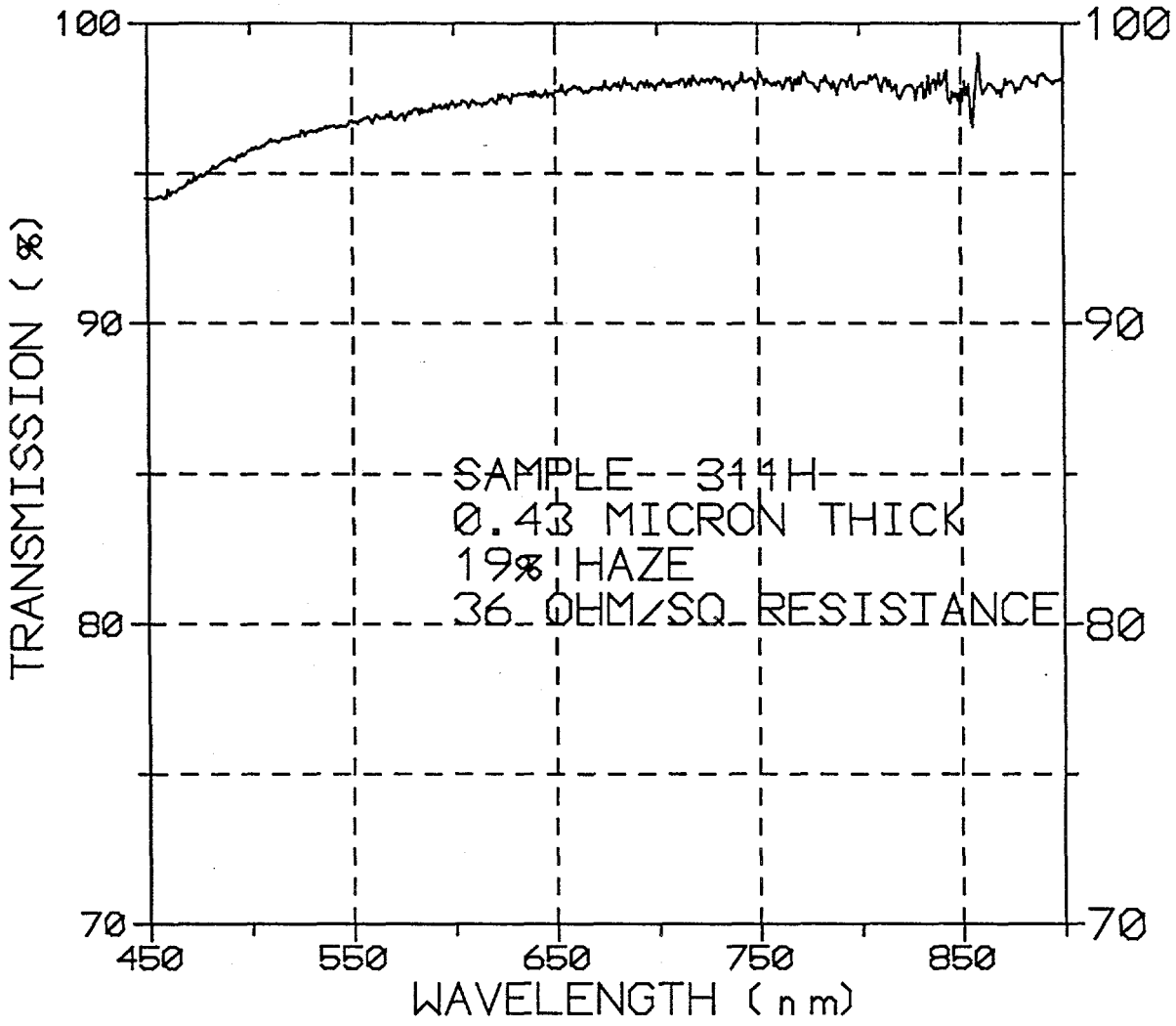

Figure 3-9. Change in resistance of zinc oxide films as a function of dopant (hexafluoropropylene) flow rate. Films were APCVD films prepared at 525°C. The films are all 0.5 - 0.6 microns in thickness.

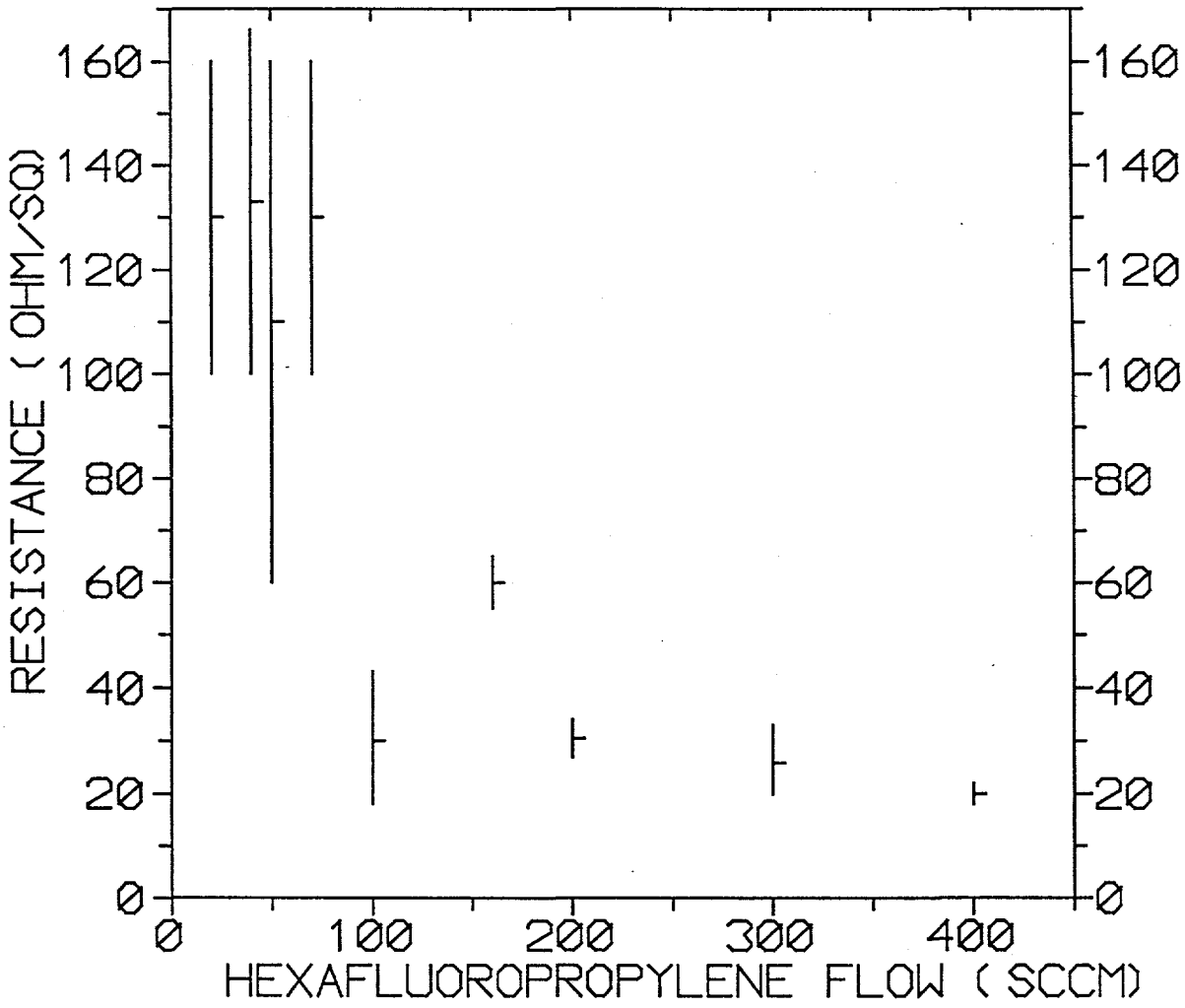

Figure 3-10. Change in APCVD zinc oxide film thickness and resistance as the exhaust rate from the furnace is increased.

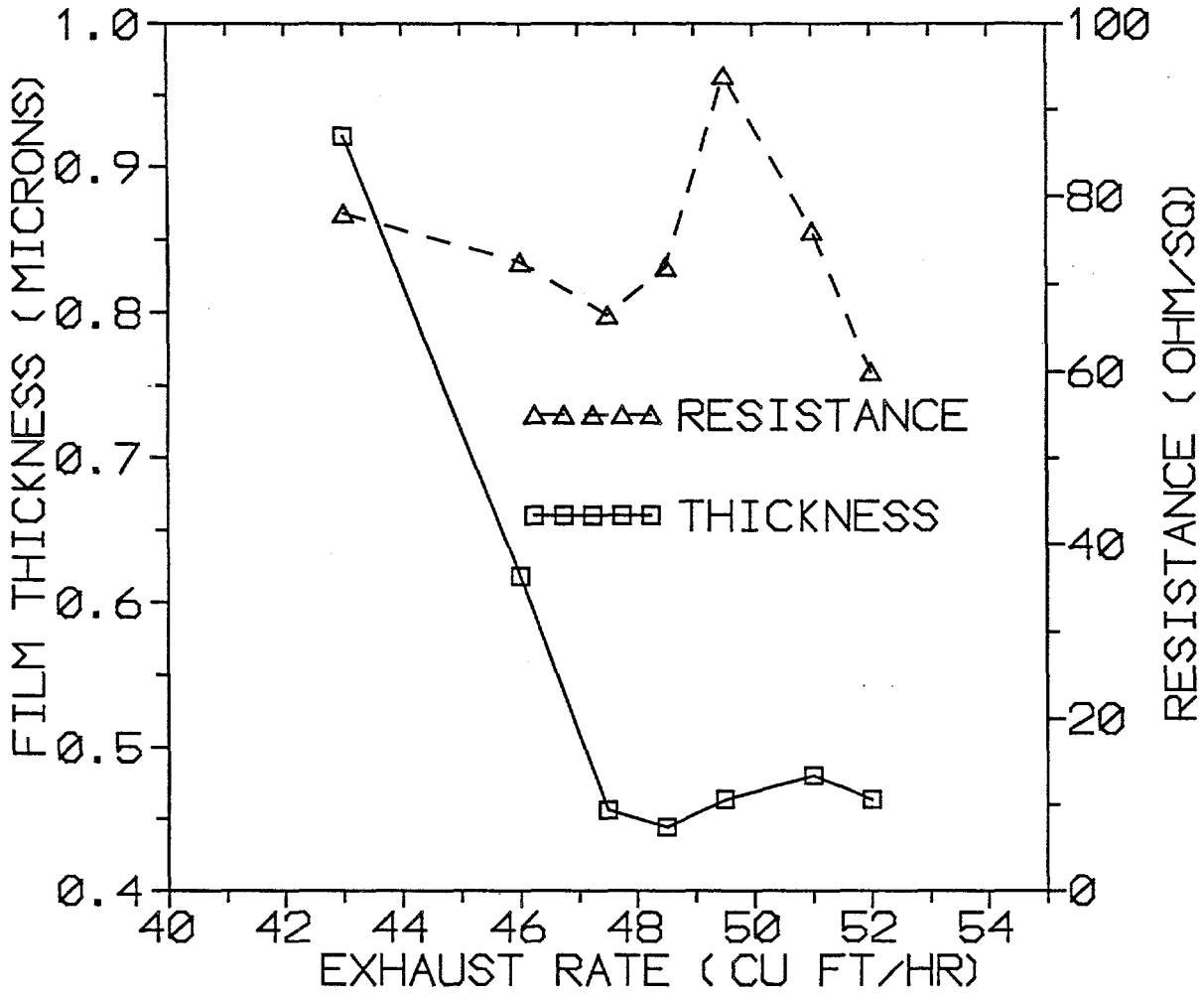

Figure 3-11. Affect of the flow of diethylzinc at 550°C and 575°C on the thickness of APCVD zinc oxide films.

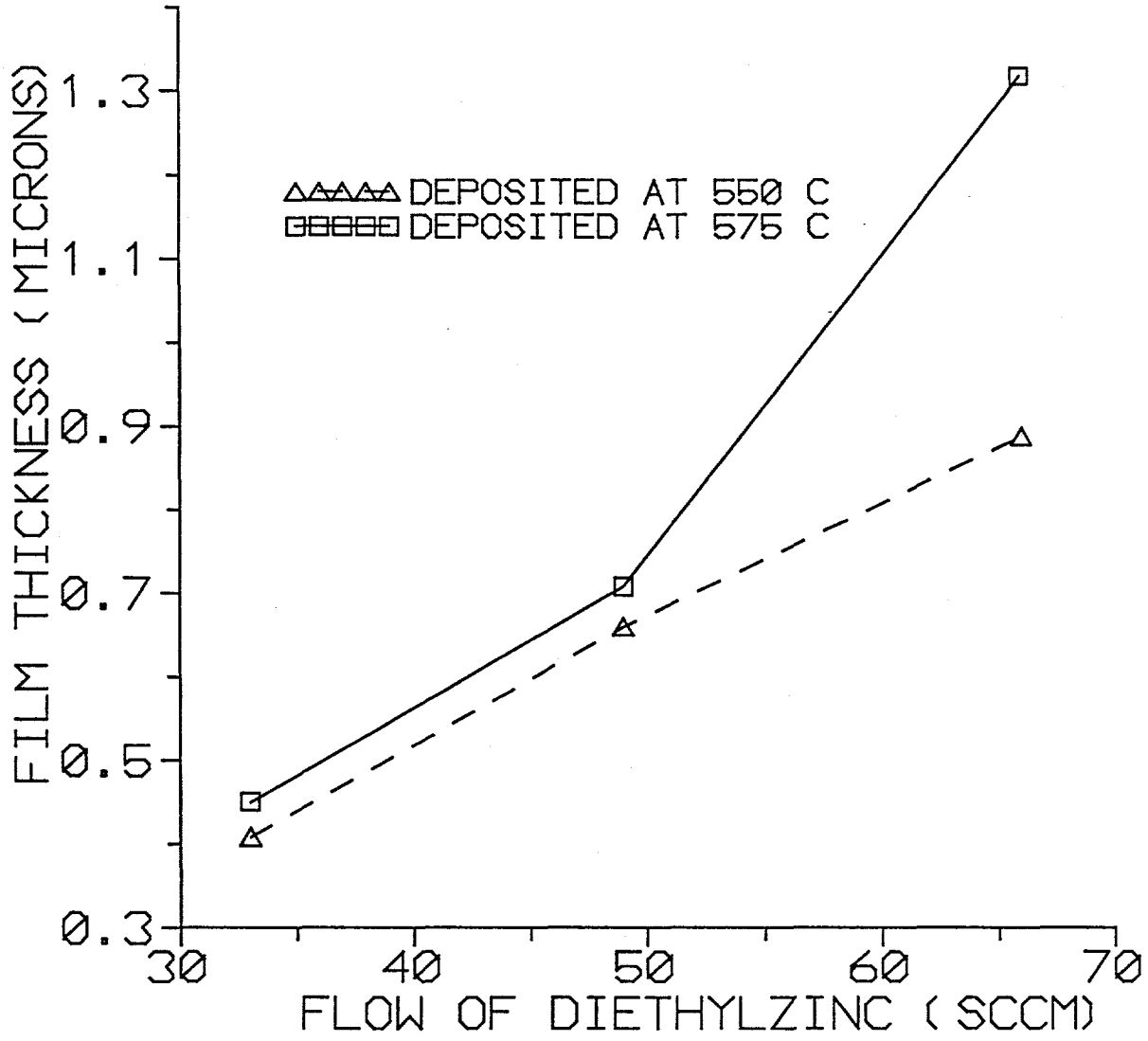

Interesting insights into the ZnO film structure have come from scanning electron micrographs (SEM) such as those shown in **Figure 3-12**. Zinc oxide prepared by APCVD appears to be made up of a large number of spheres that are 0.1 - 0.2 μm in diameter. Large "dust" particles are also visible. In contrast, the LPCVD ZnO is made up of highly crystalline material structure with many pores and crystallites 0.5 - 1 μm across that provide a very large surface area. It is clear that APCVD ZnO is structurally different material from the highly crystalline LPCVD material.

3.4 Back Contact Structures and Material

We have postponed further work on reactive dc sputtering of ZnO films in favor of rf sputtering from an oxide source.

3.5 Solar Cells on ZnO

As the properties of the ZnO films, in terms of sheet resistance, haze and optical transmission, become reproducible, several such films were selected for test solar cell fabrication. The properties of the ZnO films are given in **Table 3-3**.

Table 3-3. Properties of ZnO Films Used to Make a-Si Solar Cells.

Sample #	Thickness (μm)	Conductivity (1/Ohm-cm)	Transmission (%)	Haze (%)
91-295-I	0.911	157 - 177	82.7	34.0
91-295-J	1.230	185 - 194	81.1	53.4
91-295-G	0.780	130 - 160	85.4	21.3
91-295-H	0.946	163 - 192	80.0	44.5

A control single junction solar cell structure containing a 7000Å i-layer was grown simultaneously on samples of all ZnO films and on our standard SnO_2 substrates. Solar cells were completed using ZnO/Ag back contacts.

Measurement of such control cells involves probing them with spring loaded contact electrodes. For the cells on ZnO, we noted extreme sensitivity to such probes, with increased reverse currents, in most cases, and sometimes shorting of cells. This is generally not the case for cells on SnO_2. The latter are quite robust showing no measurable change in electrical parameters with

Figure 3-12. SEM pictures showing the difference between the highly crystalline LPCVD zinc oxide films (a) and the APCVD films made of small spheres (b).

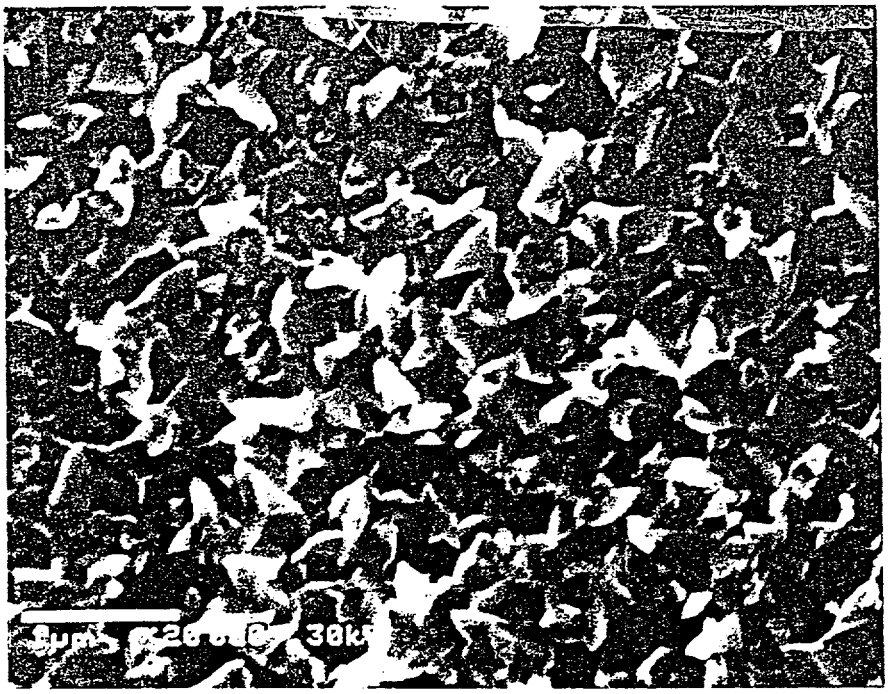

(a)

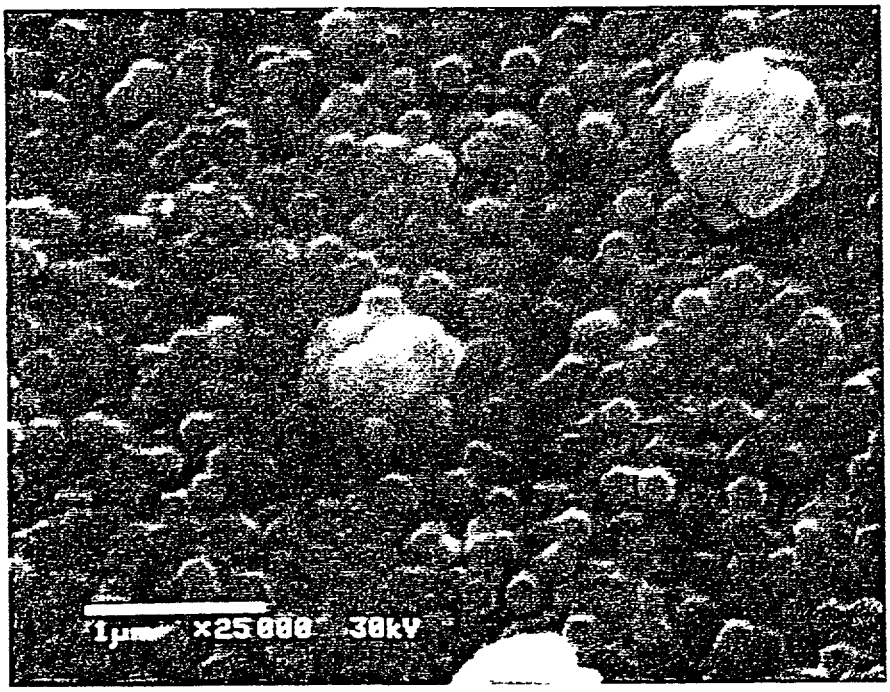

(b)

contact pressure. The sensitivity of the cells on ZnO may be due to a combination of the inherent softness of ZnO and the "powder-like" structure of the surface texture of the APCVD films.

For the above reason, it was quite difficult to obtain reproducible measurements of the solar cell efficiencies and spectral responses. Measurements obtained for some cells on ZnO and the controls on SnO_2 are summarized in **Table 3-4** and **Figures 3-13** and **3-14.** It should be noted that although the efficiency of the controls and the best cells on ZnO are about equal, some features of the quantum efficiency (QE) data for ZnO show important differences indicating potential improvement over tin oxide. The high blue response, peak QE of almost 90%, and QE of 60% at 700 nanometers (obtained at -1V to eliminate collection effects), are noteworthy as such high values are not obtained with SnO_2 substrates. One problem noted has been generally lower V_{oc} with ZnO substrates.

Attempts will be made to improve the surface morphology and density of ZnO films so that improved devices can be prepared.

Table 3-4. Solar Cell Parameters for Cells on ZnO.

Cell/Substrate	J_{sc} (mA/cm^2)	V_{oc} (mV)	FF	η %	QE_{peak}	QE_{700nm}
MC 1301-2 / SnO_2 (Control)	16.3	849	.632	8.8	84%	54%
MC 1301-2 / ZnO (295I)	17.0	820	.608	8.5	89%	60%

Figure 3-13. Illuminated I/V curve for single junction control cell made on SnO_2; an identical device fabricated on ZnO yielded a far lower V_{oc} (see **Figure 3-14**).

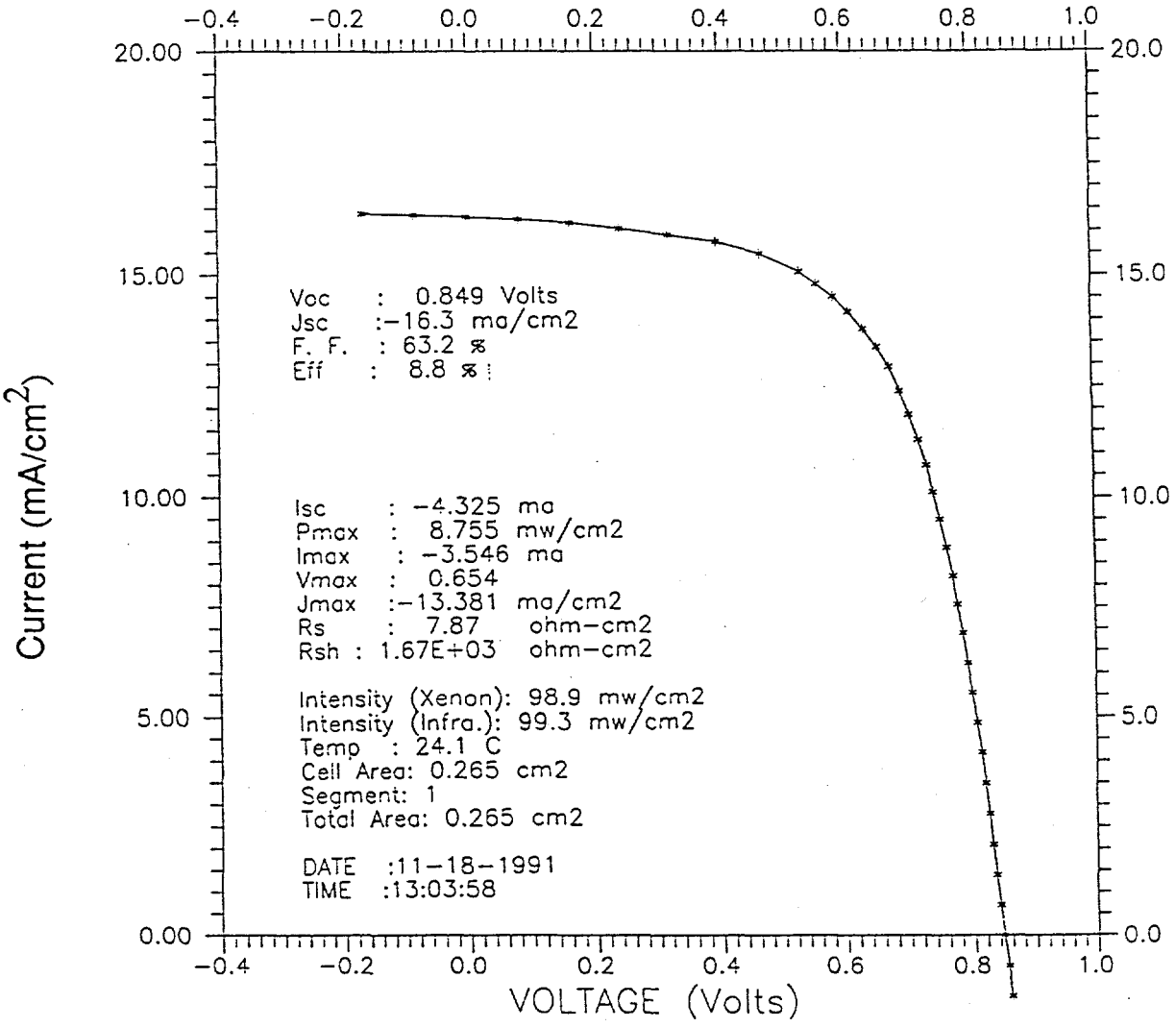

Figure 3-14. Illuminated I/V curve for single junction cell deposited on APCVD ZnO. The control cell I-V is shown in **Figure 3-13.** The currents determined from quantum efficiency measurements (**Table 3-4**) are more accurate and confirm the higher ZnO optical transmission.

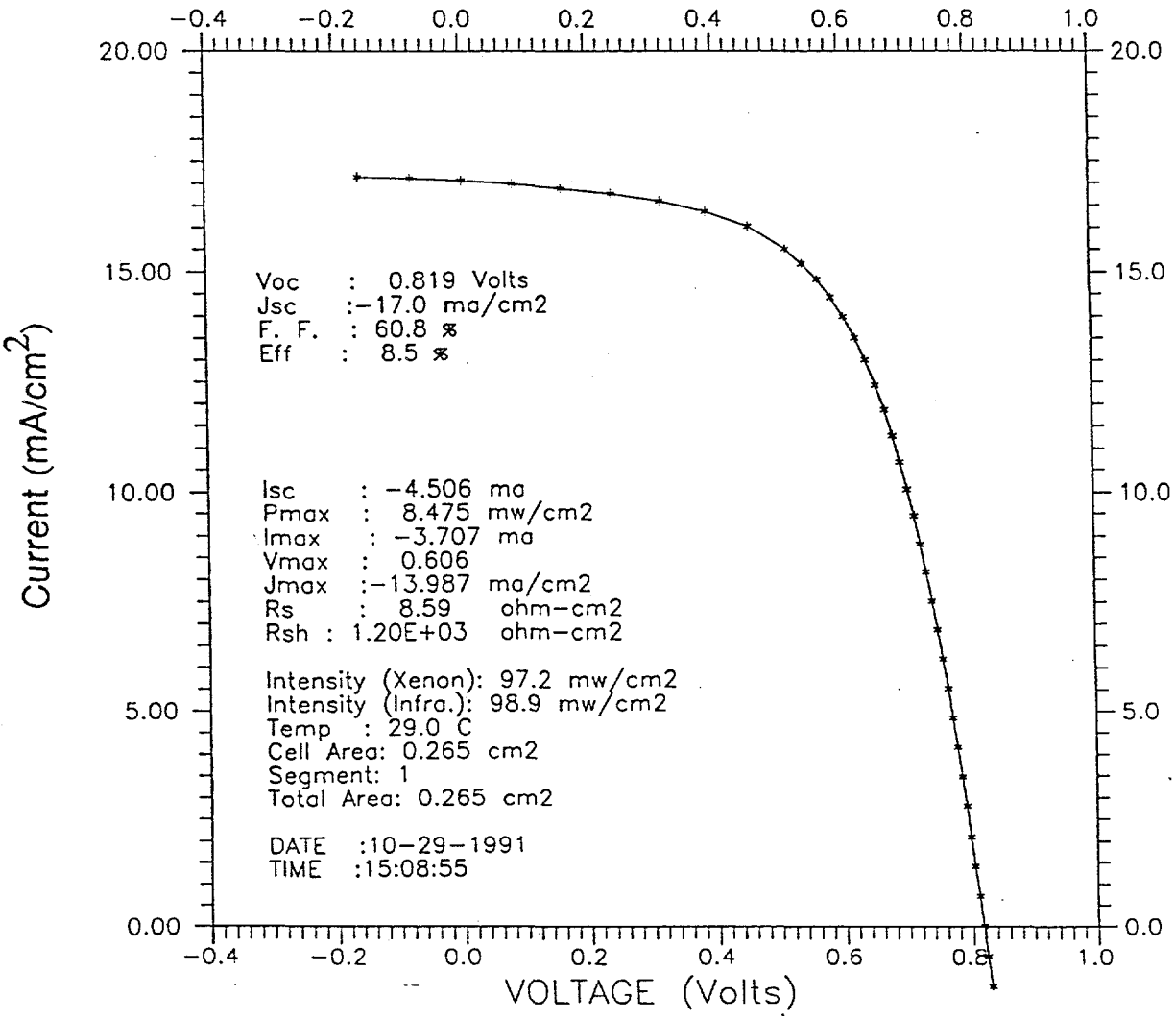

4.0 TASK III: MODULE RESEARCH

4.1 Introduction

The principal second year goal of this task is the development and demonstration of a multijunction module which exhibits 10.5% efficiency after 600 hours degradation at 50°C under AM1.5 global illumination. Subordinate objectives include the evaluation of the electrical and optical losses of state-of-the-art modules, characterization and elimination of defects, and the continued optimization of the vertical interconnect.

Most of our effort over the last six months has been directed toward improvements in what we have previously termed "ground level" problems associated with making modules. These issues include the discovery of the major role which shunts play in both the initial and stabilized performance of the modules, as well as the reproducibility of the rear contact.

During this reporting period, the important influence of the underlying tin oxide and the role of defects in that film, giving rise to shunt-like defects in devices, has been realized. Improvements in the tin oxide have reduced, but not eliminated, the occurrence of these defects. Towards the end of this reporting period relatively defect-free tin oxide became available, but because of the long lead-time for module fabrication testing and degradation, little of that improved tin oxide has been used in this study.

Unless noted by exception, all the modules described here contain a-Si:H p-i-n/a-Si:H p-i-n/a-SiGe p-i-n triple-junction devices, with bandgaps of 1.7 eV, 1.7 eV and 1.45 eV, respectively. All modules are > 900 cm^2 in area. Rear contacts are comprised of sputtered ZnO overcoated with silver except as noted. 5:1 dilution with hydrogen is used for a-SiGe devices. a-SiC devices have not been sufficiently developed to warrant their inclusion in modules. It should be noted that, in addition to yielding an expected higher open circuit voltage, a-SiC:H front junctions would be considerably thicker than their a-Si:H counterparts. Calculations indicate that a 500Å front i-layer would be replaced with a ~1500Å 1.9 eV a-SiC:H. We expect the use of such a thicker layer to reduce the vulnerability of the device to defects, given the better surface coverage of such a film. Likewise, the modules reported here do not yet incorporate ZnO as the front contact. Further refinement to improve uniformity and reproducibility are necessary before it can be used in modules. Furthermore, the initial devices made on ZnO indicate that problems may be expected when fabricating devices as the initial devices have an average 0.1 V lower V_{oc}.

4.2 Impact of Shunts on Initial Device and Module Performance

We have determined that the large flakes of tin oxide debris on the edge of many modules are likely to be responsible for a large part of the initial variation in module performance. **Figures 4-1** and **4-2** illustrate the impact which shunts can have on the initial performance of small area (≈ 0.26 cm^2) triple-stack cells. In these figures, the size of the shunt is characterized by the device leakage current at -2 volts reverse bias. The more severe the shunt, the greater is the leakage current. It can be seen that the V_{oc} of the cell is not much affected until the leakage current increases to about 1 mA (4×10^{-3} A/cm^2). On the other hand, the fill factor begins to be seriously affected by the time the leakage current reaches 0.1 mA. This data indicates that the initial performance of our triple-stack modules, which have an active segment area of 35.19 cm^2, will begin to be affected when the leakage current reaches about 10 to 15 mA. Since "good" small area cells have a leakage current of about 2 μA, it should be possible, under ideal conditions, to make modules having segments with leakage currents of about 0.25 mA. Indeed, we have made modules in which 80% of the segments have leakage currents of ≤ 1 mA. **Figure 4-3** shows the dramatic impact which shunts can have on the open-circuit voltage of triple-stack modules.

Another qualitative indication of the progress which has been made in reducing module-to-module variations in initial performance since we began "re-scribing" the modules as can be seen in **Figures 4-4** and **4-5**. (The re-scribe process will be discussed in the next section of the report.) **Figure 4-4** shows the V_{oc} of a large group of modules made before re-scribing became part of the module fabrication process. After adopting the re-scribe procedure, the range of this variation was greatly reduced, as shown in **Figure 4-5**. Part of the increase in V_{oc} which is apparent in **Figure 4-5** arises from the use of an improved SiGe:H alloy in the i_3 layer of the triple-junction module.

4.3 Origin of Shunts and Ways to Reduce Their Impact

As previously reported, the principal sources of shunts are tin oxide debris, a-Si debris, mishandling of the module, and laser-induced shunting along the metal scribe.

Although there are many types of SnO_2 debris (see Section 2.1), the large flakes (0.005" across) of debris which are spalled from parts inside the CVD furnace during the SnO_2 deposition are the only kind of tin oxide debris which seems to correlate with shunt problems which affect the initial performance of the module. Although we have investigated a number of ways of removing this debris from the superstrate, no satisfactory method has been found. Improved cleaning

Figure 4-1. Effect of leakage current on V_{oc} in a small-area triple-junction cell.

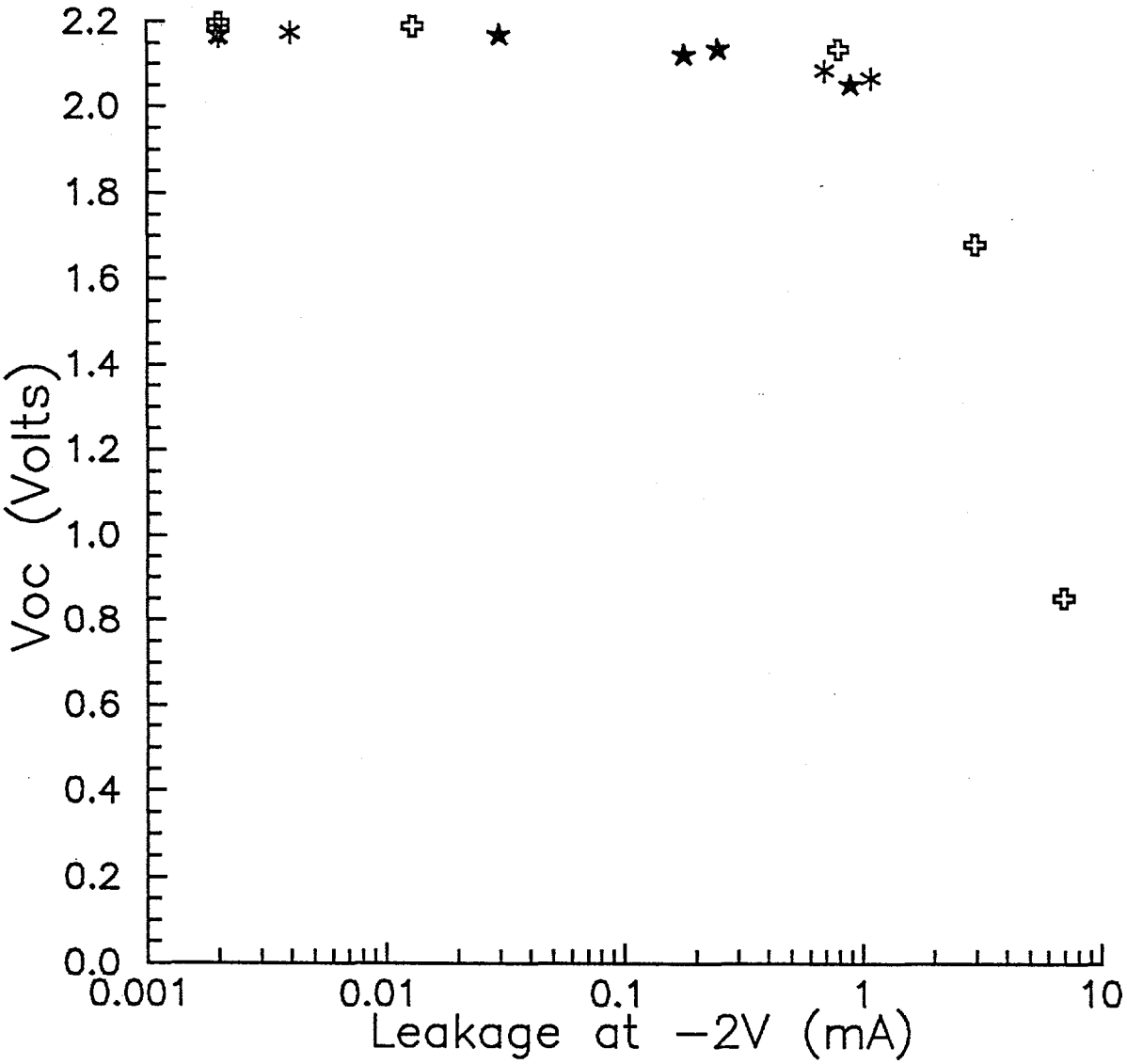

Figure 4-2. Effect of leakage current on FF in a small-area triple-junction cell.

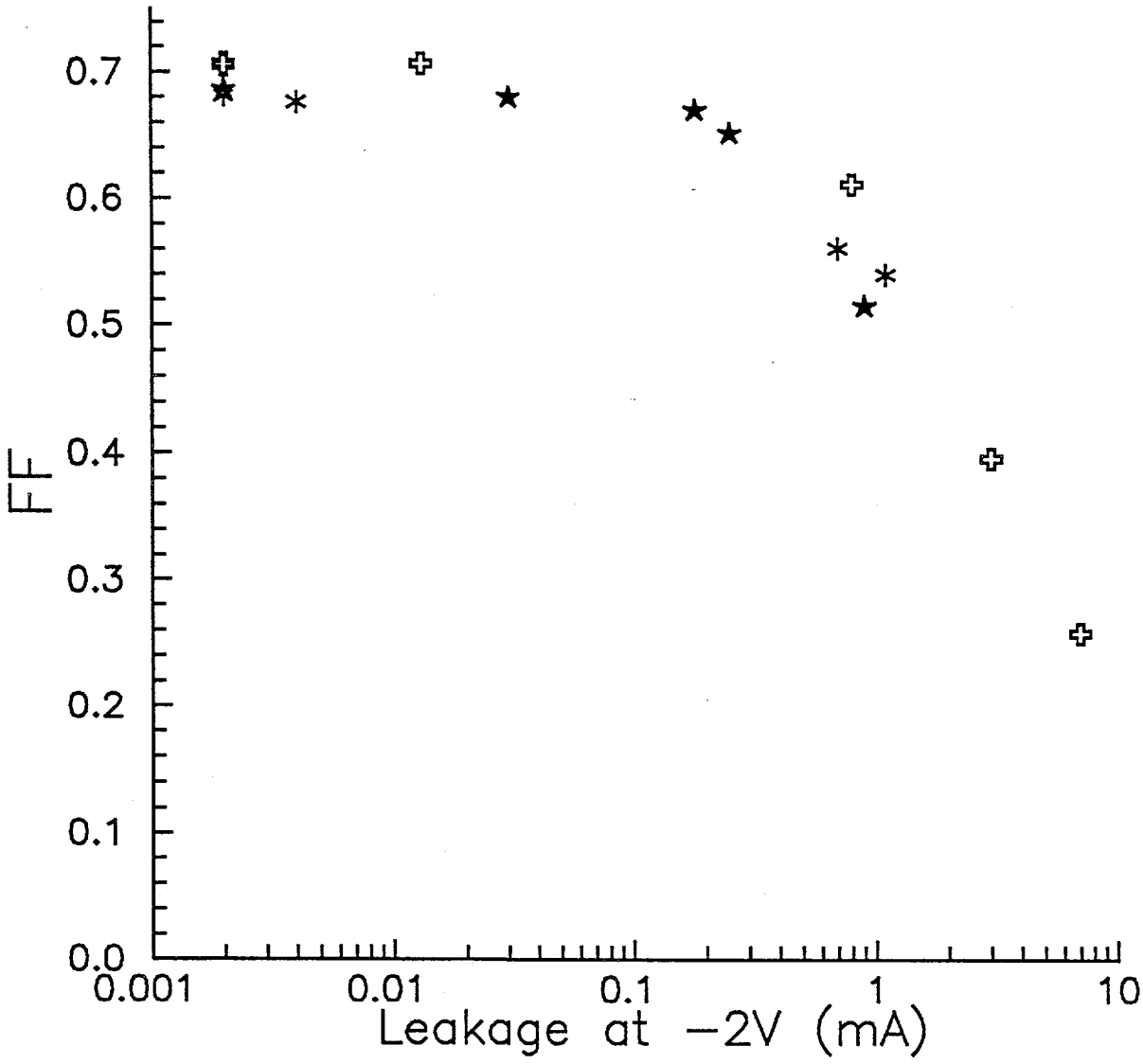

Figure 4-3. Effect of leakage current on V_{oc} in 936.3 cm^2 triple-junction modules.

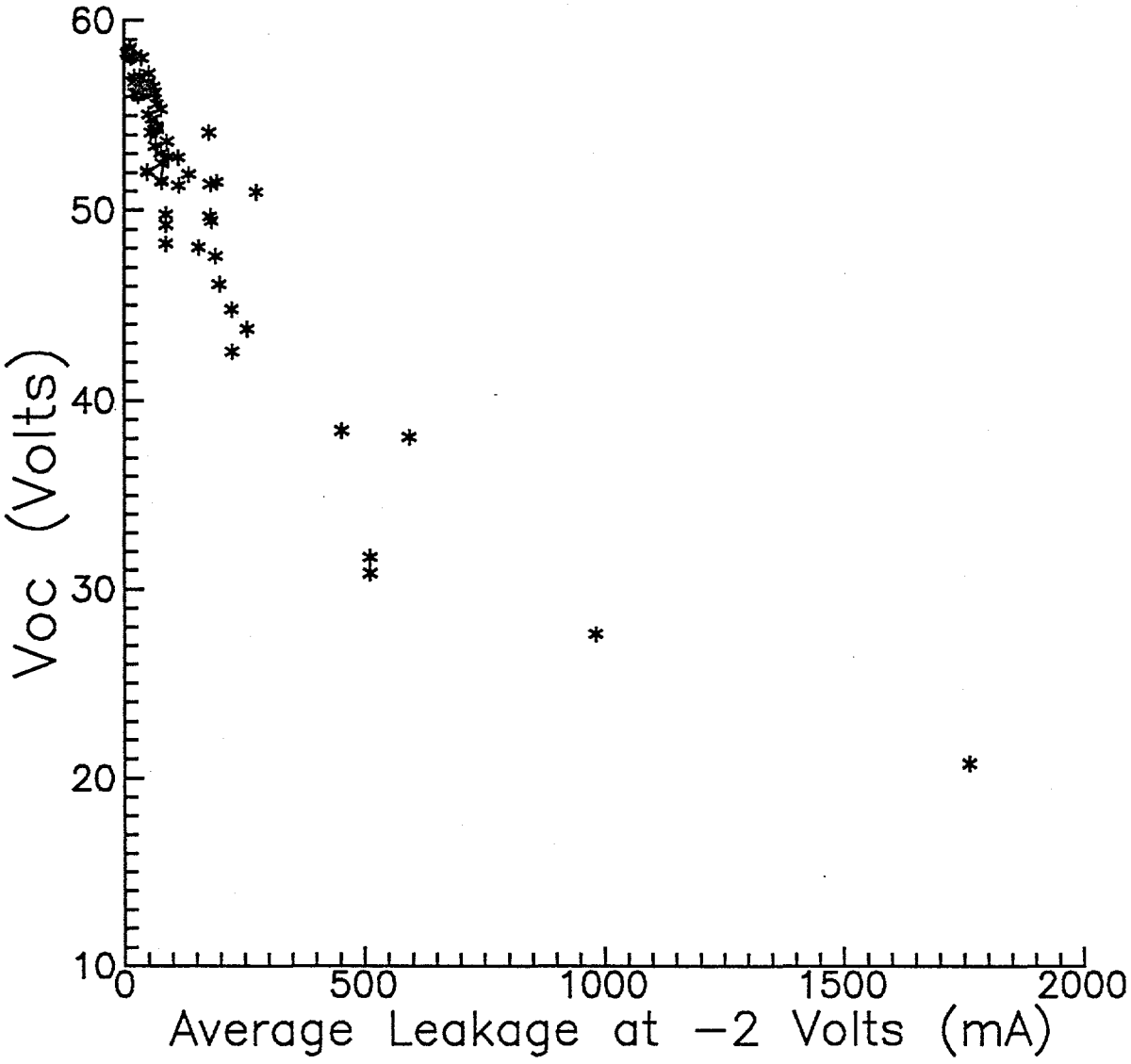

Figure 4-4. Variation in V_{oc} for triple-stack modules without re-scribes.

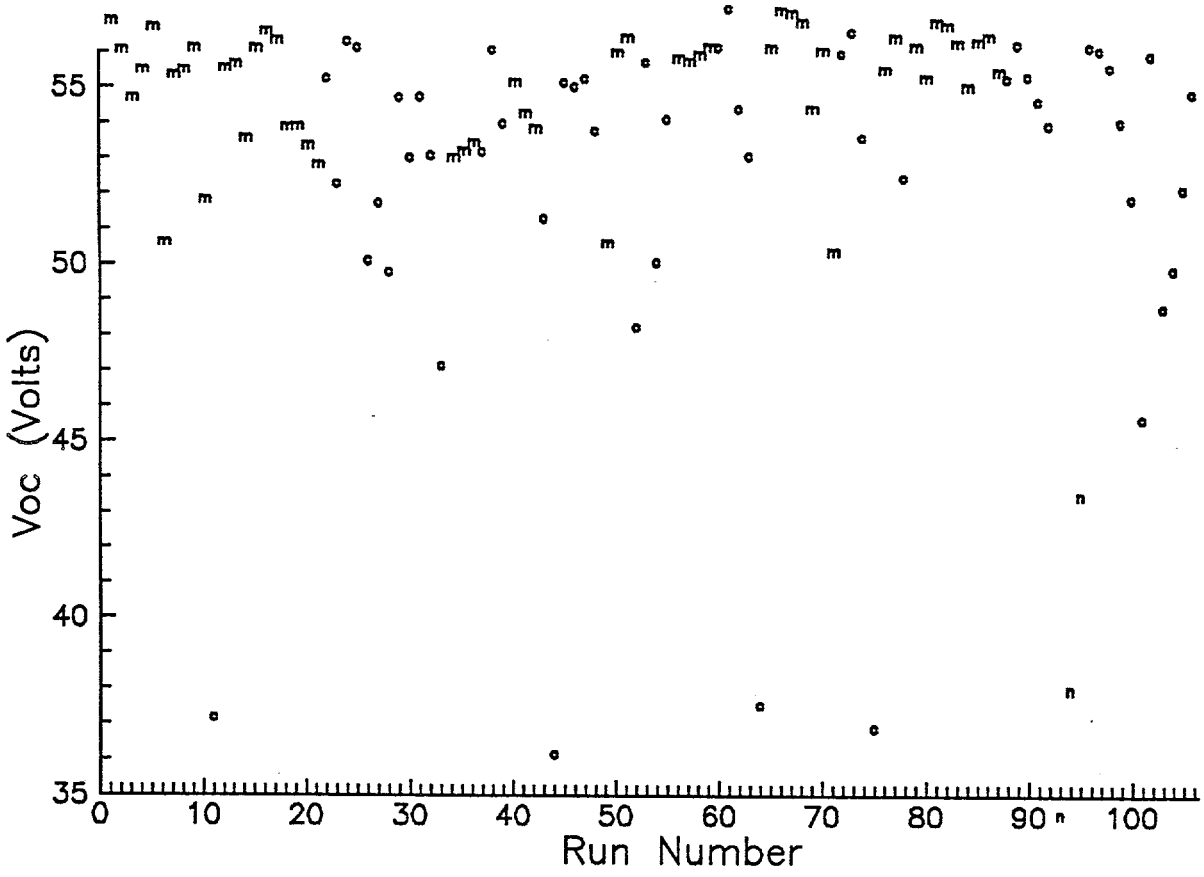

Figure 4-5. Variation in V_{oc} for triple-stack modules with re-scribes.

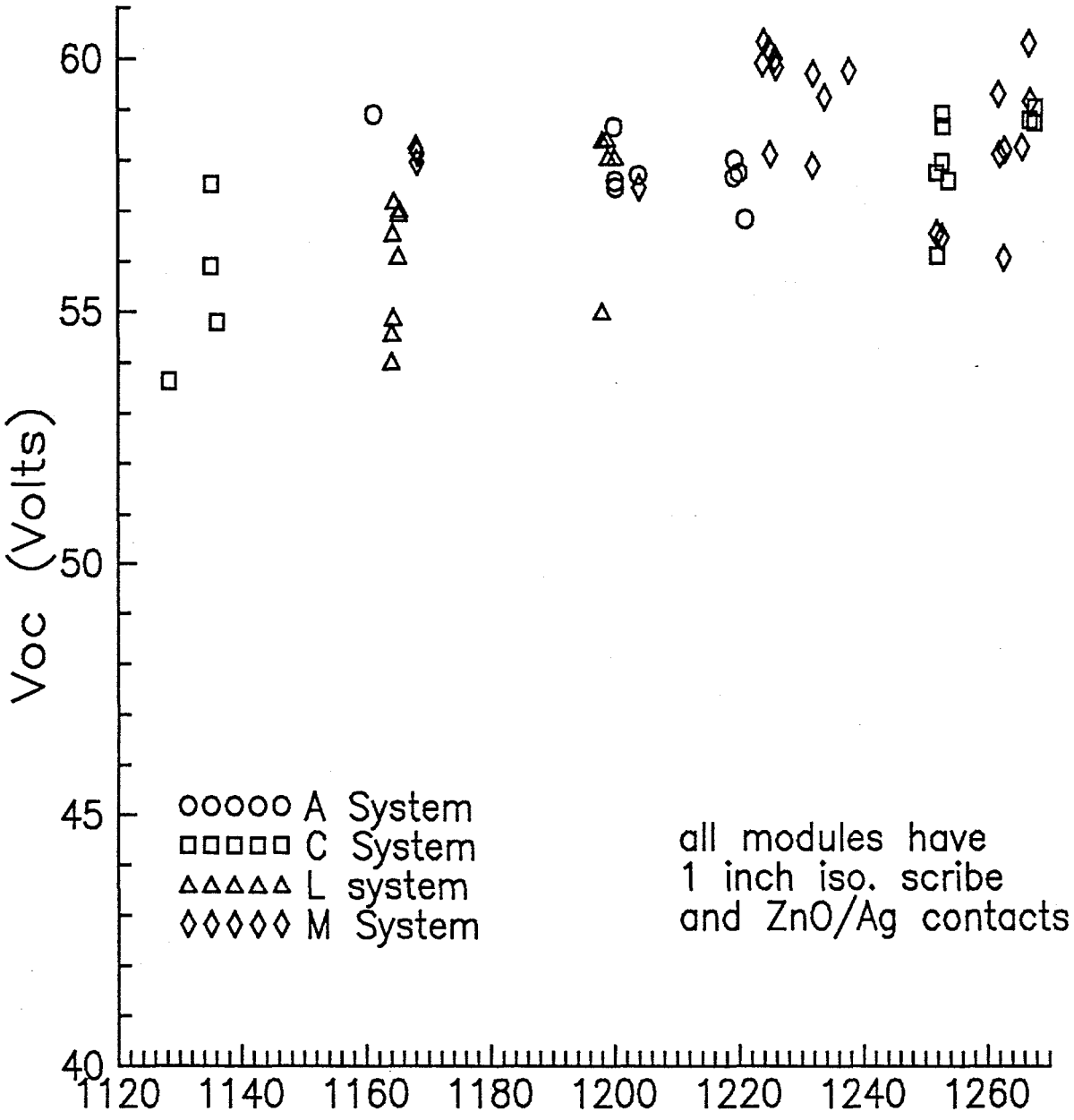

procedures have reduced - but not eliminated - this problem. As a stopgap measure, we have found that re-scribing the modules to keep the active area of the module far from the glass edge, is sufficient to greatly reduce the number of segments having high leakage. It appears that this process works because the large tin oxide debris is predominantly found near the edges of the module. Although we are relatively certain that these shunts are the ones which affect the initial module performance, we are not convinced that the elimination of these defects is sufficient to avoid the anomalous degradation effect which has been ascribed to a shunt problem.

The role of a-Si:H debris in affecting the shunts seems to be quite variable. Even the formation of the debris seems to be quite system dependent and may be related to non-recognized differences between deposition system parameters or a-Si:H recipes. In general, the multichamber deposition system is less susceptible to this problem. However, in the load-locked single-chamber deposition systems, there are large differences in the frequency of this debris formation. There is often no apparent effect of the a-Si:H debris on the module performance.

However, if the a-Si:H-related debris is dislodged, e.g. by mishandling, before the rear contact is deposited, a direct shunt path can be formed between the front tin oxide and the rear contact, and the module performance will be reduced.

A number of experiments have indicated that the total a-Si:H thickness plays a role in the size of the shunt current. **Table 4-1** shows the results of an experiment on some tandem a-Si:H/a-Si:H modules in which the thickness of the i_2 layer was varied from 1000Å to 3000Å. Two 26-segment modules were made for each thickness and the number of segments having leakage

Table 4-1. Tandem i_2 Thickness Experiment Analysis of Leakage Current/Segment at -2V.

	# Seg > 100 mA	# Seg > 100 - 25 mA	# Seg > 25 - 10 mA	# Seg < 10 mA
Thickness:				
1000Å	49	3		
2000Å	21	18	8	
3000Å	7	11	13	21

currents of various sizes was tabulated. As the i_2 thickness was increased, the number of segments having a leakage current greater than 100 mA dropped dramatically and the number

of segments having a leakage current less than 10 mA increased dramatically. In other experiments on both tandem and triple-stack modules, the thickness of the n_2 layer (adjacent to the rear contact) was increased with similar results.

Although many kinds of shunt paths can be "burned out" or "cured" by forcing a large current through the shunt, some shunts appear to re-form after some time, even if the cell is left in the dark. Many other kinds of transient behavior and instability can be observed in the dark I-V behavior of a cell or an individual segment on a module. Whether any of this behavior is correlated with the anomalous shunt degradation has not been unequivocally determined.

4.4 Influence of Rear Contact Material(s) on Shunt

After some initial results which seemed to indicate that cells with Al rear contacts were more stable than cells with ZnO/Ag rear contacts, further experiments were not able to reproduce this promising result. In one experiment comparing six different rear contacts, Al, ITO/Al, ITO/Ag, ITO/Ni, ZnO, and ZnO/Ag, there is no convincing evidence that one metal offers any significant advantage over the others. **Figure 4-6** shows the efficiency vs. time for the six different rear contacts. Each point in **Figure 4-6** is actually the average of 9 cells which vary in area from 2 to 3 cm^2. The cell-to-cell variation in the size of the shunts for each metal seemed to indicate that the effect of the metal was secondary to the other shunt causes, such as the amount of tin oxide debris on the substrate.

In another experiment, a large number of triple-stack modules was made and metallized with either Al or ZnO/Ag. **Figure 4-7** shows the average leakage current per segment on each module. Again, there is substantial variation from one run to the next, but, if anything, Al appears to be more prone to shunts than ZnO/Ag.

4.5 Effect of Shunts on Stability

In addition to affecting the initial performance, shunts also affect the stability of the devices. **Figure 4-8** shows the deleterious effect which a shunt can have on the stability of a small area cell. Similarly, the stability of modules is often affected by the presence of shunts. **Figure 4-9** shows the stability of a group of modules which have been degraded outside at V_{oc}. For one module being degraded outside, the change in each cell parameter, plotted as a function of the

Figure 4-6. Stability of cells having various metals for the rear contact.

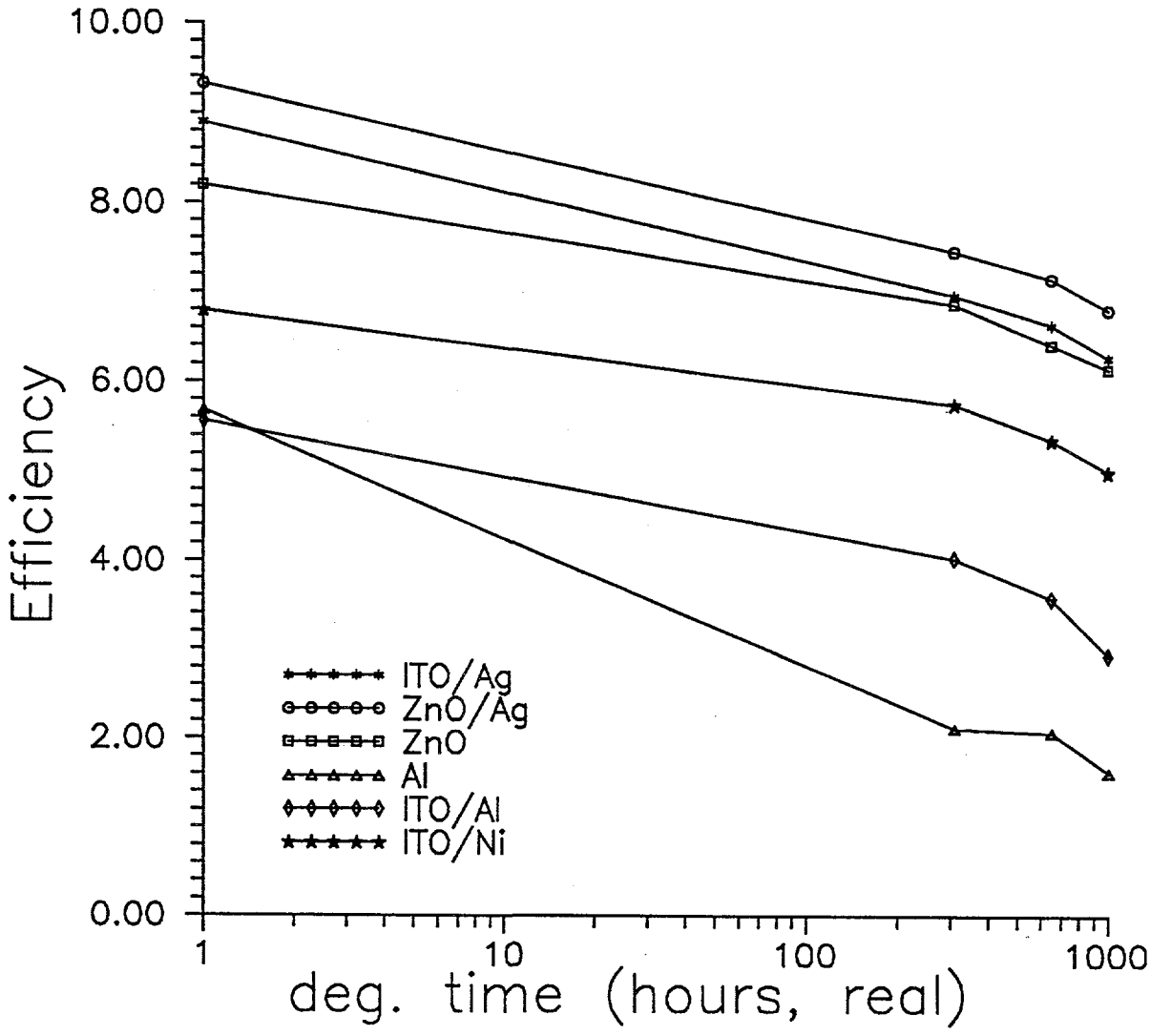

Figure 4-7. Average leakage current per segment for 789 cm^2 modules having either Al or ZnO/Ag rear contacts.

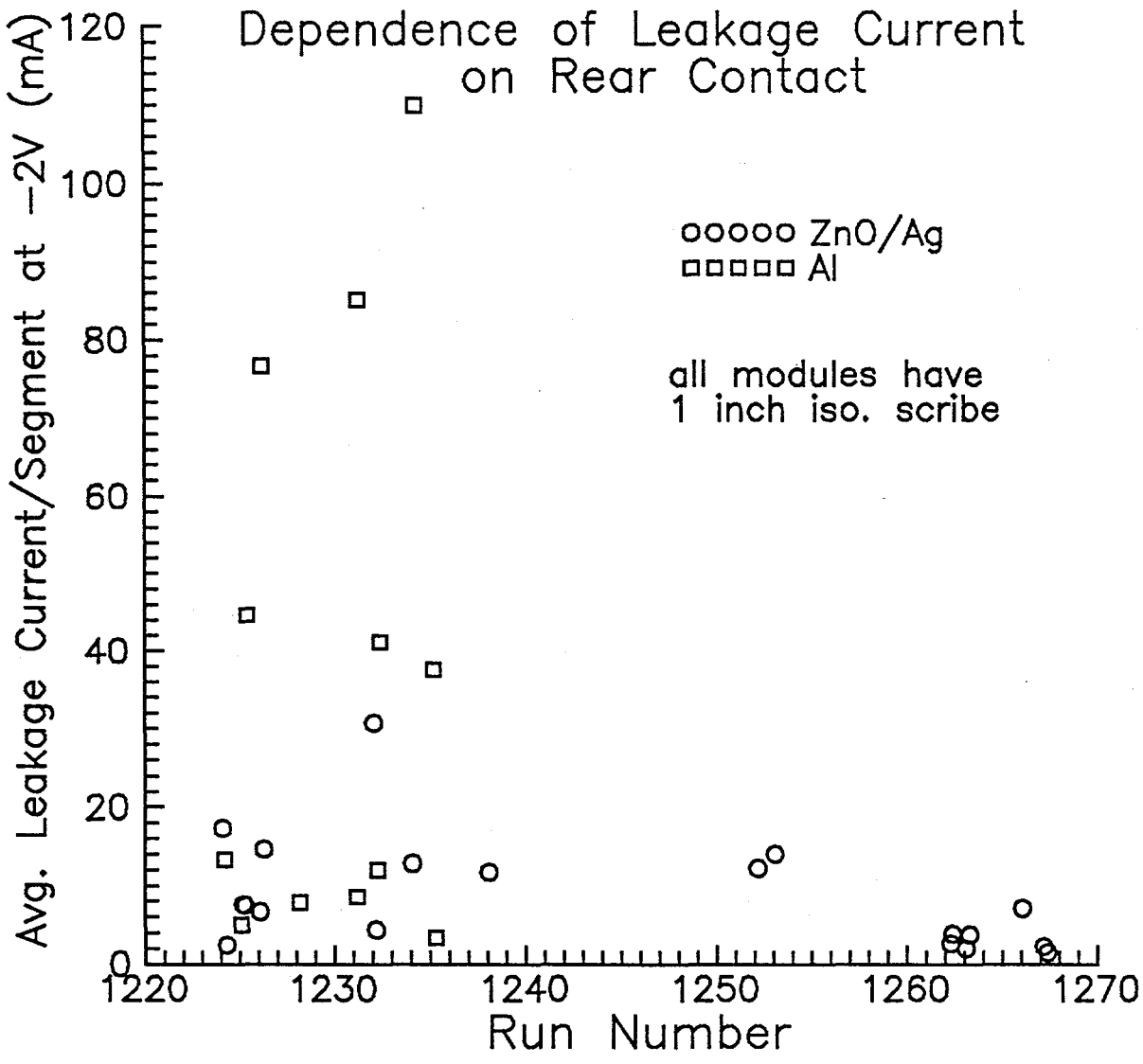

Figure 4-8. Effect of "shunt" vs. "no shunt" on the stability of a small-area triple-stack cell.

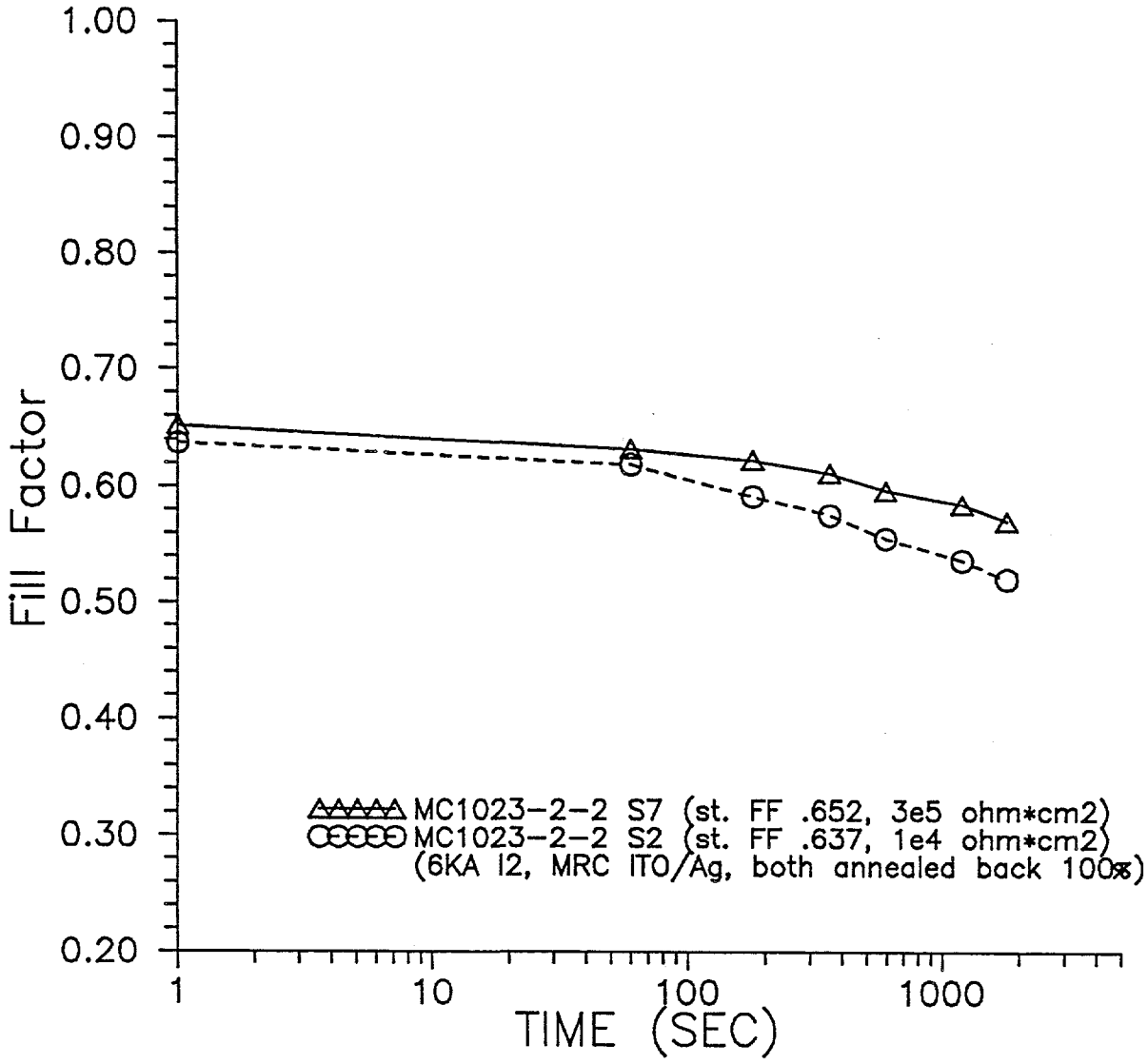

Figure 4-9. Outdoor stability measurements of triple-stack modules without re-scribes.

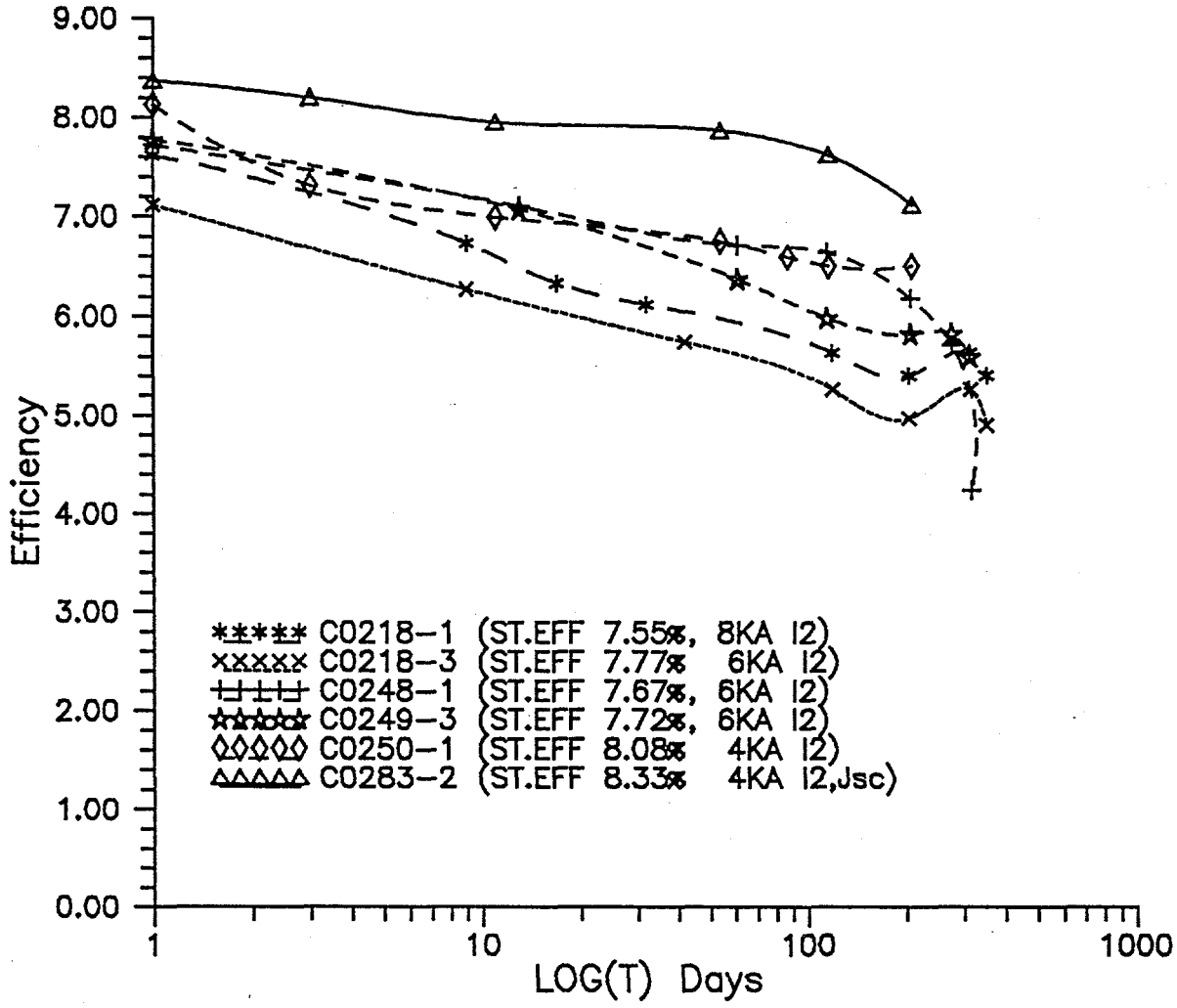

light-soak time is shown in **Figure 4-10**. Although most of the decrease is in the fill factor, V_{oc} also degrades about 7%, indicative of the development of a shunt resistance problem. Two other points related to **Figure 4-10** should be made: 1) the increase in I_{sc} after ≈100 days was caused by a change in the simulator calibration, and 2) evidence of the seasonal annealing which is often observed in a-Si:H is also seen.

When modules are re-scribed, resulting in much lower leakage currents per segment, not only is the variation in initial performance reduced, but the variation in the rate of degradation is also greatly reduced. **Figure 4-11** shows the aperture efficiency of four modules as a function of the length of simulated light exposure with the module held at V_{oc}. One very encouraging result which is evident in this figure (and which has now been seen on a total of 11 re-scribed modules) is that there is no sign of the rapid fall-off in module performance in the 600 to 1000 hour time-frame, as has been noted in modules with high leakage current.

4.6 Other Stability Results

4.6.1 Modules Degraded for 2000 hours at NREL

Table 4-2 gives the results of a degradation experiment performed on Solarex modules at NREL. Five triple-stack modules were light-soaked indoors at maximum power. The results indicate a stabilized aperture efficiency (600 hrs., AM1.5, 50°C) in excess of 7% on these modules. It should be noted that these modules, made early in the program in Phase I do not contain the rescribes used to limit leakage and, thus, represent a "worst case" scenario.

Table 4-2. Aperture Area Efficiency (in %) of Solarex Triple-Stack Modules Degraded at NREL.

Module	Initial	600 Hours	2000 Hours
MC0304-3	8.69	7.24	6.74
MC0304-2	8.95	7.31	6.70
MC0304-1	8.92	7.14	6.58
MC0310-1	8.59	7.04	6.71
MC0242-2	9.05	7.06	7.29

Note: The aperture areas were delineated incorrectly for the first four modules, causing the measured aperture efficiencies to be about 2.8% too low.

Figure 4-10. Change in cell parameters for a module degraded outdoors (without re-scribes). The legend gives the initial and final values of the cell parameters.

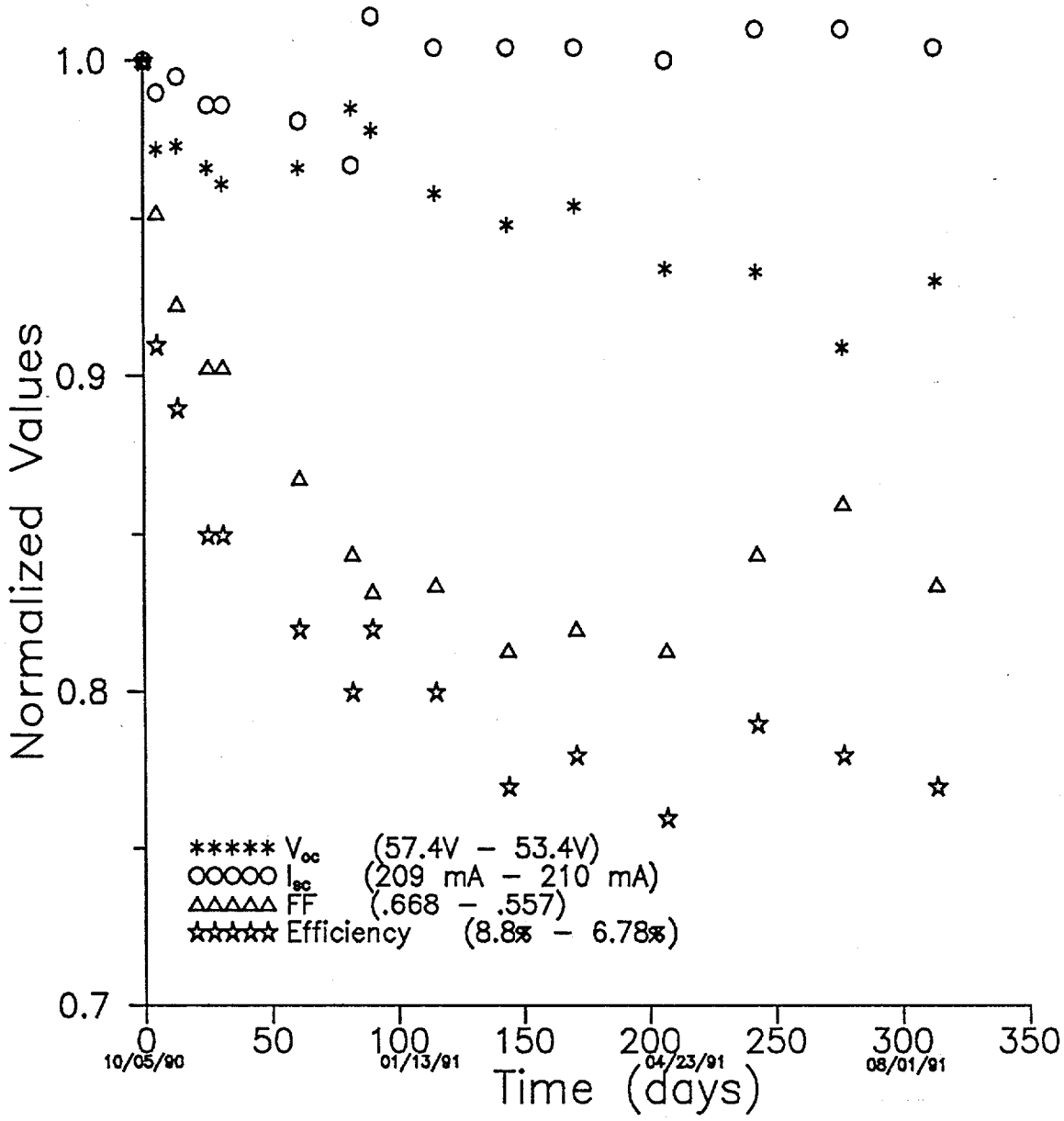

Figure 4-11. Indoor degradation of six re-scribed modules.

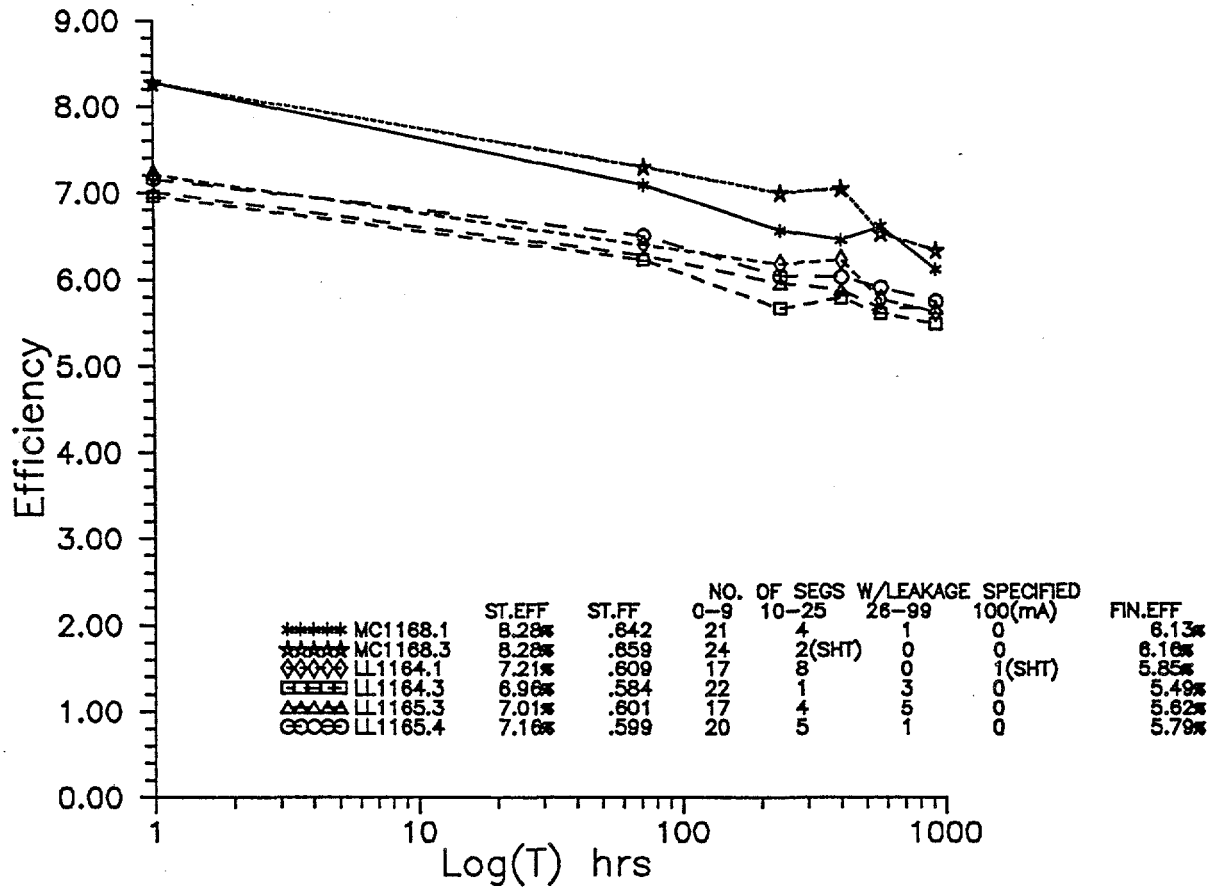

4.6.2 Modules Degraded at the PECo Test Site

Four triple-stack modules were degraded outdoors at V_{oc} at the PECo test site in Newtown, Pennsylvania. Measurements on two modules which were individually monitored are shown in **Figure 4-12**. The sudden drop in performance for one module coincided with an electrical storm. Although the module shows no visible sign of damage, the drop in V_{oc} which the module has undergone is equivalent to a couple of segments having been shorted out. After three months, the modules were re-measured indoors and it was found that their performance had decreased between 15% and 25%.

4.6.3 Modules With Al Rear Contacts

In the past we have been concerned that the Ag rear contact might be aggravating the shunt problems. In particular, one problem which was described as a relapse of the electrical cure was often noted on cells and modules having ITO/Ag rear contacts. More careful scrutiny of cells and modules having Al rear contacts, and also ZnO/Ag rear contacts, has determined that the relapse of the cure occurs regardless of the metal used. The only definite advantage of using Al for the rear contact is that the shunts which can be cured electrically, do so easily and there is less tendency for shunting defects to reform.

Another of the initially encouraging results related to the use of Al for the rear contact is shown in **Figure 4-13**. These mini-modules made on 3" x 3" superstrates show very little degradation. However, the starting efficiency is low as the cells are severely back-limited and some degradation which is occurring may be masked by the imbalance of the cells. More recent results on modules which were optically designed for the use of an Al rear contact had a higher initial efficiency (≈8%), but light-soaking of these modules does not indicate that this advantage translates to a higher stabilized efficiency, as shown in **Figure 4-14**.

4.7 Improvement of the Uniformity and Reproducibility of the Front and Rear Contacts

Results presented in the last annual report **(12)** indicated that the consistency of the series resistance and the reflectivity of the reactively sputtered ITO/Ag rear contact was less than ideal. After attempting to develop a reactively sputtered ZnO/Ag rear contact, we discovered that it was much simpler to sputter the ZnO from an oxide target. This has led to a significantly more reproducible rear contact than the previously used ITO/Ag (see Section 3.0).

Figure 4-12. Outdoor data for two of the triple-junction modules degraded at the PECo test site in Newtown, Pennsylvania (no re-scribes).

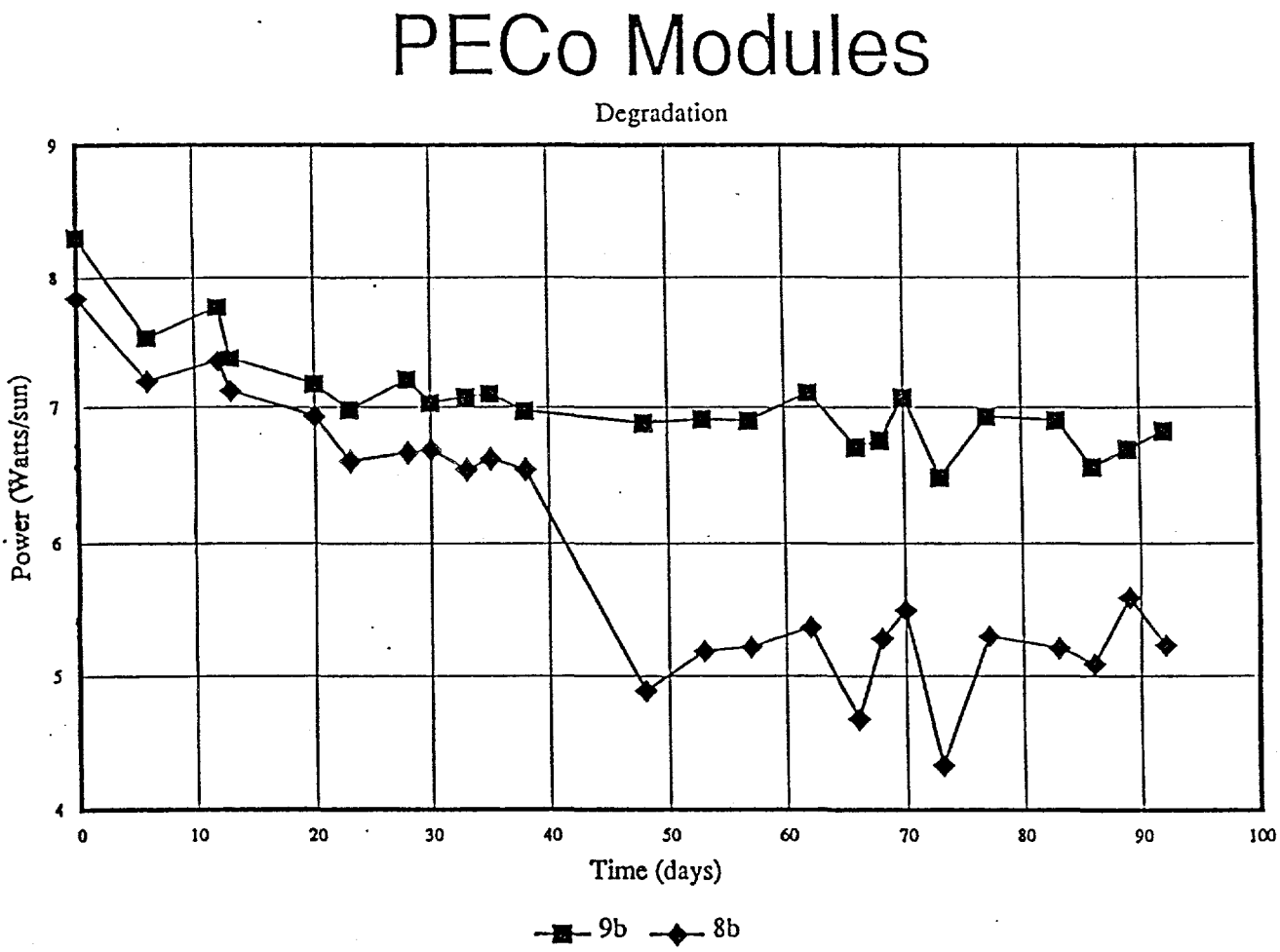

Figure 4-13. Degradation of 3" x 3" triple-stack modules which are current-imbalanced as a result of having Al rear contacts.

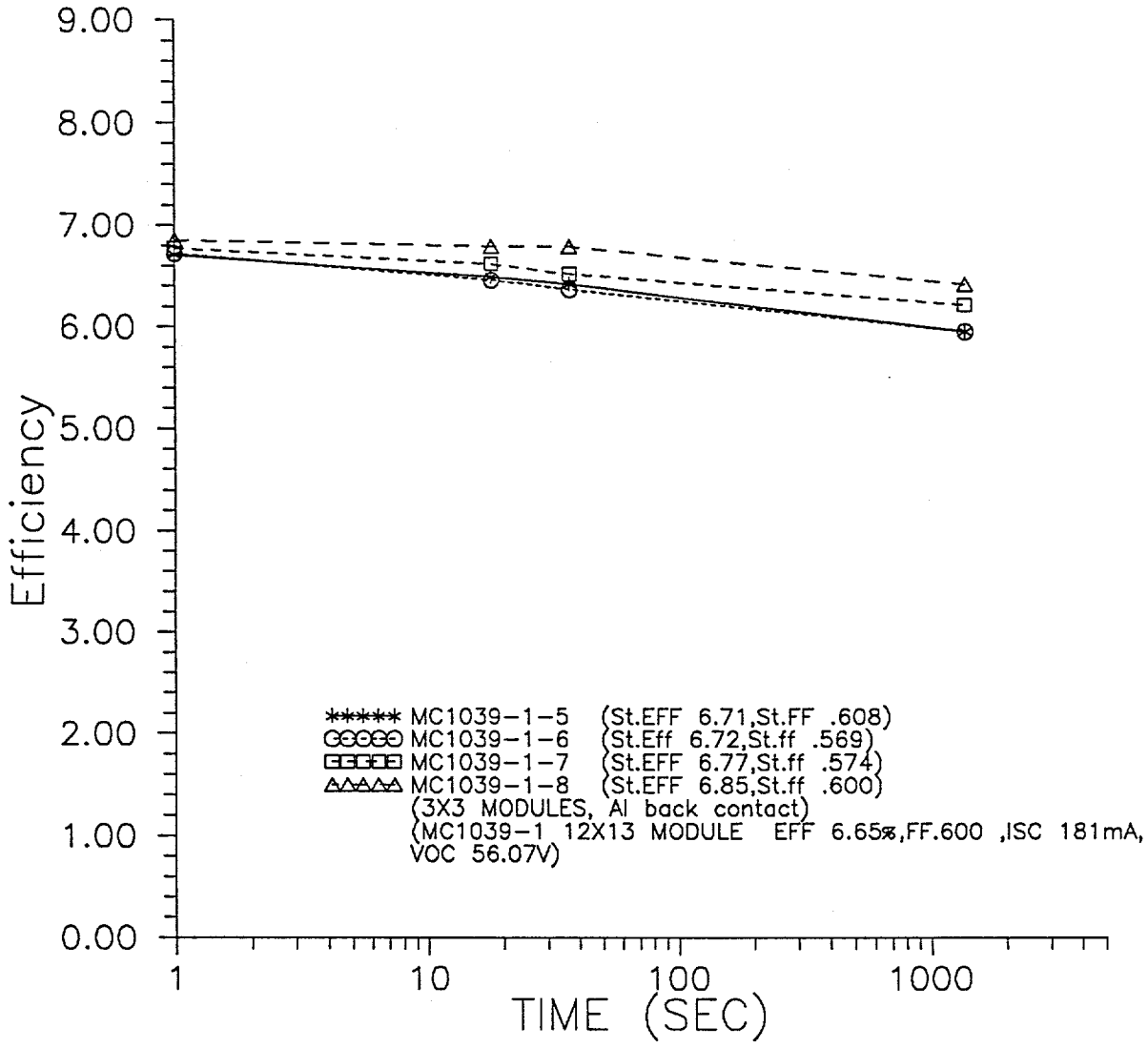

Figure 4-14. Indoor stability data for a 789 cm^2 triple-stack module which is more nearly current-balanced than the mini-modules shown in **Figure 4-13.**

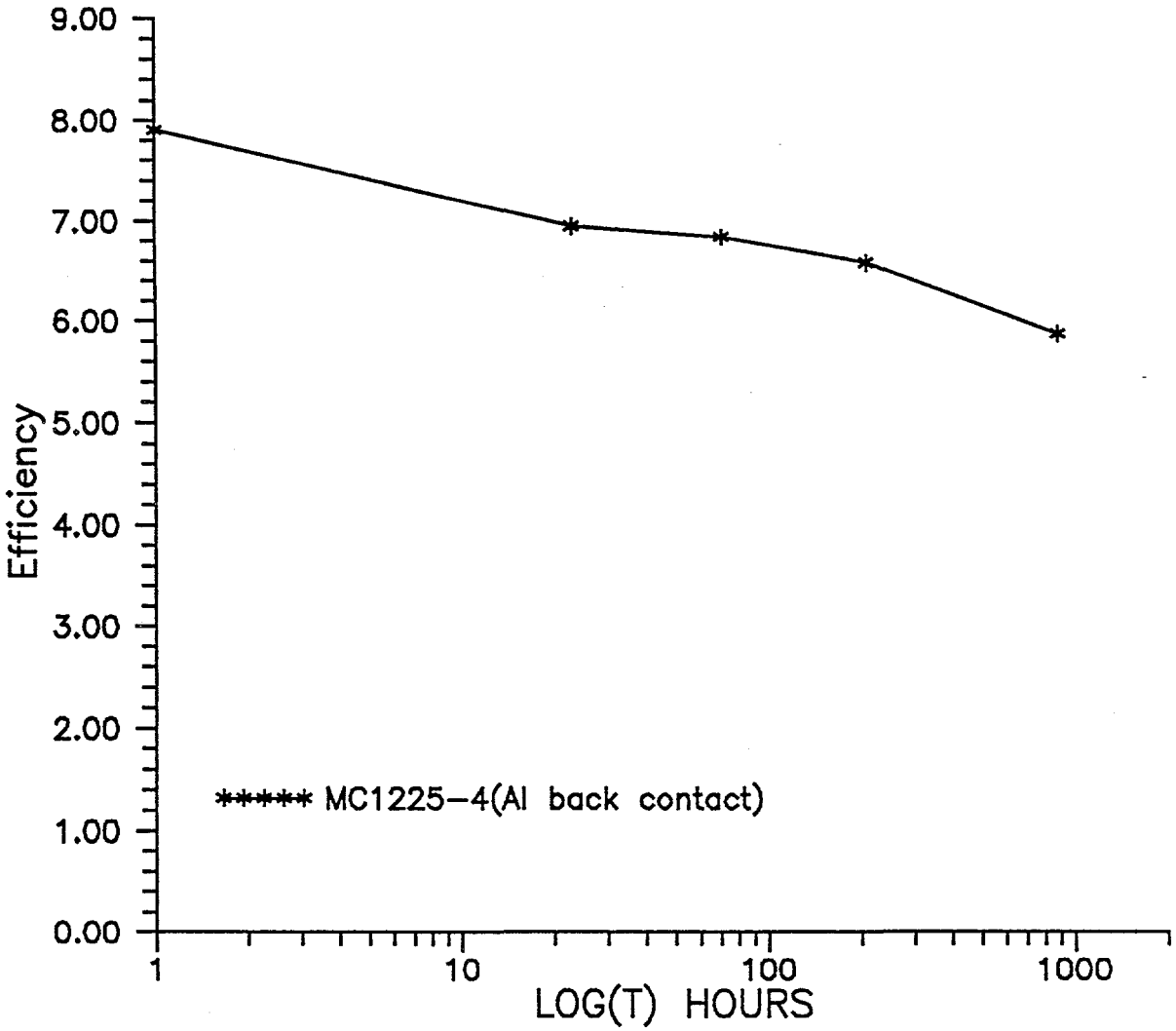

Although we believe the reactive sputtering process that has been developed will be the lowest cost process in production, the low throughput of modules in research does not enable a steady-state condition of the target to be reached, hence reprodubility is poor.

The ZnO deposition process was changed recently, leading to a variation in sheet resistance and haze across a 12" x 13" superstrate which was only half of the normal variation we observe. These improvements have contributed to a better overall uniformity of the modules we have made recently. **Figure 4-15** shows the uniformity of J_{sc} over the area of a typical module. Successive contours indicate a 1% change in current density.

4.8 Temperature Coefficient of Triple-Stack Modules

The temperature coefficient of a triple-stack module was measured between room temperature and 160°C. The results are shown in **Figure 4-16**. In contrast to the result seen in single junction modules, the temperature coefficient for triple-junction devices is slightly negative. The slight increase in short circuit current and FF with temperature is not enough to compensate for the greater drop in V_{oc}. As a practical matter, a triple-stack module measured at 25°C would be expected to lose about 7% in performance when operated at 60°C.

4.9 Summary of Task III Progress

- Increased the characterization of shunts, including the strong role played by ZnO debris.
- Reduced the impact of shunts on initial performance and on variations in stabilized performance.
- Began systematic investigation of relationship of rear contact materials to shunt resistance.
- Incorporated improved front and rear contacts into modules developed under Task 2.

4.10 Task III Work in Progress

The following topics summarize the specific issues which will be addressed by Task III group members during the rest of Phase II.

Figure 4-15. Uniformity of J_{sc} over the surface of a recently made triple-stack module.

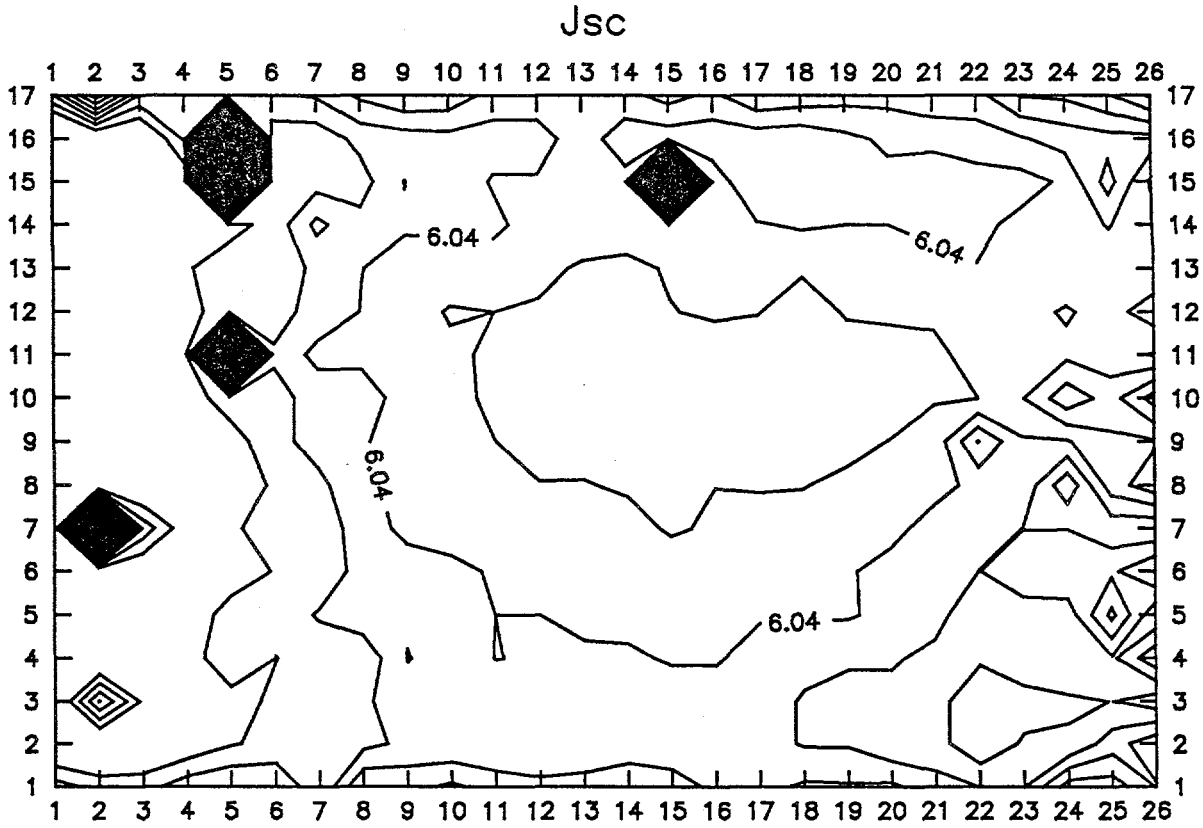

Figure 4-16. The variation of the cell parameters with temperature for a triple-stack module.

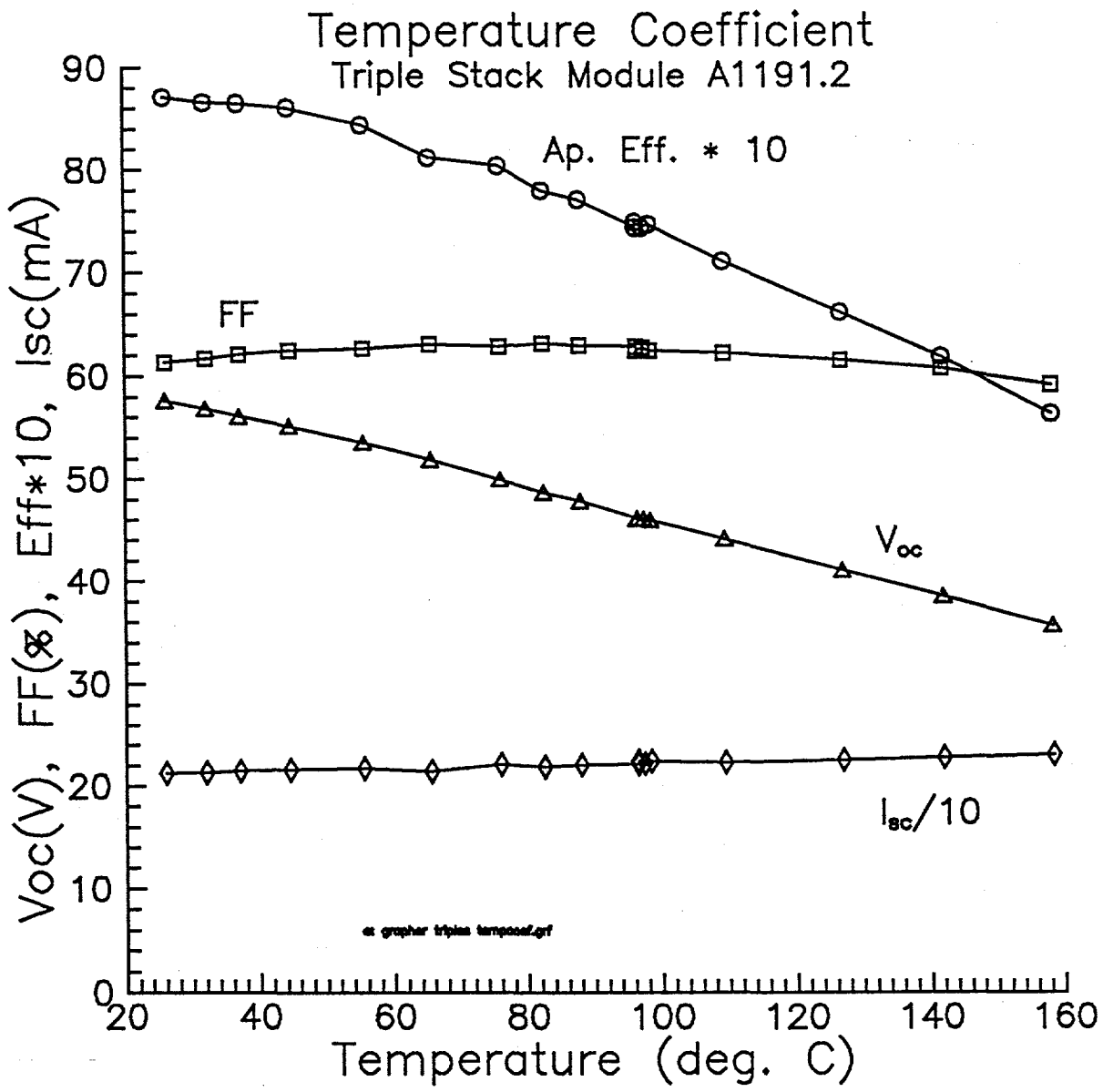

- Work on shunts will continue, by reducing the likelihood of shunt formation and by minimizing the effect of the shunts.

- Attempts will be made to incorporate higher i-layer deposition temperatures into modules in an effort to take advantage of recent progress made in Task I.

- The investigation of alternate metals for the rear contact will continue, with emphasis on Al and ZnO/Ag.

- The indoor and outdoor facilities for stability measurements will be improved. Ten more Na vapor lamps will be utilized to upgrade our indoor facility, and further modification of the outdoor facility will improve our ability to measure module performance vs. time-of-day and season.

- A round robin with NREL and Spire will be undertaken to investigate simulator performance.

- Appropriate standards which are capable of detecting changes in spectral output of the Spire lamps with aging will be fabricated, as recent measurements have indicated a need for such.

REFERENCES

1. H.R. Park, J.Z. Liu, and S. Wagner, Appl. Phys. Lett. 55, 2658 (1989).
2. L. Yang, L. Chen, and A. Catalano, Appl. Phys. Lett. 59, 840 (1991).
3. A. Banerjee, et al., AIP Conf. Proc. Vol. 234 (1991), p. 268.
4. M. Bennett, et al., Proc. of the 20th IEEE PVSC, Las Vegas (1987), p. 67.
5. M. Stutzmann, W.B. Jackson, and C.C. Tsai, Phys. Rev. B 32, 23 (1985).
6. D. Redfield and R.H. Bube, Appl. Phys. Lett. 54, 1037 (1989).
7. J. Kakalios, R. Street, and W. Jackson, Phys. Rev. Lett. 59, 1037 (1987).
8. T. Tsuda, et al., Solar Cells 9, 25 (1983).
9. M. Bennett, J. Newton and K. Rajan, Proc. of 7th European Photovoltaic Conf., Seville, Spain (1986), p. 544.
10. L. Yang, L. Chen and A. Catalano, Appl. Phys. Lett. (to be published).
11. H. Ohagi, M. Yamazaki, J. Nakata, J. Shirafuji, K. Fujibayashi, Y. Inuishi, "Optical Degradation of a-Si:H Films with Different Morphology and Preparation of Degradation-Resistive Films", Tech. Dig. of the PVSEC-3 (Tokyo, Japan, 1987), p. 671.
12. A. Catalano, M. Bennett, L. Chen, R. D'Aiello, B. Fieselmann, Y. Li, R. Podlesny, K. Rajan, S. Wiedeman, L. Yang, "Research on Stable, High-Efficiency, Amorphous Silicon Multijunction Modules", Annual Technical Progress Report for Period 1 May 1990 to 30 April 1991, SERI, Contract No. ZM-0-19033-1.
13. Y.-M. Li, B. Fieselmann and A. Catalano, Proceedings of the 22nd IEEE Photovoltaic Specialists Conference (IEEE, N.Y., 1991), to be published.
14. A. Matsuda, T. Yamaoka, S. Wolff, M. Koyama, Y. Imanishi, H. Kataoka, H. Matsuura, and K. Tanaka, J. Appl. Phys. 60, 1986, p. 4025.
15. A. Matsuda and K. Tanaka, J. Non-Cryst. Solids 97 & 98, 1987, p. 1367.
16. H. Sakai, T. Yoshida, T. Hama and Y. Ichikawa, Jpn. J. Appl. Phys. 29 (4), April 1990, pp. 630-635.
17. C. Kittel, Introduction to Solid State Physics, Wiley, 5th ed., 1976, p. 210.
18. C.K. Lau, S.K. Tiku and K.M. Lakin, J. Electrochem. Soc., 127, 1843 (1980).
19. S. Oda, H. Tokunaga, N. Kitajima, J. Hanna, I. Simizu and H. Kodado, Jpn. J. Appl. Phys. 24, 1606 (1985).
20. R. Gordon, J. Hu, J. Musher and C. Giunta, Final Technical Report, NREL Subcontract XG-0-19121-1, February, 1991.

Document Control Page	1. SERI Report No. NREL/TP-451-4720	2. NTIS Accession No. DE92001213	3. Recipient's Accession No.

4. Title and Subtitle

Research on Stable, High Efficiency Amorphous Silicon Multijunction Modules

5. Publication Date

February 1992

6.

7. Author(s)

A. Catalano, R.R. Arya, M. Bennett, L. Chen, R. D'Aiello, B. Fieselmann, Y. Li, J. Newton, R. Podlesny, S. Wiedeman, L. Yang

8. Performing Organization Rept. No.

9. Performing Organization Name and Address

Solarex Thin Film Division
826 Newtown-Yardley Road
Newtown, PA 18940

10. Project/Task/Work Unit No.

PV241101

11. Contract (C) or Grant (G) No.

(C) ZM-0-19033-1

(G)

12. Sponsoring Organization Name and Address

National Renewable Energy Laboratory
1617 Cole Blvd.
Golden, CO 80401-3393

13. Type of Report & Period Covered

Technical Report

14.

15. Supplementary Notes

NREL technical monitor: Werner Luft

16. Abstract (Limit: 200 words)

Improvements towards to goal of a 12.5% initial triple-junction module efficieny require the use of a wide gap top-layer for improved open circuit voltage, higher transmission from the transparent front contact and more highly transmitting doped layers. To address the first issue, there has been continued development of a-SiC:H with the utilization of several novel feedstocks to control the atomic structure of the solid. These films have transport properties superior to the best results reported for a-SiC:H. Preliminary results with devices exhibit a stability comparable to a-Si:H, while previous results with a-SiC:H have generally shown far higher rates of degradation.

Module fabrication has been refined to the extent that comparable module and small area device efficiencies are readily obtained. Despite the high initial efficiencies (9% - 10%) obtained in 935 cm^2 modules employing devices with 4000Å thick middle junctions, higher than expected rates of degradation were found. The cause of the anomalous degradation was traced to shunts present in the device arising from defects in the tin oxide coating. NREL degradation results of triple-junction modules showed stabilized performance of the initial efficiency for modules prepared during the period in which shunts were a problem.

17. Document Analysis

a. Descriptors

amorphous silicon ; high efficiency ; modules ; photovoltaics ; solar cells

b. Identifiers/Open-Ended Terms

c. UC Categories

271

18. Availability Statement

National Technical Information Service
U.S. Department of Commerce
5285 Port Royal Road
Springfield, VA 22161

19. No. of Pages

103

20. Price

A06